



Point Source X-Ray Lithography System for Sub-0.15 Micron Design Rules

Contract N00019-97-C-2001
Value: \$10,498,517 - Competitively Awarded

CDRL A020

Interim Report

22 January 1997 through 22 April , 1998

Prepared for

**Department of the Navy
Naval Air Systems Command
Washington, DC 20361**

**Technical Point of Contact
Richard Henson
Bldg 2185, Suite 1159, Unit 6
22347 Cedar Point Road
Patuxent River, MD 20670-1161**

May 22, 1998

Distribution Approved for Public Release; Distribution is Unlimited

19980707 167

Table of Contents

List of Figures	5
List of Tables	7
Introduction:	8
A001: SOW Task 3.2.1: X-Ray Stepper Design, Engineering, Fabrication, and Test	9
SAL Activities Summary	9
SRL Activities Summary	10
CXrL Activities Summary	11
Sanders MMIC Fabrication Activities	11
A002: SOW Task 3.2.1.1: X-Ray Aligner Design and Fabrication	12
Design Test Bed	12
Build Test Bed	12
Vibration Characterization	13
Complete Test Bed, Installation and Acceptance	13
A003: SOW Task 3.2.1.3: Alignment System Improvement	13
IBBI Alignment System Design	13
IBBI #1 Hardware, Software & Test	13
Test IBBI Gap Setting	13
ALX/ 3 Alignment System	13
ALX/3 Completion	14
ALX/3 Software	14
ALX/3 Integration	15
ALX Gap Evaluation Baseline	15
A004: SOW Task 3.2.1.5: Stage Location Accuracy Improvements	15
Overview of the BCI Brassboard Demonstration at SRL	15
BCI Critical Design Review	17
BCI Installation and Evaluation on Model 4 Stepper	18
BCI Development Program Conclusions	19
BCI System Software	20
Enhanced Global Alignment Software	20
A005: Robotic Wafer Handler	20
Wafer Handler Robot and Interface (I/F) Hardware	21
Control Software for Wafer Handler Robot and I/F	21
Proximity Bake Station	21
A006: SOW Task 3.2.1.7.3: Composite Stage	22
Design Composite Stage Upgrade	22
A007: SOW Task 3.2.1.8: Stepper Performance Verification	22
Characterization of Overlay	22
BCI Evaluation by CXrL	23
Characterization Reticles	24
Device Fabrication:	26
New device with 0.15 μ m T-gates	28
MMIC Fabrication	29
Design and Build of Masks for MMICs	29
Test Mask with Tantalum Absorber on Silicon Carbide	29

MMIC Mask Design: Mix-and-Match Consideration for Large Field Sizes	29
MMIC Mask Description	30
MMIC Mask Procurement from IBM's Advanced Mask Facility	31
T-Gate Fabrication Approach and Performance Trade-off	32
Results: MMIC Lot Fabrication	34
Overlay Measurements	34
Device Results	35
X-Ray Beam Divergence Impact on MMIC Device Fabrication	36
A008: SOW Task 3.2.2.1: Solid State Driver Development	38
Measure Voltage Rise Time Requirements	38
Design of Modules	39
Solid State Driver Measurements	41
Studies on Phase II Deliverable Module Options	41
Dummy Load	44
A009: SOW Task 3.2.2.2: Source Lifetime Improvement	44
Anode Materials/Design Trade-Off	45
Degasser	45
Short Anodes	45
Anode Gas Injection	48
Water Cooled Cathode Rods	49
Insulator Life Enhancement	51
Chopper Life Enhancement	53
A010: SOW Task 3.2.2.3: Source Testing to Verify X-Ray Output	55
EMI enclosures, Power Supplies, Power Feeds, and Supporting Systems	55
DPF Base and Power Feed	55
Vacuum System	56
Thermophoretic Particle Precipitator	58
DPF Source Computer Controls and Hardware Interrupts	59
New Anode Base	60
Electrodes	62
Chiller	63
DPF Source Serviceability	63
Install and Test DPF Driver:	64
Early System Demonstration	64
One Hundred Million Shot Module Test	66
Power Semiconductor Life Analysis	68
Module Life Test Summary	68
Bringing System on Line into Dummy Load	69
Bring System on Line into DPF Load	70
DPF Source Characterization by CXrL	72
Beamline and Collimator Development	75
A012: SOW Task 3.2.4: System Integration	77
System Specifications Review	77
DPF Point Source System Control Interface	81
Point Source Design Configuration Considerations	86
Interface with Stepper	86
Beam Height and Overall Height	87

Collimator Accommodation	88
Beamline Interface	89
Point Source Interface Conclusions	89
A013: SOW Task 3.2.5: Compatibility with Laser Based Point Source	90
Expectations for the Future	90
JMAR X-Ray Source Spectrum	90
JMAR Source Evaluation	90
JMAR Laser Plasma X-Ray Point Source Power Estimation	91
JMAR Laser Plasma X-Ray Point Source Uniformity Estimation	92
JMAR Laser Plasma X-Ray Point Source Size Estimation	92
JMAR Source Evaluation Conclusions	93
Appendix A: Revised System Specifications	95
Appendix B: Photographs of SAL Produced Equipment	104

List of Figures

Figure 1: Schematic of BCI demonstration at SRL. The individual colors of the bichromatic beams are shown, light gray, (1064 nm), and gray, (532 nm), respectively; they are shown separate for clarity, but in reality overlap. The baseline HP interferometer beams, (633 nm), are shown in black. The baseline and bichromatic beams propagate parallel to one another—but separated by approximately 10 mm—through the turbulent region in the probe arm of the main interferometer.....	16
Figure 2: The BCI installed on the Model 4 Stepper at CXrL. The y-axis system, including both the HP laser gauge and the BCI, are mounted above the granite at the top of the photograph. The x-axis hardware at bottom center is visible through the opening in the granite.....	18
Figure 3: BCI Phase as a Function of Time, While Stage is Displaced Discretely.....	19
Figure 4: Four Fields of the SAL X-Ray Stepper Cover a 3 Inch GaAs Wafer	30
Figure 5: Detailed Layout of a Single Field of the MMIC Reticle for Ultratech 1 X Photostepper.....	31
Figure 6: A 3-6 GHz LNA With an Expected Performance of 1 dB Noise Figure and 22 dB Associated Gain, Based on 0.25 micron Gate Length PHEMT Device.....	31
Figure 7: A Millimeter Wave (above 30 GHz) LNA Based on 0.15 micron Gate Length PHEMT Device. The expected performance for this chip has a noise figure of 2.5 dB across a broad bandwidth.....	32
Figure 8: Cross Section of a T-Gate Fabricated Using a Dielectric Layer to Support the "T" Structure	32
Figure 9 (a and b): T-Gate Fabrication Based on a Bilayer Resist Process, Resulting in a Free Standing "T" Structure. A device cell made up of six gates is also shown.	33
Figure 10: PHEMT DC Electrical Characteristics Showing Transconductance, G_m , and Drain Current, I_d , as a Function of Gate Bias, V_g	36
Figure 11: Schematic Diagram of MMIC Gate Metal Evaporation from a Source Showing the Requirement from a Resist Processes to Achieve Reliable Step Coverage as Well as Clean Lift-Off.....	37
Figure 12: Solid State Pulsar Waveforms Driving the DPF X-Ray Source. Left trace shows the full discharge pulse. Right trace shows expanded view of voltage rise time across the DPF electrodes.	39
Figure 13: Solid State Module Schematic Diagram. Twelve parallel modules make up the full power DPF driver.....	40
Figure 14: Photograph of the DPF Solid State Drive Module	41
Figure 15: Photograph of the 12 Module Solid State Driver Test Bed	41
Figure 16: Measured DPF Voltage and Current Waveforms Generated by a Spark Gap Power Supply, (left), and Simulated for the Solid State Supply, (right).....	42
Figure 17: Voltage and Current Waveforms Generated by the Solid State Module into a 0.25W Resistive Load.....	43
Figure 18: Comparison of Output versus Energy for Different Anode Lengths.....	46

Figure 19: Hollow Cathode Array with Pulse Discharge Capacitors	54
Figure 20: Chopper Coupling.....	54
Figure 21: View of Interior of Vacuum Chamber, as Seen From the Pinch, Showing Cooled Cylindrical Liner, Dome, and Conical Beamstop	58
Figure 22: New Anode and Anode Base.....	61
Figure 23: New Electrode Set.....	62
Figure 24: Withdrawal of the Vacuum Chamber.....	64
Figure 25: View With Head Exposed Showing Pneumatic Clamping System	65
Figure 26: View of Vacuum Chamber Covering DPF Head.....	66
Figure 27: Voltage and Current Waveform for 6 Parallel Modules Driving a 0.025W Resistive Load at an Initial Charge Voltage of 7 kV.....	69
Figure 28: X-Ray Source Waveforms Generated by the 12 Module Solid State Driver. The pulser was charged to 5 kV, and the X-Ray head was pressurized to 1.3 torr neon.....	70
Figure 29: Waveforms with Pinch. 7 kV charge, 1.0 Torr Ne.....	71
Figure 30: View of Beamline.....	72
Figure 31: X-Ray Transport Line, (No Collimator)	75
Figure 32: X-Ray Transport Line with the CXrL Collimator.....	77
Figure 33: GaAs Industry Linewidth Needs Determined from a Survey	79
Figure 34: GaAs Industry Throughput Needs Determined from a Survey	80
Figure 35: GaAs Industry Field Size Needs Determined from a Survey.....	80

List of Tables

Table 1: Refractive Index Difference Determined from the Data of Fig. 3	19
Table 2: Experimental and Simulated Results for CD Linewidth Broadening	27
Table 3: Type and Number of Exposed Wafers at CXrL	29
Table 4: Sheet Conductivity and Contact Resistance on PHEMT Device lot 97-208 After the Ohmic Process	34
Table 5: Residual Errors, (in microns), in Placement of the Gate Footprint in the Device Channel	35
Table 6: PHEMT Device Characteristics Including Channel Currents, Transconductance, and Source Resistance	36
Table 7: DPF Solid State Power Supply Design Specifications	39
Table 8: Summary of 100,000,000 Shot Tests	67
Table 9: Photocell Response and Al Film Transmission	74
Table 10: Summary of Exposures Conducted at SRL by CXrL for Source Characterization	74
Table 11: X-Ray Source Control Message List	82
Table 12: X-Ray Source Command/Response Format	85
Table 13: Al Filters Combinations Used in JMAR Laser Plasma Source Spectrum Evaluation	91

Point Source X-Ray Lithography System for Sub-0.15 Micron Design Rules

Interim Technical Report for 22 January 1997 through 22 April, 1998

Introduction:

The team of Sanders, a Lockheed Martin Company, Suss Advanced Lithography, (SAL), Science Research Laboratory, (SRL), and the Center for X-Ray Lithography, (CXrL), at the University of Wisconsin are developing a point source X-Ray lithography system for sub-0.15 micron design rules. The system will consist of a SAL developed stepper, an SRL developed Dense Plasma Focus, (DPF), X-Ray source, and a CXrL developed beamline. The system will be delivered to Sanders in the spring of 1999. Sanders is leading development of gallium arsenide wafer processing technology for the MMIC "T" gate process, and is carrying out a prototype fabrication run of 35 GHz MMIC low noise amplifiers. During development of the point source system, the processing work has been conducted at CXrL using the CXrL synchrotron source and SAL Model 4 stepper.

The program has been funded in two Phases. The first phase of 15 month duration, running from January, 1997 to April, 1998 concentrated on development of components for the lithography system. Beginning with an existing machine that used spark gap switching, SRL has developed an all solid state driver and improved head electrode assembly for their dense plasma focus X-Ray source. Likewise, SAL has used their existing Model 4 stepper installed at CXrL as a design starting point, and has developed an advanced stepper test bed. The test bed includes the frame, coarse and fine stages, wafer load/unload system, ALX3 alignment system and controlling software, and will be completed in Phase 2 to become the next generation stepper (Model 5 or SAL designation XRS2000/2). SAL has also investigated two advanced systems, an improved alignment system, (Interferometric Broad Band Imaging, IBBI, alignment system), and air turbulence correcting stage interferometer, (Bichromatic Interferometer, BCI). CXrL has designed a beamline for the system, has designed a scanning mirror collimator, carried out X-Ray source testing and has supported Sanders in MMIC process development.

In the Phase 2 program that began on 22 April, 1998 and has a 24 month duration, the system components will be completed, delivered to Sanders, and integrated into a complete system. Integration is scheduled to run from 15 March to 1 June 1999. The system will be evaluated and used to fabricate a pilot production run of 35 GHz low noise and power MMICs.

This Interim Report describes the Phase 1 program activities that have culminated in acceptance in place by Sanders of the DPF X-Ray source with Solid state driver and Stepper Test Bed. The report follows the format of the contract Statement of Work, and describes activities that took place in each SOW task.

A001: SOW Task 3.2.1: X-Ray Stepper Design, Engineering, Fabrication, and Test

This summary level task includes all program technical activities. These consist of four major activities; stepper development led by SAL; source development led by SRL, beamline and collimator development led by CXrL; and device fabrication demonstration led by Sanders. Each team member is contributing in each area as required to insure an integrated system.

SAL Activities Summary:

In general, this report describes the tasks carried out by Suss Advanced Lithography to develop technology for an X-Ray Stepper Lithography System with sub-0.15 μm working resolution, (with potential for extension to 0.13 μm), that meets the requirements of DARPA BAA 95-022, and DARPA performance goals.

SAL worked as a subcontractor with Sanders. Also included as team partners were Science Research Laboratories and the Center for X-Ray Lithography at the University of Wisconsin. The program will combine SAL stepper technology and SRL X-Ray source technology. Additionally, SAL let subcontracts for specific tasks to MIT, (IBBI), SRL, (BCI), and UVM, (stage).

SAL provided planning; design, development and demonstrated portions of an X-Ray stepper suitable for interfacing with the dense plasma focus point source. A basic design goal was that this tool is applicable to and with US industry standards for companies interested in developing an in house X-Ray lithography capability.

The Model 4 stepper and Aladdin synchrotron were used to demonstrate and validate critical stepper capability.

An advanced stepper test bed, (Model 5), and MHS, (Material Handling System – a.k.a. Bake Station), has been constructed tested and demonstrated.

On 12 March, 1998, SAL demonstrated the functionality of the Model 5 Test Bed and MHS. The basic functions of the mask stage, wafer stage, laser interferometer system, ALX/3 alignment system, X-Y stages and, Graphical User Interface were installed on the test bed, and operational. The demonstrated functionality was consistent with SOW Phase 1 tasks. This is a prerequisite to completing and delivering the completed stepper to Sanders at the end of Phase 2.

Sanders witnessed that this demonstration and documentation fulfills the SOW requirements for Phase 1 of the program. The test results provided at this time represent preliminary data, which is consistent with the final acceptance criteria. SAL has delivered to Sanders pertinent documentation and test results.

A design group was formed at SAL to document the Model 4 upgrades and provide a basis of design for the test bed. Close consultation with the Karl Suss Munich designers and drawing sets was necessary to extend the design. A support network of suppliers was developed to provide timely delivery of granite, mechanical, and electrical elements. Meetings were held with CXrL and SRL designers and engineers to plan and

coordinate construction. Plans were made to test the Model 4 design for stability and performance.

SAL worked closely with engineers from SRL, CXrL, and MIT to design stepper enhancements required by the contract. These enhancements in stage accuracy, gapping, and investigations of an alternate or supporting alignment system were designed to first be placed into the existing Model 4 stepper at CXrL, then incorporated into the test bed design, if proven successful. Other improvements were to be added to the test bed only, such as the material handling and the robotic bake station. A pure engineering study of alternative materials for the existing Y stage granite member was undertaken successfully.

Photographs of SAL developed equipment appear in Appendix B.

SRL Activities Summary:

Over the first period of this contract, SRL has achieved a major advance in the technology of X-Ray point sources. The specifics of these advances are summarized below.

A new Dense Plasma Focus, DPF, geometry was developed that increases the X-Ray output by more than a factor of three, and that decrease the pulse storage and switching drive requirements by a factor of two when compared to the performance of the original SRL spark gap switched DPF machine, (developed under a previous contract). These advancements will allow the new machine to reach well over a kilowatt of X-Ray output (into 4π sr), which corresponds to entry level, or more, levels of production throughput.

An all-solid-state power supply consisting of 12 parallel driver modules was designed, fabricated, and tested into both a resistive load and the DPF X-Ray source. The all-solid-state driver modules met all the performance specifications listed in design goals. A 100 million shot lifetime test was conducted on a single module. This tests shows that the modules will meet the 3×10^9 shot life requirement.

A new laboratory prototype has been built to support the new driver technology. This laboratory prototype has been built to serviceability standards which will carry over directly to an industrial setting in the semiconductor industry. The system has just been brought on line. The stability of triggering and pinch formation time are markedly better than encountered with the spark gap driven machine. X-Rays are being reliably produced at levels in line with levels produced on the previous spark gap driven machine. Runs of 4000 pulses have been achieved with no X-Ray dropouts.

A major function of the all-solid-state driver was to eliminate the current reversal that was implicated in anode erosion. Inspection of an anode subjected to 40,000 shots shows that material removal from the anode is at least tens of times smaller than was observed with the spark gap driver. This is highly encouraging. Because of the difficulty in accurately quantifying the small amounts of material removal, detailed

measurement will have to await the buildup of at least several hundred thousand shots on the machine.

CXrL Activities Summary:

The University of Wisconsin—Madison Center for X-Ray Lithography, (CXrL), has completed all tasks of Phase I of the Point Source Lithography System for Sub-0.15 μm Design Rules. CXrL's role in the program was to provide support for X-Ray stepper engineering, X-Ray source evaluation and X-Ray beamline design. X-Ray stepper engineering support included evaluation of various upgrades to the existing X-Ray stepper located at CXrL's facilities in Stoughton, WI. The beamline design included an optional collimator design to enhance the performance of the lithography system. CXrL conducted preliminary evaluations of 2 different X-Ray sources including a Dense Plasma Focus point source and a laser-based point source.

Sanders MMIC Fabrication Activities:

This report covers the work completed during Phase I, March 1997 through April 1998, on the MMIC fabrication task. We transitioned to using silicon carbide membrane and tantalum absorber masks. This has allowed us to use in-board alignment marks as well as address the mix-and-match issues between a UV phot stepper tool and the SAL X-Ray stepper.

Using a high resolution test mask, we refined the SAL605 negative resist process for MMIC gate application. The post exposure bake temperature parameter was readjusted to hold the dose requirement at a reasonable range of 130-150 mJ at the mask plane, or about 65-75 mJ on the wafer. The differences between silicon and GaAs substrates were characterized. At a given post bake temperature there were occasional problems such as incomplete development of the resist that were traced down to surface condition of the GaAs substrates. These were also overcome by treating the surface of the GaAs with mild acid. There were notable improvements in lithography for MMIC gates. Based on ESCA surface analysis, the acid treatment has been carried out for even more prolonged periods on mechanical substrates of GaAs indicating even higher yields for gate lithography. However, this last result has not been integrated in the device fabrication process, due to concerns over PHEMT device degradation.

Overlay between the X-ray and photo steppers draws attention to several issues. First, the 1 X chrome photomask from commercial suppliers needs to be procured with tighter placement parameters. For a field size of 30 X 23 mm, the placement in the photomasks must be within 120 nm. For mix-and-match purpose, a phot stepper with large field capability is required, so that one field of the phot stepper matches with the X-Ray field in the future. We have noted that using an industry standard cost effective tool such as the Ultratech model 1500, the throughput will be lower by a factor of 3 from our target figure.

The T-gate process is the MMIC industry's standard bearer for high performance chip fabrication. We have achieved success in fabricating T-gates on PHEMT device wafers with device performance comparable to the electron beam direct write process. The T-gate structures are freely standing structures, without the support of a thick nitride layer as used to be the case with an earlier process.

Finally, the mask contrast of the recent tantalum silicon absorbers produced by IBM is even lower than the masks we received in 1997, which contained tantalum and boron material. We are looking at modifying the MMIC gate process to adjust to the mask characteristics so that we can move ahead with demonstration of 0.15 micron gate MMICs in the next phase of the program.

A002: SOW Task 3.2.1.1: X-Ray Aligner Design and Fabrication

The next generation X-Ray stepper test bed is designed and fabricated by SAL in this task, including installation of an improved alignment system. The existing Model 4 stepper, operational at CXrL is the starting point for the design.

Design Test Bed:

A test bed was designed using the Model 4 as the basis. The Model 5 incorporates similar large granite blocks as base and upright stage support. A cavity space in the upright granite incorporates the mask manipulator stage and the alignment system, while allowing for exposure X-Rays to reach the mask. The cavity was enlarged to allow space for several options in flux delivery. A provision for a point source beamline interface was included in the design, as well as a helium containment system. An integrated mask and wafer handling system is supported on the base granite and isolated during sensitive stepper functions, while allowing for robotic interfacing from the Material Transfer System in Phase 2. The XY stepping stage was lengthened in the Y direction for greater clearances during handling steps. Improvements were made in the granite manufacture to add strength and for better access for cable routing and service. The electrical system was upgraded to improve signal routing and access. Many new and improved components were incorporated in the electrical interface junction areas and internodal wiring. An improved feedback device was developed for use on this lithographic tool and incorporated into the wafer alignment stage. Improvements in the laser interferometry mounting hardware allow more flexibility in alignment and layout. Provisions were made for the BCI integration to follow in Phase 2.

Build Test Bed:

The test bed was constructed using onshore suppliers wherever possible. A local manufacturer of precision granite instruments was used to fabricate the granite elements to SAL specifications. Several additional local shops were utilized to provide quality machining and surface treatment to subassembly materials. Each incoming part was inspected and cleaned before assembly. Subassemblies were wired and shelved for later buildup in the cleanroom. The electrical control system was built up to include improved access to all signals and junctions. Care was taken in cable placement both between the system and rack and also onboard the stepper to provide improved signals and appearance. During the final assembly of the test bed, tests were conducted on the mask, wafer, and step stages to check calibration and accuracy during startup.

Preliminary data indicates an improvement in gap setting and wafer leveling capabilities consistent with the goals of the 0.15 μ m program.

Vibration Characterization:

Members of the UVM engineering department tested the stepper at the SAL facility after assembly. The test bed was fitted with acceleration sensing devices in the vertical and horizontal planes. Vibration was introduced by an external tool to the test bed at various points and on the floor adjacent to the granite while test data was taken. Mr. Paul Parise of SAL submitted a report of the results of data analysis on 12 March, 1998. Further testing of the system for vibration will be done as a regular part of Phase 2 continued developments, particularly after full operation is achieved with the addition of the robotic wafer interface.

Complete Test Bed, Installation and Acceptance:

The test bed was completed on schedule and demonstrated to Sanders. All mechanical systems were assembled to the system and all wiring required for the Phase 1 demonstration was in place. The test bed supporting structure (base) was temporary and will be built during Phase 2 and installed prior to the arrival of a class one environment. Initial testing of the mask stage accuracy and wafer stage gapping and alignment drive motion was undertaken and reported on at the acceptance. The ALX alignment system focus mechanism was tested for accuracy and repeatability. The GUI interface was prepared for demonstration over the network of the test bed as well as the Material Handling System. The test bed was demonstrated to perform basic wafer handling, stepping, and alignment system instructions consistent with requirements for the Phase 1 project. Testing and run-in to improve handling speeds and to measure accuracy is ongoing. The BCI demonstration was done at the SRL laboratory and was then installed on the Model 4 stepper at CXrL in Wisconsin.

A003: SOW Task 3.2.1.3: Alignment System Improvement

Here, a 3 microscope version of the SAL ALX alignment system is installed and characterized on the stepper test bed, (Model 5), and a four microscope system is designed for use on the Model 5 stepper in Phase 2.

The IBB alignment system developed by engineers and scientists at MIT was developed for insertion into the Model 4 stepper system at CXrL. A plan to conduct side-by-side tests was developed to give the most meaningful test data since the ALX alignment system is a mature design. A plan to retrofit a new mask stage plate carrying the 4 channels of the IBB was developed and implemented. Problems in acquiring sufficient signal strength and other developments forced a redirecting of the IBB effort and introduction of the ALX/3 into the test bed in order to maintain schedule. Details of the IBB follow.

IBB Alignment System Design:

A mechanical and electrical design for the IBB system was developed jointly between SAL and MIT. This design was compatible with the Model 4 stepper. Multiple laser light sources were evaluated resulting in the selection of a multi-line argon laser light source. A new mask stage was designed to integrate the IBB optics into the Model 4. This new design supported X and rotational movement of each IBB pair for adjustment

to the loaded mask. A DSP based vision processor was also selected for analysis of the resulting IBBI images.

IBBI #1 Hardware, Software & Test:

All optics and mechanics were fabricated and installed on the Model 4 stepper. The DSP based electronics were purchased. An existing LabView algorithm developed by MIT was available as a benchmark for development of the DSP software as well as a test tool for use with the Model 4 until the complete electronic and software system was available. Evaluation of the performance of the system on the Model 4 resulted in poor signal quality, which could not be used for alignment measurements. The significant contributing factors to the poor signal quality were weak laser illumination and mask fabrication issues. The IBBI project was taken off the critical path for further development at MIT during Phase 2. The IBBI Final Technical Report was submitted on 22 December, 1997.

Test IBBI Gap Setting:

This task was deleted with the rescheduling of the IBBI project. Gap setting tests were performed under the ALX Gap Evaluation Baseline.

ALX/3 Alignment System:

As a result of the IBBI#1 testing, SAL recommended an alternative alignment strategy to replace the IBBI#2 tasks with ALX/3 tasks for the Model 5 in Phase 1, and with ALX/4 tasks in Phase 1 and 2. Sanders accepted these recommendations with the provision that SAL continue to fund the MIT IBBI project at a level of effort in Phase 2.

SAL refurbished and tested a three-microscope version of the ALX alignment system, installed it on the Model 5 stepper at SAL, and verified its ability to meet the program overlay goals for Phase 1. Additionally SAL developed and designed a four-microscope version of the ALX that will meet the program goals for Phase 2. The four-microscope version will be built in Phase 2.

The ALX/3 system design was adapted for use on the Model 5. Associated adapters were designed to allow an existing ALX/3 microscope manipulator to be mounted on the Model 5.

ALX/3 Completion:

A three microscope manipulator with the associated signal processing electronics was installed on the Model 5. The microscope manipulator was stripped, cleaned, reassembled and aligned. The electronics were incorporated into the existing electronics rack and machine cabling.

ALX/3 Software:

Existing software from the Model 4, ALX/2 was modified to support the third microscope. The Model 5 system software will support both the ALX/3 and ALX/4 configurations. This software was used during the demonstration on 12 March, 1998. Additional software will have to be written during Phase 2 to support the full configuration and features of the ALX/4.

ALX/3 Integration:

An ALX/3 alignment system was incorporated into the test bed to serve until an ALX/4 system is complete. The alignment system hardware consists of three matched alignment channels equipped with CCD cameras on flexure stages mounted to independent stages. The physical dimensions of the Model 5 required design changes in the optics mounts and manipulator base. After studying several approaches, which included remanufacturing certain mount elements and additional calibration, a plan to raise the manipulator on a spacer plate was chosen. A design and manufacture period, during which the manipulator was reworked and realigned, was undertaken. Optics extensions were made to provide the correct focus plane for the Model 5 integration. The alignment system was calibrated externally prior to installation. Integration involving adjustment to agree with all stepper orthogonal systems was done and the hardware was tested for functionality, accuracy, and repeatability. The electrical and software subsystems were integrated with custom cabling. A demonstration of alignment system operation was performed for the Sanders demonstration. Lack of a suitable matched mask and wafer set prevented complete testing and demonstration. Further testing and evaluation will be undertaken during Phase 2.

ALX Gap Evaluation Baseline:

A new displacement measurement sensor was developed and evaluated by SAL R&D on the Model 5. The DVRT sensor improves upon the effective resolution of the LVDT sensors used on the Model 4 by increasing the signal to noise ratio significantly. The new sensor will allow the wafer chuck to be adjusted more accurately. The system was installed on the Model 5 and evaluated against an external sensor.

A004: SOW Task 3.2.1.5: Stage Location Accuracy Improvements

The stage interferometer is upgraded under this task by incorporating a bichromatic interferometer, (BCI), that compensates for air turbulence inaccuracies. The task is subcontracted by SAL to SRL, and will result in design and fabrication of a BCI prototype that will be installed on the Model 4 stepper and evaluated. The BCI is to function in a non-interfering mode with the existing Hewlett Packard Interferometer.

The BCI upgrade required support of SRL engineers in the form of system drawings and software architecture. Design and manufacture of the initial BCI test devices on the Model 4 ran over schedule. A detailed description of the BCI effort to date follows.

After SAL generated specifications and evaluated required changes to the Model 4, the SRL subcontract for development of the BCI was signed on 27 March, 1997. We identified as a challenging design task that the critical optic for the BCI is a 1/4 wave retardation plate. The optic has precisely 1/4 wave of retardation at 3 wavelengths (HP 633nm and BCI 532 & 1064nm). This optic had to be integrated with the HP optics, and the combined HP/BCI optics had to fit into the available space on the stepper. In addition the BCI optics requires precise alignment.

Overview of the BCI Brassboard Demonstration at SRL:

The BCI was demonstrated on an optical bench at SRL on Dec 17, 1997. The optics included the HP x axis interferometer, (HP 10719), and the BCI x axis module, (see Figure 1). The BCI optics measured the air turbulence in a path parallel to the HP

beam path. The paths were 10mm apart. Using parallel paths allowed us to demonstrate that the BCI measured air turbulence was very similar to the turbulence measured by the HP. However, we were not able to subtract the BCI output from the HP signal to cancel the air turbulence in the HP, since the paths were not coincident.

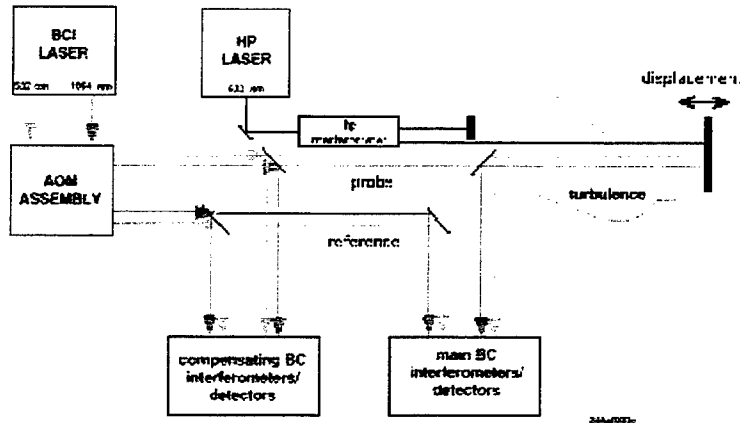


Figure 1: Schematic of BCI demonstration at SRL.

The individual colors of the bichromatic beams are shown, light gray, (1064 nm), and gray, (532 nm), respectively; they are shown separate for clarity, but in reality overlap. The baseline HP interferometer beams, (633 nm), are shown in black. The baseline and bichromatic beams propagate parallel to one another—but separated by approximately 10 mm—through the turbulent region in the probe arm of the main interferometer.

The BCI laboratory demonstration at SRL dramatically exhibited three critical features of the relationship between the baseline HP laser gauge and the BCI:

- Whereas the HP gauge measures both the displacement of a mirror and changes of the air-path thickness, (turbulence), on the way to the mirror, the BCI measures changes of the air-path thickness, but is insensitive to displacement of the mirror.
- When the mirror is held fixed and the BCI signal is multiplied by the appropriate, theoretically predicted scale factor, the BCI signal closely tracks variations in the HP-gauge signal that are due to air-density variations.
- When multiplied by the same scale factor, the noise level of the BCI signal is smaller than that of the HP laser gauge.

This laboratory demonstration was a vivid, hands-on proof of principle for the BCI. It showed that the BCI signal is indeed a measure of the instantaneous air-path thickness. It follows that the BCI signal can be used to correct the HP fringe signal for turbulence, yielding a corrected signal that is a function of the mirror position only.

Results of Demonstration:

The demonstration agreed with the predictions of the analysis discussed above:

- (1) The air-density variations detected by the two interferometers—as determined by comparing the compensated BCI fringe-shift signal with the baseline fringe-shift signal when the mirror was held fixed were well correlated but not identical. When the two signals were viewed on the same scale, it was found that they tracked one

another quite well on a time scale of 0.2–50 s. This tracking occurred in spite of the fact that the baseline and bichromatic beams were separated by approximately 1 cm, which shows that nearly all the air-density variations are on a scale larger than 1 cm. However, it was observed that

- (a) On a long time scale—approximately 1 minute—the baseline signal and the scaled BCI signal slowly drifted apart. This drift is most likely due to a slow, systematic change in path length that results from thermal expansion of the optical table.
 - (b) On a short, (0.2 s), time scale, the BCI signal contained sudden, rapid spikes that were not present in the baseline signal. These spikes may be due to a number of factors, including laser pointing jitter and the motion of dust through the BCI beams.
- (2) The BCI signal is insensitive to mirror motion that is easily detected by the baseline interferometer. This insensitivity was demonstrated as follows:

The position of the mirror shown in Fig. 1 was piezoelectrically modulated sinusoidally with an amplitude of ≈ 500 nm and a frequency $f_0 \approx 0.2$ Hz. The baseline interferometer easily detected this motion. It produced a signal containing two components: (1) a sinusoidal signal, due to the motion of the mirror, and (2) other, smaller variations, predominantly due to air-density variations in the path of the beam. For this sinusoidal mirror motion of ≈ 500 nm, the BCI should see a signal of ≈ 2.5 mdeg, which is below its noise level. Indeed, no BCI signal correlated with the motion of the mirror was observed.

In summary, the SRL brassboard demonstration experimentally confirmed the theoretically predicted principles of the BCI.

The work-around electronics were also included in the Brassboard Demonstration. The work-around electronics consist of a National Instruments Data Acquisition Board running in a 75MHz Pentium computer running LabView under Windows 95. Technically this system appeared to work fine; however, it is suitable for demonstrations only. Windows 95 is not compatible with the stepper's requirement for a reliable, real-time operating system.

BCI Critical Design Review:

A BCI Critical Design Review was held at SRL on February 12, 1998. SRL presented its revised plan and schedule for the completion and installation of the BCI on the Model 4 stepper at CXrL. Before shipment of the BCI for installation on the Model 4 stepper, the BCI hardware was setup on an optical bench at SRL. The setup used the actual components, (optical parts and metal brackets & supports), that are designed to fit on the Model 4 stepper. The parts on the optical bench were in the same relative positions relative to each other as they were to be on the stepper. During final pre-shipment testing, an error in the signals was discovered. The error appears as a fluctuation in the output signal. The fluctuation is on the order of 5 to 15 degrees of

phase change. As a comparison, the normal turbulence signal from the BCI would be on the order of tenths of a degree of phase change.

BCI Installation and Evaluation on Model 4 Stepper:

The parts were shipped on April 16 and 17 and have been installed at the Model 4 at CXrL, (see Figure 2). The combined laser gauge/BCI system was demonstrated in open loop form.

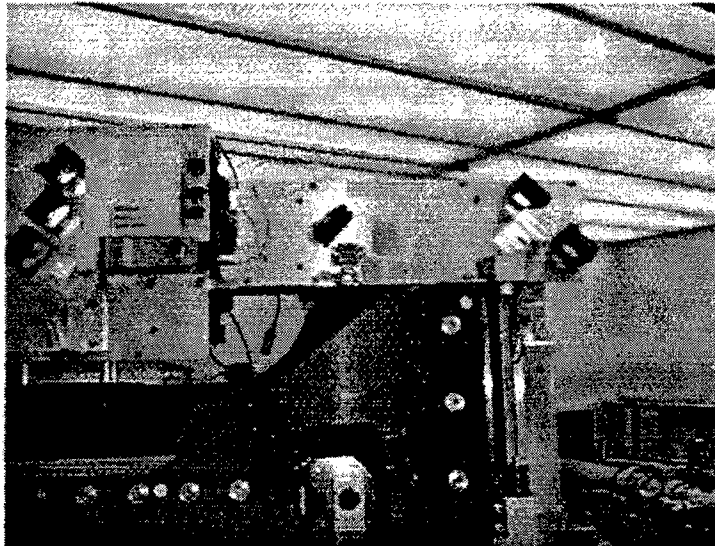


Figure 2: The BCI installed on the Model 4 Stepper at CXrL. The y-axis system, including both the HP laser gauge and the BCI, are mounted above the granite at the top of the photograph. The x-axis hardware at bottom center is visible through the opening in the granite.

μm of stage motion—or equivalently, 100 degrees per centimeter of motion. The precise value depends on both $\beta_{12} = (n_2 - n_1)/\rho$, that is, the dispersion of air and the value of the air density, ρ .

Fig. 3 presents a record of the BCI phase shift, (in degrees), as a function of time. The step jumps in phase occur when the stepper is displaced. With the exception of the first displacement, (which shifts the BCI phase from $\approx 87^\circ$ to $\approx 0^\circ$), all displacements are either $10000 \mu\text{m}$ or $\pm 20000 \mu\text{m}$. Table 1 lists the displacements and the refractive-index difference, $n_2 - n_1$, determined from the BCI measured phase changes at a pressure of 1 atmosphere, a temperature of 20°C , and a relative humidity of 50%. As indicated in Table 1, the anticipated value of $n_2 - n_1$ under these conditions is 4.14×10^{-6} . The measured values are in excellent agreement with this prediction. In fact, the deviation of the measured values from this prediction is smaller than the observed fluctuation of each measurement, (see Fig. 3). This demonstrates that the phase variations seen by the BCI are indeed associated with the dispersion of the air.

Details of BCI Evaluation on Model 4 Stepper:

BCI Response to Stage Motion:

A BCI critical demonstration that was performed for the first time at CXrL was the determination of the response of the BCI to stage motion. The sensitivity of the BCI fringe shift to stage motion is predicted to be

$$\partial f / \partial L = m \beta_{12} \rho / \lambda_2$$

where m is the number of one-way passes of the BCI beams through the BCI; for the installed system, $m = 4$. For $\beta_{21} = 4 \times 10^{-6}$, $\rho \approx 1 \text{ amagat}$, and $\lambda_2 = 532 \text{ nm}$, this fringe shift corresponds to approximately 10 mdeg per

Table 1: Refractive Index Difference Determined from the Data of Fig. 3. The value tabulated under "standard air" is the anticipated value of $n_2 - n_1$ for standard air pressure of 1 atm, a temperature of 20°C, and a relative humidity of 50%.

<i>Displacement (μm)</i>	$10^6 (n_2 - n_1)$
+10000	4.05
+10000	4.08
-20000	4.08
+20000	4.10
-20000	4.11
standard air (20C)	4.14

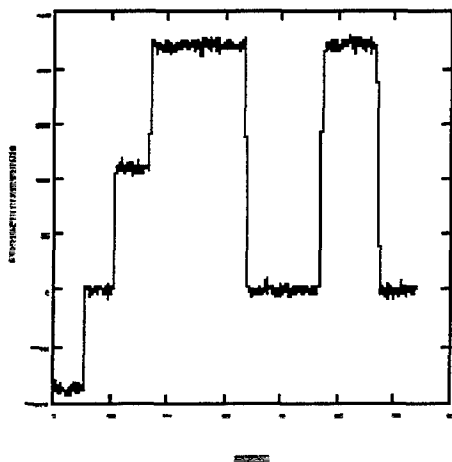


Figure 3: BCI Phase as a Function of Time, While Stage is Displaced Discretely, (Phase in Degrees Versus Time in Seconds)

In addition, the installation at CXrL greatly reduced the polarization leakage associated with the HP x interferometer of the Model 4 Stepper. The original configuration of the x interferometer included a 90° total internal reflection of the circularly polarized HP x beam by a prism. Such a reflection of circularly polarized light changes the polarization significantly. We removed the prism, replaced it by a mirror, and added two 633-nm quarter-wave plates, one immediately before the reflection and one immediately after the reflection. In this new configuration, the polarization leakage is greatly reduced. This improvement will enhance the capability of the Model 4 Stepper to write narrower lines that are oriented along y.

BCI Development Program Conclusions:

Phase 1 of the BCI development program has demonstrated that the BCI noninvasively interfaces optically, mechanically and electronically with all three axes, (x, y1 and y2), of the HP laser gauge. In addition, the BCI has met the tight space constraints imposed by the Model 4 stepper and the mechanical/optical interface with the HP laser gauge. The integration of the system on the Model 4 stepper was nearly flawless; the few mechanical inconsistencies that were encountered during installation were rapidly corrected on site. During the installation tests, the BCI has been experimentally shown to be a self-calibrating instrument that repeatably measures stage position in terms of air thickness and known air dispersion. The phase measured by the BCI is an absolute number that is equal to the path-length difference—expressed as a phase—between light waves of wavelengths 1064 and 532 nm. The BCI phase changes by approximately 100 degrees for every centimeter displacement of the stage; it accurately tracks the stage position as it is displaced macroscopically by many centimeters. The

theoretically predicted principles of the BCI have been demonstrated successfully: that the BCI measures changes of the air-path thickness, but is insensitive to mirror displacement; that the BCI signal, multiplied by the theoretically predicted scale factor, closely tracks variations in the baseline-interferometer signal that are due to air-density variations; and that, when multiplied by the same scale factor, the BCI noise level is significantly smaller than that of the baseline interferometer. The operation of the BCI has been demonstrated at a level of phase noise and systematic variations of $\pm 0.05^\circ$, which is equivalent to a stage displacement of ± 1.2 nm

In addition, the installation at CXrL greatly reduced the polarization leakage associated with the HP x interferometer of the Model 4 Stepper. This improvement promises to enhance the capability of the Model 4 Stepper to write narrower lines that are oriented along y.

BCI System Software:

The BCI utilizes a single DSP processor to collect and process the information from the BCI system and the HP laser system. Software was written for the DSP to read the current raw position of the stage through a digital interface with the existing HP Servo-Axis controller. The software also supports reading BCI data through analog inputs. The DSP software then combines the information to produce a corrected instantaneous position at a rate of 1KHz. This corrected position is then used as input to a PID motion control algorithm which servos the piezo driven alignment stage. The DSP also performs the appropriate coordinate translations to convert the three input data from the laser systems into the three output data required by the mechanical design.

Enhanced Global Alignment Software:

A global alignment algorithm similar to that used on the Model 3 machines was implemented on the Model 5. This algorithm was integrated with the existing alignment software and expanded to support multiple data sets for calculation with ALX, IBBI, or BCI data. The User Interface was also modified to support selection of the global alignment operating modes.

A005: SOW Task 3.2.1.4: Robotic Wafer Handler

A robotic wafer handling system that includes a proximity bake station will be designed and constructed in this task. Karl Suss America, (KSA), will design and build the system to SAL specifications, using an adaptation of their standard systems.

During March, 1997 SAL generated specifications and dimensions, which led to a formal quotation for the Material Handling System, (MHS), from Karl Suss America, (KSA), on 27 March, 1997. SAL worked closely with KSA, Sanders and SRL to determine the best mechanical interface. The result was a MHS design specified to be a standard KSA product planned to meet the beamline height specification of 1100 mm. The standard MHS should be more flexible in the future, should Sanders want to use it for other applications. Additionally, it is upgradable to a coat-develop station using standard KSA modules.

The conceptual design includes SMIF I/O and the Wafer/ Mask handling interface, as well as an environmental chamber set to cover the complete Model 5 Stepper, Robotic Wafer/Mask Interface and Bake Station subsystems.

Wafer Handler Robot and Interface (I/F) Hardware:

The design concept of the MHS includes a robot which allows a wafer transfer from input/output cassette stations to hot plates and cool plates and the transfer positions on the Model 4 and the test bed stepper. This module is not necessary for the Phase 1 stepper program, however SAL provided a conceptual design of a wafer handler robot and interface hardware for configurations including mask handling, SMIF or variable beamline heights.

Control Software for Wafer Handler Robot and I/F:

A TCP/IP based protocol was developed for communication between the Model 5 and the Wafer Handler. A command description, which utilizes this protocol, was defined. The system software was modified to support the new communication method and a User Interface Service Utility was developed to test and exercise the defined command set. Tests were performed both locally on the wafer handler system and remotely over the TCP/IP link to verify proper functionality.

Proximity Bake Station:

The Bake Station, (MHS), was specified to be as close to the standard product that KSA builds as possible. This allowed use of existing hardware and software with minimum redesign. It also provided for ease of maintenance for future support.

The main modules of the MHS are:

MHU: The MHU includes the robot, the end effector, the centering station and the machine control electronics.

Genmark Centering Station

Auto-sizing Cassette Station

HCV Module: This module includes two hot plates and one cool plate

Blank Module

KSA provided the software modifications for integration into the X-Ray stepper system. A major difference between the standard KSA product and that required here is SAL's tight specification for the hot plate. At this time KSA can not meet this specification. Additional R&D work is necessary.

The MHS was demonstrated and accepted, (except the hot plate), on 12 March.

A006: SOW Task 3.2.1.7.3: Composite Stage

A lower mass (when compared to the present granite stage) stage made of composite material will be designed. The material selection and stage design will be subcontracted by SAL to the University of Vermont.

A lower mass stage, (when compared to the present Impala granite stage), made of composite material should be designed. The material selection and stage design was subcontracted by SAL to the University of Vermont, (UVM).

An initial meeting with UVM mechanical engineering personnel was held on 26 March, 1997 to discuss the task and resources. A contract was signed with UVM on 30 April. Principal Investigator Dr. Dryver R. Huston, Co-Investigator Dr. Gerald Sullivan, a graduate student and an undergraduate student performed the work on this project. Dr. Huston was responsible for the overall project.

The team started with the detailed work on 21 May. The task has been completed and results and recommendations are described in the final report dated 31 Dec., 1998.

Design Composite Stage Upgrade:

The overall purpose of this project was to produce an alternative design for the impala granite Y-stage that is currently used in SAL's Model 4 X-Ray lithography stepper. A study was conducted of the mechanical and material properties of the existing Y-stage. This included simplified mechanical modeling, computer modeling, and experimental verification. Possible replacement materials that were examined included glass, ceramics, aluminum, synthetic granites, composites, and plastics.

Based on a variety of characteristics such as weight, stiffness, stability and manufacturability, it was decided that silicon carbide ceramic, and graphite epoxy composite are the best options for alternative Y-stage materials. Formal quotes are being solicited from Xinetics Inc. of Devens, MA for a silicon carbide Y-stage, and Vermont Composites of Bennington, VT for a graphite epoxy Y-stage.

A number of issues and possible design changes for fabricating a Y-stage for 300 mm wafer size stepper have also been identified.

A007: SOW Task 3.2.1.8: Stepper Performance Verification

This task includes verification of the performance of the improved Model 4 stepper at CXrL, both through overlay metrology using test exposures, (CXrL led task), and through MMIC device fabrication, (Sanders led task). Reticles for this work are to be supplied as GFE from the IBM AMF through the MMD program.

Characterization of Overlay:

CXrL made many efforts using several different techniques to characterize the overlay capability of the Model 4 stepper. The original intention was to use wafers from a previous Model 4 program, print the second level and measure the overlay with the Model 4 itself. These wafers had the first level printed with the Model 4, had been processed and SiO₂ marks etched. The second level was printed on the Model 4 using the same mask and the wafers were processed. Unfortunately, the first level was too difficult to read with the Model 4 once the second level was printed and developed.

CXrL then tried creating a new first level on Si wafers with SiO₂ etching using a mask from a previous program. The etching was done at the WCAM facility on campus. It was determined that the RIE etcher was too contaminated for this application and the marks produced were unsatisfactory.

Sanders agreed to provide CXrL with GaAs wafers containing Au overlay marks printed with an optical mask. CXrL tried two different resists for printing the second level: SAL 605 and APEX-E. The second level was printed using an X-Ray mask with corresponding overlay marks and the wafers were developed. The wafer was then inspected with the Model 4 for overlay. A definitive overlay number could not be obtained with a small number of data points. More wafers were spun, exposed and developed. During the course of the measurements on the Model 4, it was concluded that the overlay pattern is too small for the stepper optics to measure, thus giving incorrect overlay data.

It was decided to inspect the above-mentioned GaAs wafers in the CXrL SEM. CXrL has a Hitachi CD-SEM donated by Intel Corp. Unfortunately, what was necessary to be measured was Au under resist and the resist itself. This required a voltage out of range of the CD-SEM. The wafers were then inspected on CXrL's general purpose JEOL SEM. The measurements showed a systematic error that is mostly likely due to the JEOL computer program used to measure overlay.

CXrL has monitor wafers that were used during the device exposures that can be used for measuring overlay. The wafers were then wet etched. The Model 4 was unable to read the marks satisfactorily.

After exhausting all of the methods above, there are still several possibilities for obtaining overlay data, but there is no time remaining. The Model 4 stepper is currently out of operation for the installation of the BCI alignment system. The overlay performance of the Model 4 exposure tool, however, can also be judged by the working performance of the MMIC devices. The overlay capability of the Model 4 system is sufficient for functional MMIC devices with a critical dimension of 0.25 μm .

BCI Evaluation by CXrL:

CXrL supported installation and evaluation of the BCI on the Model 4 stepper.

There were two visits by SAL/SRL to CXrL associated with BCI installation efforts. The first visit took place in the second half of April, 1998. The BCI system was delivered to CXrL and mounted on the Model 4 stepper. CXrL assisted with the BCI installation.

The system included a new laser, (green and infrared Bichromatic laser), and BCI optics, (prisms, beam splitters, $\frac{1}{4}$ -wavelength plate, 2 BCI receivers, and new fiber optics cables connecting the BCI interferometer to BCI receivers). CXrL personnel performed some machining work on the BCI parts: slots and grooves in the mounting plates and trimming a few parts to eliminate their mechanical interference. The BCI laser subsequently failed, and was returned for repair.

The new BCI laser was installed and the whole system re-aligned. Additional parts had to be made at CXrL to facilitate proper positioning of some optical elements. The HP's $\frac{1}{4}$ -wavelength plate was shifted to direct the beams to the HP interferometer receivers. This allowed the X-Y travel initialization procedure to be fulfilled successfully. The signal of the original HP interferometric system was checked and found to work satisfactory over the whole range of X and Y travel.

The boards reading the signals from the BCI and HP receivers had bad channels, so all signals could not be read simultaneously. Using available channels, the BCI interferometer signals were obtained and were found satisfactory.

Characterization Reticles:

CXrL has determined the structures to be included in the characterization reticles. They include line/space resolution structures, "star" resolution structures, Prometrix structures, overlay structures and alignment structures.

The reticle design has been performed with software developed to automate the generation of line/space and star features. A pattern file in the CALMA stream format has been generated for the entire resolution test mask, which now comprises the following features:

- Line/space resolution structures
- Isolated and grouped lines
- Junctions of isolated and grouped lines
- Orthogonal lines
- Crossed lines
- Small features near lines with positive and negative tones
- CDs from 100 to 500 nm
- "Star" resolution structures with positive and negative tones
- Indices for resolution
- Prometrix structures with single and multiple lines and orthogonal sets of lines
- CDs from 100 to 500 nm
- Overlay structures
- Standard CXrL structures
- Vernier sets
- Alignment structures for ALX 100, ALX 70, ALX 50 and IBBI
- Redundant sets to improve processing yield
- Miscellaneous structures including fine lines over topography, and large gratings for development endpoint detection
- Surface profilometry pads
- "Niru's Fingers" quick CD test structures

The main groups of structures included in the characterization reticle are: overlay pattern, IBBI alignment marks, ALX Alignment marks and additional overlay targets, resolution chevrons, resolution star, Prometrix vertical and step pads. All structures were designed, generated, placed, and converted at CXrL, with the following exceptions: Klaus Simon of SAL designed the topography features; Niru Dandekar of Sanders suggested the "Fingers"; ALX targets were designed by SAL; and the IBBI marks were designed and generated by Euclid Moon at MIT. In connection with these last, we have adopted a file format conversion path in which MIT generates .CIF files, which are converted at CXrL to .SF, (GDSII stream files), for use on the e-beam tool, and to .CEL files, the format handled by CXrL's IC editor. Placement of the IBBI marks was done at CXrL.

In June of 1997, CXrL completed the design of all structures listed above, using ICED IC editor software. The design staff wrote code segments to expedite the generation of repetitive features, such as the resolution structures, and to incorporate them into ICED pattern files. Using these pattern files as subcells, they generated a complete layout for the mask, taking into consideration the geometry of the available mask blanks, the restrictions governing alignment target placement, and the need to measure stepper overlay at sites throughout the exposure field.

The inclusion of too many and varied structures when converting the entire pattern file to GDSII format for use by the mask shop would have resulted in large and unwieldy files. To improve file conversion efficiency and to minimize total file size, CXrL carried out the conversion cell by cell, and then generated placement information for each cell. The large sets of resolution lines constituted the greatest demands on write time and process control, and so were kept as distinct subcells. The mask shop at IBM Fishkill accepted the final pattern files for final conversion to a format compatible with their e-beam tool.

The IBM Fishkill mask shop wrote the pattern sent by CXrL onto a SiC membrane, mounted to a NIST standard glass ring, with an absorber pattern formed of TaSi. CXrL and SAL staff evaluated this mask in the SAL Model 4 stepper, by making prints of the whole pattern, examining the resolution structures, and attempting to perform second-level exposures aligned to the first printed level, to measure the overlay capabilities of the stepper.

The contrast at X-Ray wavelengths of the TaSi absorber layer, relative to the SiC/Cr carrier, is only about 3 for the current samples. This is quite low when compared to a mature, functional mask technology, such as Au absorber on a Si carrier, but our preliminary results show that it seems sufficient and that care in resist processing can overcome this limitation. Resolution test prints exhibited satisfactory linewidth down to about 200 nm; higher resolution structures may be present in some regions of the mask, but as these have not been required, they have not yet been examined in detail. Other structures on the mask, such as those for surface profilometry of resist images, are also satisfactory.

Images of wafers viewed by the Model 4 through the mask were found to be of insufficient quality for reliable and precise alignment of mask and wafer, and indeed in some cases to be near the limit of quality to allow setting exposure gap. Specifically, the optical contrast of the image of alignment structures on the wafer, relative to the rest of the wafer, was less than 2 for the case of etched GaAs coated with 500 nm of a Novolak-based resist. A good quality mask/wafer system, such as Si wafers viewed through polyimide mask windows, may have a contrast greater than 20:1. To test the possibility that the poor optical performance was due solely to the Cr metal layer on the mask, we also examined a SiC mask that lacked Cr. It showed better image quality, but not enough to provide reliable alignment. We suspect the high reflectance of SiC, not just its low transmittance, needs to be addressed. Presumably an antireflection coating could improve its performance. The test was completed in February 1998.

The mask was sent to IBM for Cr layer removal. The last tests with this mask do not show improvement sufficient to perform reliable mask/wafer gap setting and alignment.

Device Fabrication:

An approach for mask bias estimation is based on diffraction phenomena and processing conditions. Generally, the intensity level directly under the absorber edge is ~ 0.25 . Depending on the development conditions, the edge can be formed at different levels of intensity relative to the nominal dose, (usually more than 0.25), and as a consequence "imaging" the edge is shifted in to the illuminated, (open), area of the mask feature. Any feature in the resist formed under the absorber will be wider than that on the mask. To compensate for this, the opaque features on the mask have to be "positively" biased, which means that the absorber has to be made narrower by a two-sided bias, B , approximately calculated as

$$B = 2v(I)\sqrt{G\lambda/2},$$

where G and λ are gap and wavelength respectively, and $v(I)$ is a coefficient which depends on the relative intensity level. Usually, development is optimized at intensity levels in the range of 0.3 to 0.6. Calculations were performed for average wavelength of $\lambda = 9\text{\AA}$.

The required bias is greater as the mask/wafer gap increases and the higher the intensity level at which the line is formed during development. In general, a 0.3 – 0.6 intensity range is commonly used and for 15-30 μm gaps, the linewidth broadening could be expected in the range of 20 to 110nm.

The specific bias values to be introduced into the mask pattern depend on the process optimization and can be predicted on the basis of detailed simulation. An extensive set of runs of the aerial image was performed. The main scope of these efforts was to determine the optimal bias requirements for printing isolated lines and trenches of 250 and 150 nm CD in positive resist APEX-E. For this project, it has been assumed that the mask has a SiN carrier and TaSi absorber. The parameters for the simulation study are as follows:

Mask Carrier:	SiN, 2 μm thick, density 2.7 g/cm ³
Absorber:	TaSi, 0.495 μm thick, density 13.5 g/cm ³
Mask Pattern(s):	250 and 150 nm isolated lines and spaces
Resist:	APEX-E, 0.5 μm thick, density 1.11 g/cm ³
Mask Bias:	varied from ± 50 nm with 5 nm step
Mask-to-Wafer Gap:	20 μm

The dose absorbed in the resist was computed using the program *XPROCESS* from the CXrL Toolset. The resist dissolution during development was performed using *FastPhoto* based on a level set approach. The choice of delivered dose and development time is quite important as it influences the developed pattern sidewall slope. In order to assure the proper choice, a matrix grid simulation of delivered dose and development time was performed. For this simulation, an equal line and space pattern was employed for $\pm 5\%$, $\pm 10\%$, and $\pm 15\%$ CD control. The dose and the

development time were varied from 40 to 100 sec and from 60 to 80 mJ/cm² on to resist respectively. (Due to the absorption in the mask carrier (SiN), the corresponding exposure dose on the mask is 2.25 times higher, or 135 to 180 mJ/cm² respectively.)

On the basis of this simulation, the dose conditions have been chosen between 70 and 80 mJ/cm² with 60 and 40 sec development time respectively. For these conditions, the "nominal linewidth" on the mask was varied in the interval from 50 to 350 nm. The predicted CD linewidth was plotted as a function of the nominal linewidth. The dependence is linear with the coefficient being very close to 1. The line broadening manifests itself as an intercept. From this analysis, a bias of 33-38 nm has to be introduced for the linewidth range of 90 to 350 nm, and possibly, above that. The processing conditions were equivalent to 0.35 relative intensity level.

The experimental data obtained for SAL 605 on Si and GaAs wafers were analyzed. Similar to simulated results, a good linear dependence of printed linewidth versus nominal was observed. The linearity coefficient varied between 0.96 to 1.06 for all data, and a value of 1.0 was assigned.

The experimental results of linewidth broadening for 30, 25 and 15 μ m gap for SAL 605 resist on both Si and GaAs substrates and simulated results for APEX-E on Si substrate are compiled in Table 2. As it follows from the data, the linewidth broadening ranges from 54 to 92 nm for Si substrates and up to 120 nm for GaAs wafers.

This analysis clearly demonstrates:

- Bias is always positive - the lines on the mask are narrower than printed
- SAL 605 resist on Si substrates behaves reasonably consistent with dose levels of the aerial image for all gaps.
- SAL 605 resist on GaAs substrates exhibits more complicated behavior. This behavior is probably related to the GaAs/resist interface chemistry.

A bias of 50 nm was recommended for the new MMIC device mask.

Table 2: Experimental and Simulated Results for CD Linewidth Broadening

Dose, mJ/cm ² on mask			120	130	140	150	160	180
		Resist/Substrate	Linewidth Broadening, nm					
Gap, μ	30	SAL 605 on Si	92	81	75	61		
		SAL 605 on GaAs	120	105	93	90		
	25	SAL 605 on Si	77	84	71	69		
		SAL 605 on GaAs	70	58	57	45		
	20	APEX-E on Si					33	38
	15	SAL 605 on Si	81	75	62	54		
		SAL 605 on GaAs	44	25	23	0		

Another goal was to develop and support a lithographic process able to produce 0.25 μm T-gates and explore the possibility to produce 0.15 μm T-gates on GaAs wafers. The development of the process started with the "old" mask, (available from a previous program). The new mask was delivered in November 1997.

The SAL 605 resist was considered as the main resist. As an alternative, another negative resist, PN 114, was explored, but the final process remained to be based on SAL 605. Although, as a base for T-gate process development, the existing process developed at CXrL, (together with Sanders), was used as a starting point, substantial changes in the lithographic system required optimization.

Development of 0.25 μm T-gate process:

- One important change was switching to "bare" GaAs wafer without the protective layer used before, (on a previous program). The cleaning and surface preparation procedure was seriously modified and a new procedure resulted in substituting for the ammonia hydroxide, (NH_4OH), a combination of diluted Hydrochloric, (HCl), acid and organic solvent (acetone and IPA).
- Efforts were put in "widening" the processing window by modifying the post-apply-bake, (PAB), and post-exposure-bake, (PEB), temperatures: $T_{\text{PAB}} = 118^\circ\text{C}$ for 72 sec and $T_{\text{PEB}} = 108^\circ\text{C}$ for 60 sec.
- The low normality of the development solution, used before to protect the GaAs from degradation, required long development time, 3 to 5 minutes, and was causing significant resist swelling. The alternative procedure utilizing a higher developer concentration, (MF312 1:1), and short development time, (45 sec), was introduced. The higher concentration allowed minimizing the contact with the wafer providing sufficient protection of the GaAs surface and avoided resist swelling. The new procedure stabilized the process.
- The mask/wafer gap was reduced from 30-35 μm to 15-20 μm , improving CD control.

Implementation of the optimized procedure enabled us to print 200 nm features on bare GaAs surfaces in a reliable and repeatable way.

New device with 0.15 μm T-gates:

- A characterization process was performed to provide thinner resist layers, (275 nm instead of 500 nm), for lift-off process
- A higher PEB temperature, (120°C was required for SAL 605 to be compatible with an optical resist formed on the top of the exposed and developed X-Ray resist). The exploratory runs performed with higher PEB on SAL 605 showed some progress, but more work in optimization is needed.

An important property of the mask is the X-Ray contrast. To determine this quality of the masks produced by IBM for the project, the SiC test mask was compared with the new device mask, both fabricated at IBM. The new device mask is optically more transparent, easier to set the gap and should be easier to align. A set of exposures has been performed with different exposure doses using SAL 605 resist on Si and GaAs wafers. The remaining resist thickness formed after exposure and development was measured in "clear" (under the SiC membrane) and in "opaque", (under the absorber),

areas. Some resist losses, (45-55 nm) have been observed even after long exposures, ($>300\text{mJ}/\text{cm}^2$ on the mask), forming the final resist thickness at about the 445-455 nm level. Comparison of these masks shows that:

- The contrast of the SiC/Test mask is $\sim 5:1$.
- The new mask carrier is somewhat, ($\sim 10\%$), less transparent compared with the SiC/Test mask.
- The new mask absorber is $\sim 25\text{-}30\%$ less "opaque" compared with that of SiC test mask.
- Consequently, the new mask exhibits lower X-Ray contrast, $\sim 3:1$ compared with that of SiC test mask.

The new mask was used to make X-Ray prints. Six wafers were printed. Some non-uniformity of absorber opacity was observed, (even within same the line). Three more wafers were printed with the old mask. Results confirm lower X-Ray contrast of the new mask. The mask was sent back to IBM for inspection and characterization.

The total number of samples processed at CXrL for GaAs MMIC T-Gate process development was 185. More detailed information is presented in Table 3.

Substrate Type	Count
Silicon Monitor	85
GaAs Monitor	60
GaAs Mechanical	20
GaAs Device	20
Total	185

Table 3: Type and Number of Exposed Wafers at CXrL

MMIC Fabrication:

Design and Build of Masks for MMICs:

Test Mask with Tantalum Absorber on Silicon Carbide:

A silicon carbide test mask was built to test through the mask in-board alignment using SAL's ALX100 and ALX70 alignment targets. GaAs wafers were prepared with corresponding targets for alignment. Three test masks were supplied by IBM, (marked as DMS102: 26E 5, 29E 4 and 29E 6), during the 4th week of March 1997. These had refractory metal included in the stack of absorber layers. We observed that silicon carbide membranes were sufficiently transparent in the optical, (red), region, and alignment was achievable without a chrome layer in the stack. A second test mask with a thin chrome layer, on the order of 10 nm, was acceptable for alignment, although it caused significantly lower optical transmission.

MMIC Mask Design: Mix-and-Match Consideration for Large Field Sizes:

At the time of designing this mask described as DMS144, the IBBI hardware had been installed on the SAL stepper. The detectors and mirrors required to test the IBBI coexisted with the baseline ALX system. In addition, the scanning snout mechanism for the beamline also placed constraints on the field size. Therefore, it was timely to proceed with the MMIC mask design using a large field size for the gate mask.

Consistent with this direction, the throughput target defined for the next phase of this program dictated that we build a database for working with large fields and familiarize ourselves with the mix-and-match lithography issues. We elected to use the largest field size available within the infrastructure of X-Ray masks, and the mix-and-match tools such as the Ultratech Model 1500 1X stepper and the SAL Model 4 stepper. Specifically, we selected 29.7 X 11.6 mm field for Ultratech exposures. The gate mask was designed to have two of these fields placed next to each other. Figure 4 shows a 3 inch wafer map, where 8 Ultratech fields, or 4 SAL X-Ray stepper fields cover the

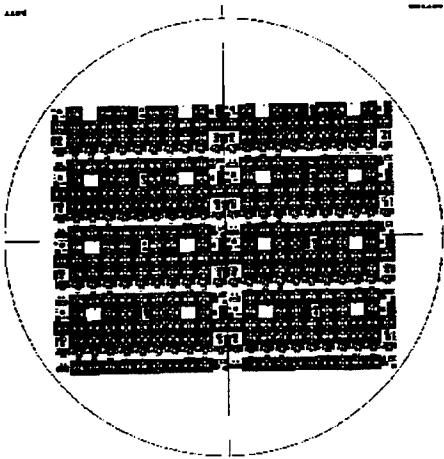


Figure 4: Four Fields of the SAL X-Ray Stepper Cover a 3 Inch GaAs Wafer

wafer. Details of a single photostepper field is shown in Figure 5. As the wafer size grows to 4 and 6 inches in the future, the complete fields will cover a larger percentage of the total wafer area. Therefore, no further effort was made in the current phase of the program to achieve more coverage on 3 inch wafers. The matching between two optical fields and one X-Ray field, however, depends on how the two optical fields are placed on the wafer. This was part of the assessment we made for a mix-and-match strategy for MMIC fabrication at high throughput levels. As a baseline, we followed our standard MMIC process flow and defined device areas with a mesa isolation photomask using a Canon contact/proximity aligner. This produced reference coordinates on wafer whose characteristics were derived from that of a chrome mask generated by a commercial vendor using a MEBES III mask writer. The optical fields of the Ultratech were printed at the ohmic metal level, using

alignment for every field. A pair of these fields were subsequently matched using a single field of the X-Ray gate mask.

MMIC Mask Description:

The details of the two LNA chips included on this mask are shown in Figures 6 and 7. The first LNA denoted by 144-1 is based on 0.25 micron gate length. The design is a 2 stage amplifier, and has a noise figure, (NF), of 1 dB over the 3 to 6 GHz frequency band, with about 22 dB associated gain. The second LNA denoted by 144-2 is based on 0.15 micron gate length. Its performance covers a bandwidth of several GHz in the millimeter wave region, (above 30 GHz), and it has a noise figure of 2.5 dB. In addition to these chips, there are test structures in a coplanar transmission line configuration that allow RF measurement after the wafer front-side process is complete. The ability to assess RF performance of devices without requiring the long cycle of flip-side process which includes wafer thinning and through wafer slot vias is very useful in the development phase of the MMIC fabrication.

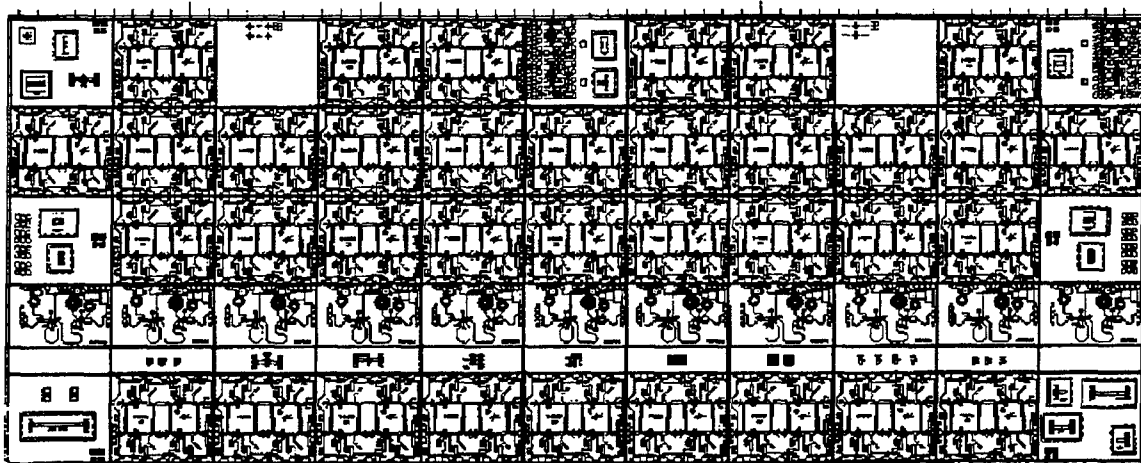


Figure 5: Detailed Layout of a Single Field of the MMIC Reticle for Ultratech 1 X Photostepper

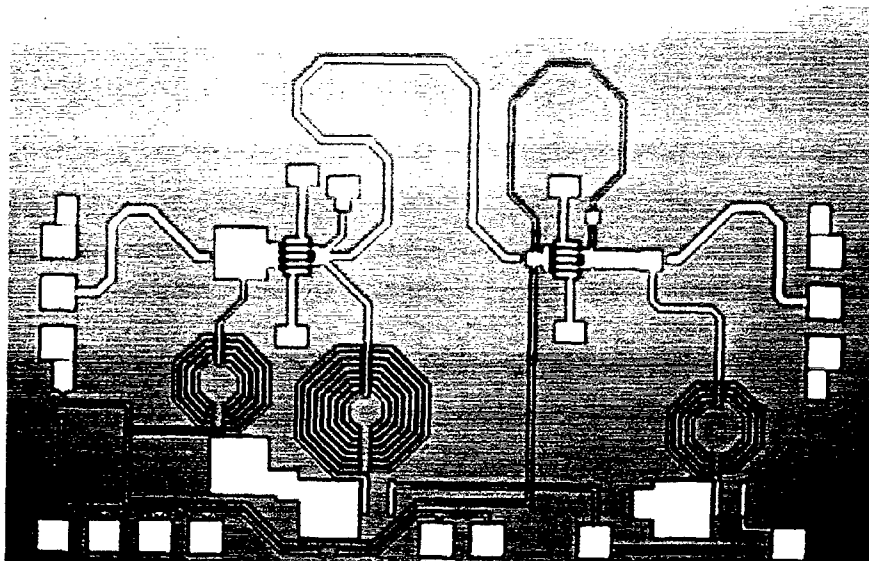


Figure 6: A 3-6 GHz LNA With an Expected Performance of 1 dB Noise Figure and 22 dB Associated Gain, Based on 0.25 micron Gate Length PHEMT Device

MMIC Mask
Procurement from
IBM's Advanced
Mask Facility:

The DMS144 MMIC mask experienced a long procurement cycle from the time of making a request in September, 1997. Due to difficulties in the mask fabrication process, a product mask was not produced until December 1997, when we requested the best result thus far to be supplied as an engineering mask to begin process development. This

mask, referred to as DMS144: 60A 4, had very low transmission for the alignment illumination in the alignment target areas. Even the mask/wafer gap setting procedure could not be performed on the SAL stepper using this mask. One of the reasons noted for low transmission was the presence of a 23 nm chrome layer. A work around solution was considered in February of 1998, involving removal of chrome in local areas around the alignment targets. This improved the transmission significantly, with alignment marks on one side showing 40% transmission, while the other side had only 20%. The reason for different transmission for the two sides was not resolved. For all device processing work in this program to date, we worked with this mask and

proceeded with developing the MMIC gate process. Finally, in April 1998 we received the product mask for DMS144 gate exposures, referred to as DMS144: 64A 4. The product mask has CDs and overlay characteristics that meet our requirement. However, initial exposures with this mask indicated lower contrast for this mask, (about 3:1), compared to the refractory metal absorber masks received in 1997 which had a contrast ratio of 5:1. With the current process parameters for SAL605 resist, we could not produce MMIC gate features due to excessive transmission through the absorber. We will look at modifying the resist process in the next program phase to adjust for the low contrast of the mask.

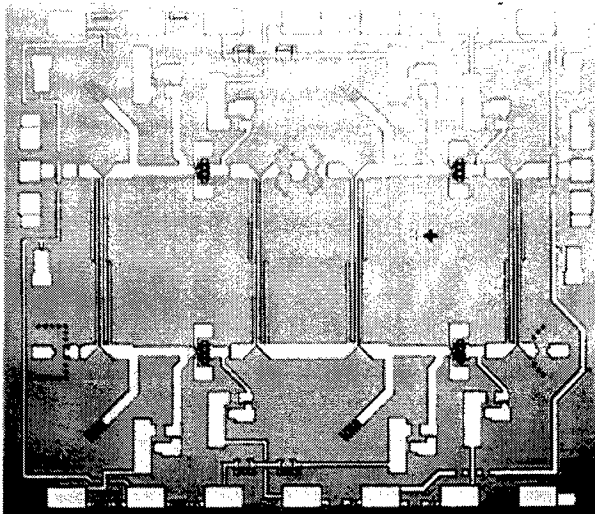


Figure 7: A Millimeter Wave (above 30 GHz) LNA Based on 0.15 micron Gate Length PHEMT Device. The expected performance for this chip has a noise figure of 2.5 dB across a broad bandwidth.

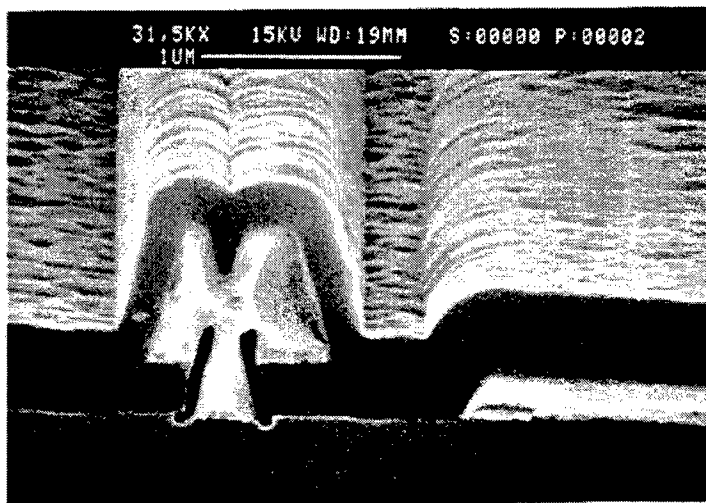


Figure 8: Cross Section of a T-Gate Fabricated Using a Dielectric Layer to Support the "T" Structure

T-Gate Fabrication Approach and Performance Trade-off:

There are two distinctly different approaches to fabricating T-gates. Figure 8 shows the cross section of a T-gate where the flared portion of the "T" shape is supported by a silicon nitride layer. To mimic the physical size of the T-gate produced by the electron beam direct-write process, the nitride layer must be relatively thick, on the order of 180 to 220 nm. The design of a T-gate along this line is described as the dielectric assisted T-gate (DAT-gate). The process to produce a DAT-gate is conceptually straight forward and requires conventional patterning of a single resist layer, (in our case SAL605 negative resist), with X-Ray exposures,

and following up with a dry etch process to transfer the gate critical dimension into the nitride layer. The wafer is then stripped of the resist and recoated for UV photolithographic definition of the T-head, which opens the T-head feature, about 1 micron wide, directly over the T-footprint. The profile created partly by the trench in the nitride layer and the resist opening defining the T-head is then filled with evaporated Ti/Pt/Au metalization. The selection of resists used in the two exposures is largely independent of each other, since the two resists are applied and stripped from wafers quite independently. We had originally developed this process for GaAs ion

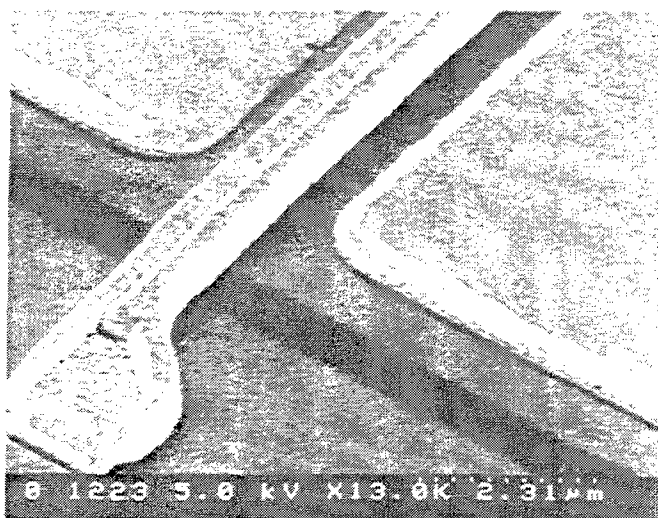


Figure 9 (a and b): T-Gate Fabrication Based on a Bilayer Resist Process, Resulting in a Free Standing "T" Structure. A device cell made up of six gates is also shown.

implanted MESFET devices. At gate lengths smaller than 0.25 micron, it is imperative that the gate process must be extendible to PHEMT material as well because of the majority of designs are based on MBE grown heterojunction layers which have intrinsically higher performance than the implanted MESFET process. The PHEMT material is also sensitive to surface conditions throughout the processing sequence, and also in the final resulting structure. We concluded that for the performance of X-Ray T-gate devices to be on par with electron beam direct-write process, the T-gate fabrication must follow the essential characteristics of a free standing T-gate structure, rather than one supported by a thick nitride layer. This is the rationale for developing a T-gate process based on patterning a bilayer resist structure where the gate footprint and the head feature are produced in two resist layers stacked one over another. An example of a T-gate fabricated along these lines is shown in Figure 9.

There are some references to T-gate fabrication using photolithography, which are relevant to the T-gate process discussed here. For example, deep UV lithography has been used to produce a T-gate using SAL601 negative resist for the

footprint definition, and again another layer of SAL601 for the "T" head. We selected the second exposure for T-head definition to be based on a UV stepper as opposed to a deep UV tool, for cost considerations as well as large field availability.

After all, with the exception of the gate footprint, all remaining levels of lithography for GaAs MMICs can be supported by a UV stepper such the Ultratech Model 1500. This has immediate implications to what resist pair we must base our T-gate process upon. The second resist layer must be UV sensitive, and therefore we cannot work with a resist common to X-Ray as well as UV exposures. We checked the compatibility of SAL605 defined footprint patterns with spin coating of a UV resist such as the Shipley 5214 as well as AZ 4110. Ideally, once the gate footprint feature is defined, it may not be modified during the course of the T-head definition in the second layer of resist

coated directly over the SAL605. However, in our investigation, some amount of intermixing between the two layers was found, and we considered a number options for a barrier layer between the two resists. At the conclusion of this development we settled on the use of 20 nm layer of silicon nitride as a barrier, and established a performance for the X-Ray T-gate which is equivalent to the electron beam direct-write process. In comparison to the electron beam direct-write process, the current X-Ray process involves added steps due to the barrier layer. However, batch processing considerations for the additional steps will still allow us to reap the throughput benefit of X-Ray lithography over electron beam lithography.

Results: MMIC Lot Fabrication:

A ten wafer lot, no. 97-208, of PHEMT, (Pseudomorphic High Electron Mobility Transistor), material was started. After defining the device areas by mesa isolation etch, ohmic contacts were formed. Table 4 shows data on contact resistance and sheet conductivity of the active device layers at the end of the ohmic metal alloying.

There were two more photostepper levels pertaining to the TaN resistor formation, after which the wafers were ready for X-Ray gate definition. We completed the T-gate process on this lot, and gathered data on overlay as well as device electrical characteristics.

Wafer no.	Sheet Rho, (ohms/ square)	Contact Rc, (ohm-mm)	Std dev % Sheet Rho	Std dev % Rc
97-208-1	261.87	0.16	0.57	8.19
97-208-2	263.29	0.16	0.92	8.83
97-208-3	265.08	0.16	1.05	8.60
97-208-4	260.65	0.15	0.96	8.38
97-208-5	261.26	0.16	0.90	8.15
97-208-6	259.19	0.16	0.70	12.57
97-208-7	257.09	0.16	0.86	11.16
97-208-8	258.32	0.15	0.73	9.69
97-208-9	259.19	0.16	0.86	8.99
97-208-10	256.53	0.16	0.99	5.68

Table 4: Sheet Conductivity and Contact Resistance on PHEMT Device lot 97-208 After the Ohmic Process

Overlay Measurements:

T-gate footprint as well as the T-gate head exposures were performed after aligning the respective patterns to the ohmic level as a reference. Residual errors in overlay were measured. Table 5 shows examples of these residual errors for the X-Ray gate footprint with respect to the ohmic level. The overlay for T-head is straight forward since the same Ultratech tool overlays one field over the other. The origin of chrome masks is also the same in this case. The overlay of the T-gate footprint on the other hand is complicated and has all mix-and-match issues combined together. The origins of X-Ray mask versus chrome mask including the electron beam writers used in their fabrication, and finally matching multiple fields of the photo stepper with a single field of X-Ray makes the analysis complicated.

Gate Exposure Field: Example 1

-.20	-.20	-.19	-.19	-.13
-.17	-.18	-.12	-.05	-.00
-.19	-.19	---	-.03	-.03
-.18	-.13	-.05	-.09	-.06
-.15	-.09	-.04	-.06	-.03
-.12	-.13	-.10	-.06	-.05

Gate Exposure Field: Example 2

+.03	+.02	+.09	+.07	+.09
+.08	+.12	+.07	+.11	+.09
+.04	+.09	+.13	+.08	+.07
-.06	-.05	-.03	-.08	-.07
-.12	-.15	-.12	-.03	-.06
-.16	-.15	-.12	-.05	-.05

Table 5: Residual Errors, (in microns), in Placement of the Gate Footprint in the Device Channels. Two examples are shown. The reference ohmic pattern was produced using two exposures from the Ultratech photo stepper for each of the gate fields.

The data shown in the examples was taken with no attempt at inputting off-set corrections after alignment. In other words, the exposures were performed when the stepper tool indicated a satisfactory alignment. We made this decision because the optical transmission for alignment on one side of the X-Ray mask was below the acceptable level, and required manual intervention by the operator to achieve final alignment. The data gathered in this exercise is very valuable, however, and already suggests what mix-and-match strategy is feasible. In Table 5, for example, we notice two Ultratech fields within the X-Ray field with clear identity of their own. Reducing the overlay errors will require a different technique to place the two ohmic level fields of the Ultratech, or else a different photo stepper with as large a field as the X-Ray reticle will be required. As a final comment, the placement accuracy for the X-Ray mask has been tightened due to the requirement from silicon digital applications. Specifically, our gate mask has placement accuracy better than 80 nm in x and y with respect to an ideal grid of coordinates. The 1X chrome masks procured from a commercial supplier and used in this mix-and-match will require similar tightening of placement accuracy before we will see lower residual errors in our application.

Device Results:

Wafers from lot 97-208 were completed through the T-gate process using SAL605 and AZ4110 resists in a bilayer process. There is one critical step before gate metalization, called wet recess etch used to adjust the device channel currents to target values. In PHEMT wafers, this is accomplished by using a built-in etch-stop layer in the stack of heterojunction layers grown by MBE. The final device characteristics not only depend on the gate length as the critical parameter, but also depend on the uniformity and accuracy of the recess etch to reach the target current values. Figure 10 shows a typical dc electrical characteristic of a PHEMT device. The parameters to be noted are the transconductance, G_m , which peaks near a small negative bias on the gate, the saturation current, and also the source resistance which is critical for a low noise device. Table 6 summarizes the data taken from wafers in the lot 97-208 and describes the saturation current, I_{dss} , the peak transconductance, G_m , and the gate bias at which this occurs. The source resistance is also tabulated.

Wafer #	Idss (mA/mm)	Gm peak (mS/mm)	Vg at peak Gm (volts)	Rs (Ohm-mm)
97-208-5	340 +/- 17	490 +/- 20	-0.30 +/- .025	.765 +/- .082
97-208-7	288 +/- 17	474 +/- 20	-0.20 +/- .022	.742 +/- .090
97-208-10	293 +/- 23	462 +/- 22	-0.19 +/- .015	.735 +/- .075

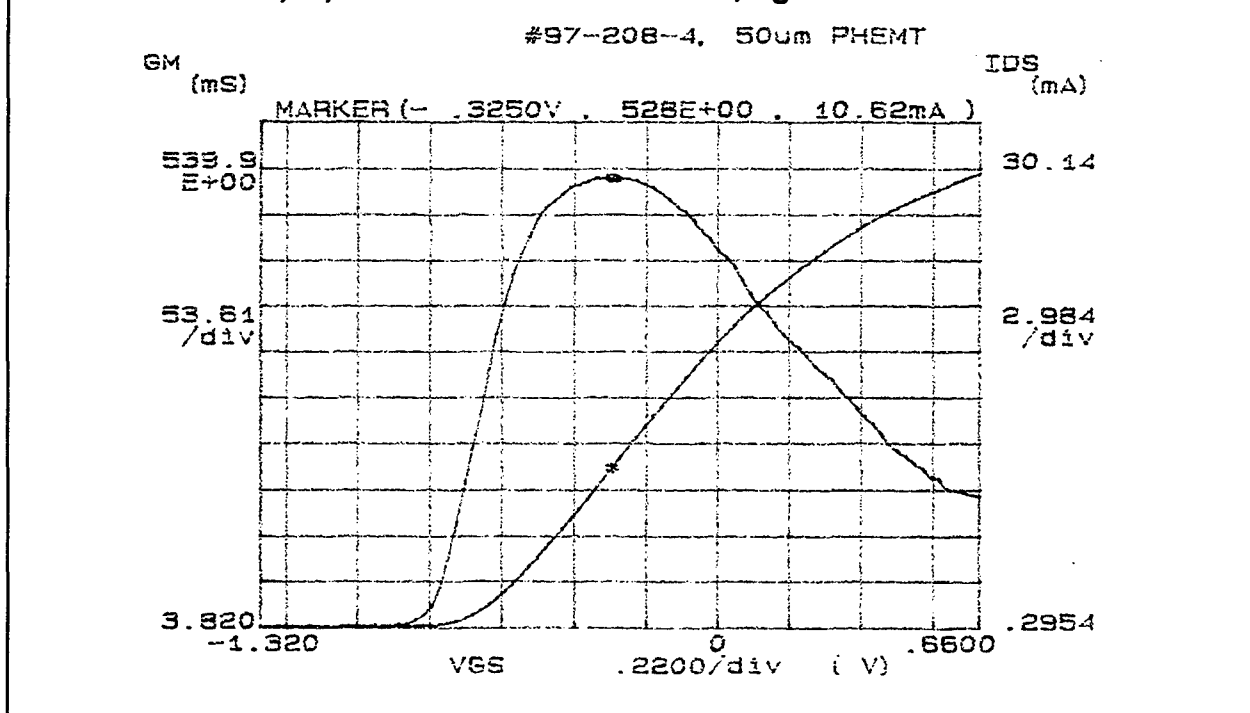
Table 6: PHEMT Device Characteristics Including Channel Currents, Transconductance, and Source Resistance

The data indicates that the 0.25 micron gate MMIC LNA design is adequately supported by the PHEMT device characteristics. The RF performance of the MMIC will be measured at the completion of fabrication, and will be the final proof of this assessment.

X-Ray Beam Divergence Impact on MMIC Device Fabrication:

Transitioning from the synchrotron based process to a point source X-Ray system, the need for reinventing the resist process must be minimized. Any differences in the arial dose profiles due to X-Ray sources must be anticipated and analyzed. Specifically, the projected divergence of the DPF point source must be contrasted with that of the synchrotron and the role played by local divergence in controlling the linewidth must be

Figure 10: PHEMT DC Electrical Characteristics Showing Transconductance, Gm, and Drain Current, Id, as a Function of Gate Bias, Vg



understood. Also, the effect of global divergence must be assessed, and requirements defined from the device fabrication point of view. This topic has special significance in

an X-Ray collimator design. We critically examined the impact of X-Ray beam divergence on the MMIC application, and noted the differences from the silicon industry's requirement.

The global divergence effects manifest in two categories. One is the overlay of X-Ray printed features with respect to the reference pattern on wafer. Second is the quality of lithography as judged by the slopes of the sidewalls of the patterned resist. The overlay issue must be addressed in mask fabrication. In its simplest form, the mask for printing with a point source will use an appropriate magnification factor to achieve the overlay. Corrections on the order of 20-25 ppm, (parts per million), will be required. The sidewall slopes in the resist pattern must be analyzed in the context of the characteristics of the post X-Ray process. For example, if the follow-on process is based on reactive ion etching, sputter deposition, or metal evaporation deposition, each of these processes will look at the resist sidewalls issue differently. MMIC gate

fabrication uses metal deposition by evaporation from a small source target, where the metal flux has strong directional effects. Figure 11 illustrates this subject for T-gate metalization. The lift-off after metal deposition is achieved through the retrograde slopes of the second level photoresist, which is a standard process in the GaAs MMIC industry. However, for the X-Ray printed T-gate stem, the sidewalls must have positive slopes all across the wafer. This is required for reliable step coverage of the metal, eliminating cracks or voids. A divergent X-Ray beam from a point source, without any collimation, will cause about 0 to 30 mrad of global divergence from the center of each exposure field to the edges, (30x30mm field). Additional collimation effort will limit the maximum divergence to 15 mrad, or even smaller values. The requirement of MMIC gate

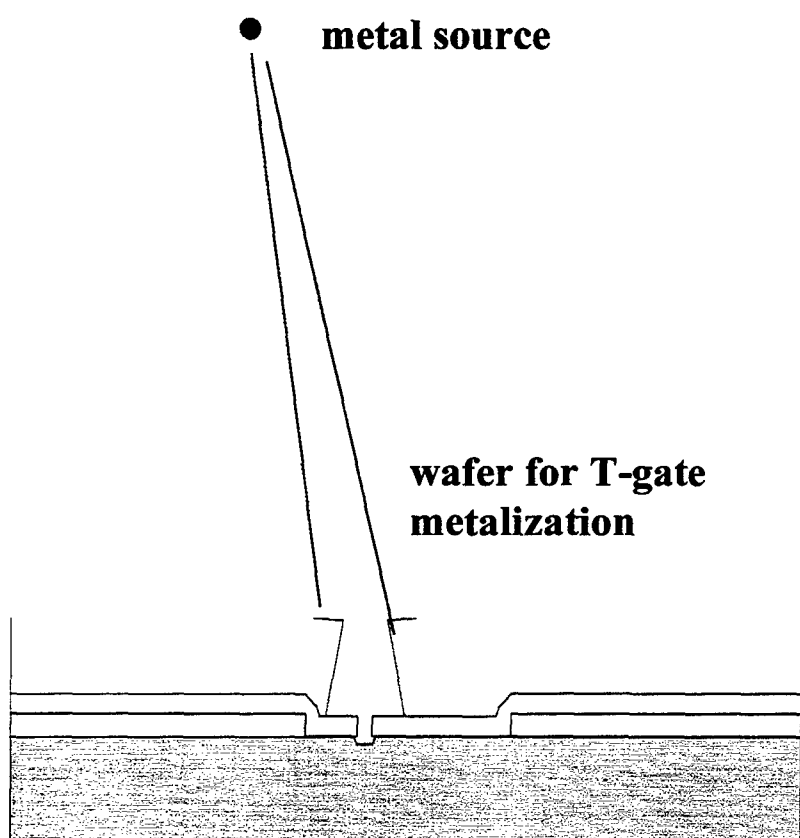


Figure 11: Schematic Diagram of MMIC Gate Metal Evaporation from a Source Showing the Requirement from a Resist Processes to Achieve Reliable Step Coverage as Well as Clean Lift-Off

fabrication will not be met this way, but will have to be addressed in the post pattern baking, (hard bake), of the X-Ray defined pattern. Quantitatively, the hard bake will

produce sloping sidewalls with an angle on the order of 50 mrad, which is consistent with the incident metal flux during the T-gate metalization process.

X-ray defined T-gates may be manufactured in the future with taller stems than currently achieved using electron beam direct writing. T-gates designed this way are expected to have lower parasitics and are most suited to millimeter wave applications. The divergence of the point source X-Ray beam, the sidewall slopes, and the modifications of these slopes using a hard bake after pattern formation will be even more important in demonstrating manufacturability of this process.

A008: SOW Task 3.2.2.1: Solid State Driver Development

An all solid state driver for the SRL dense plasma focus, (DPF), X-Ray point source will be designed and built, using a design developed on a previous program. Two pulse generator prototypes were previously built. The driver will contain 12 pulse generator units, (reduced from the original 24 because of achievement of improved conversion efficiency in the head).

Measure Voltage Rise Time Requirements:

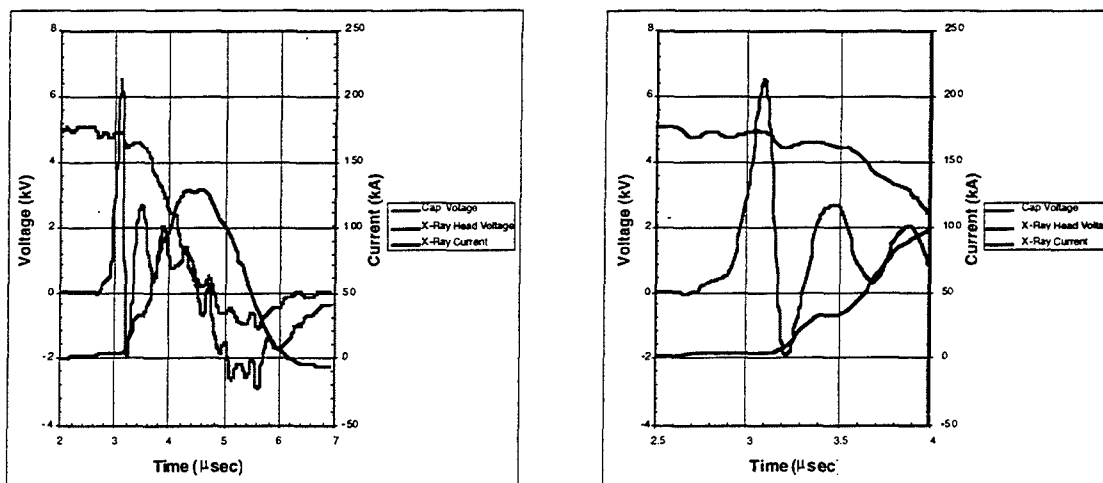
A key issue with the new solid-state driver is determining the voltage rise time across the DPF electrodes needed to initiate a discharge. There was concern that the all-solid-state driver might require an additional stage, a spiker, in order to sharpen the voltage rise time to the degree necessary to achieve the ignition characteristics of the spark gap driver.

The output cable of a standard Tektronix high voltage probe was modified so that measurements of voltage could be taken on the anode feed plate, and the signal could be carried to a high speed oscilloscope located outside of the spark gap driven DPF device in an EMP noise free environment. These measurements showed that voltage rise times on the order of 100 nsec are adequate for initiating discharges under standard operating conditions. These typically are at 1.3 torr neon fill pressure and 7 kV charge voltage on the power supply. Computer simulations have shown that 100 nsec rise times are achievable with the new solid-state driver.

The solid-state DPF driver, described in greater detail in a following section, was tested into the DPF X-Ray head in order to verify pulse discharge operation. Figure 12 shows the voltage and current waveforms across the DPF electrodes at 1.3 torr neon gas fill and 5 kV charge voltage. The left trace in Figure 12 shows the peak current through the X-Ray head was 130 kA at 5 kV charge voltage. A discharge was successfully initiated at this charge voltage. The voltage rise time across the electrodes before break down is 150 nsec, (10% to 90%).

This data shows the voltage wave front generated by the solid-state driver is adequate to trigger the DPF X-Ray source. The conclusion was that a rise time enhancing spiker would not be required with the new all-solid-state-driver.

Figure 12: Solid State Pulser Waveforms Driving the DPF X-Ray Source. Left trace shows the full discharge pulse. Right trace shows expanded view of voltage rise time across the DPF electrodes.



Design of Modules:

This section describes the solid-state power supply technology that was developed to drive the dense plasma focus X-Ray source. Table 7 summarizes the design goals of the DPF solid-state power supply that reflect improvements in X-Ray production efficiency in the DPF source over the course of the Phase I program. The power supply construct utilizes 12 parallel drive modules that together produce the fast-rising 8 kV, 225 kA electrical pulses needed to power the X-Ray source.

Table 7: DPF Solid State Power Supply Design Specifications

Nominal Parameters	Full Scale DPF Pulser 12 Module Configuration	15 kA Solid State Module Design Goals
Charge Voltage	8.0 kV	8 kV
Output Current	225 kA into live load	19 kA
Current Pulse Duration (half sine)	2.5 msec	2.5 msec
Current Rise time (10%- 90%)	< 700 nsec	< 700 nsec
Load Energy (per pulse)	>930 J	> 77 J
Pulse Recurrent Frequency	100 Hz	100 Hz
System Inductance	< 12 nH	N/A
Feedplate Inductance	< 2 nH	N/A
Pulser Inductance	< 10 nH	< 120 nH
Energy Transfer Efficiency	>80%	>80%
Pulser Life Expectancy	> 10 ⁹ shots	> 10 ⁹ shots

The circuit topology for the solid-state drive modules is based on fast-switching thyristor technology developed by ABB Semiconductors, Lenzberg, Switzerland. These high current thyristor switches are capable of switching tens of kiloamperes on the microsecond time scale as required by the DPF X-Ray source. A top-level schematic of the solid-state module is shown in Figure 13. It consists of a $2.4 \mu\text{F}$ storage capacitor switched by 3 series thyristors. The module output is connected to the X-Ray source through a ferrite isolator. Snubber diode circuits are also connected across the storage capacitor in order to clamp reverse voltage across the capacitor. This is a key design feature that ensures no reverse current flows through the X-Ray head during a discharge. This feature is necessary to improve electrode lifetime.

Figure 14 shows a photograph of the solid-state drive module. It measures 18 inches wide by 14 inches high by 42 inches long.

The test stand which supports the 12 module array is shown in the photograph in Figure 15. The test stand measures 120 inches wide by 108 inches high by 50 inches deep. It is fully instrumented and computer controlled.

Figure 13: Solid State Module Schematic Diagram. Twelve parallel modules make up the full power DPF driver.

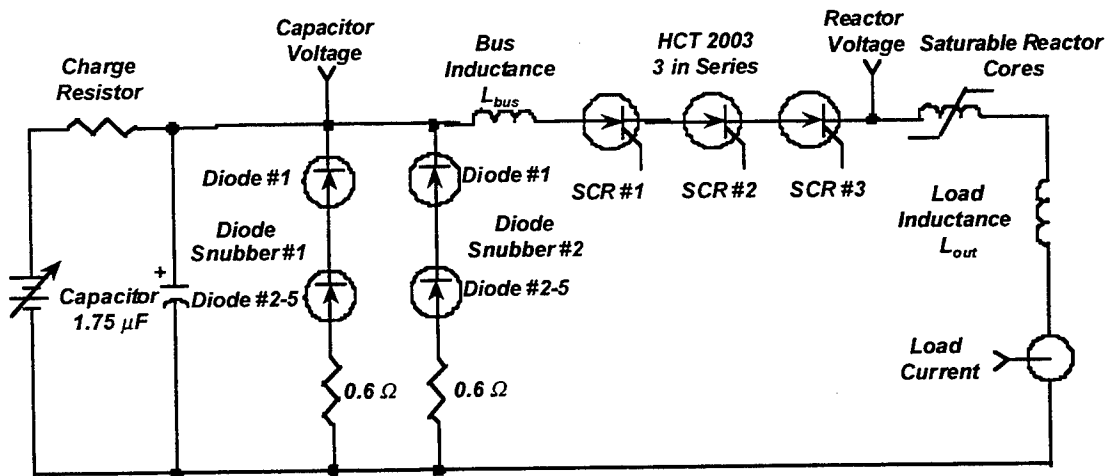


Figure 14: Photograph of the DPF Solid State Drive Module

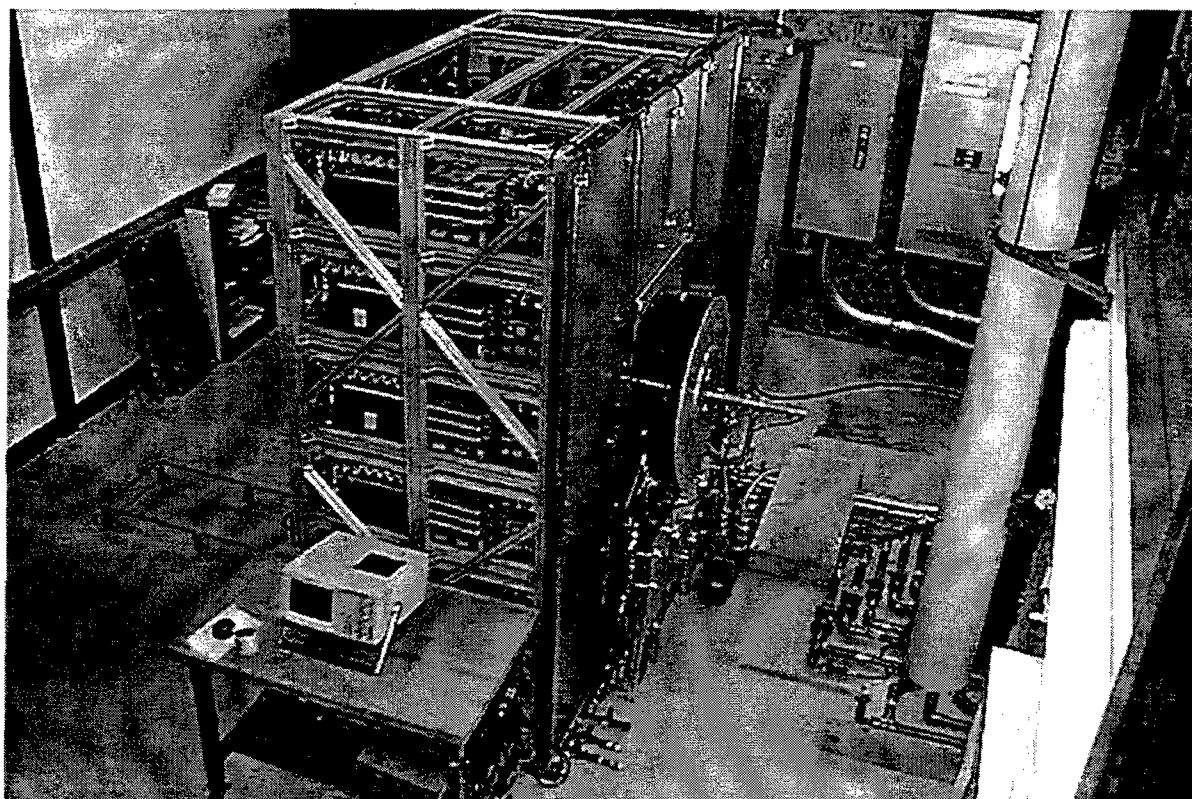
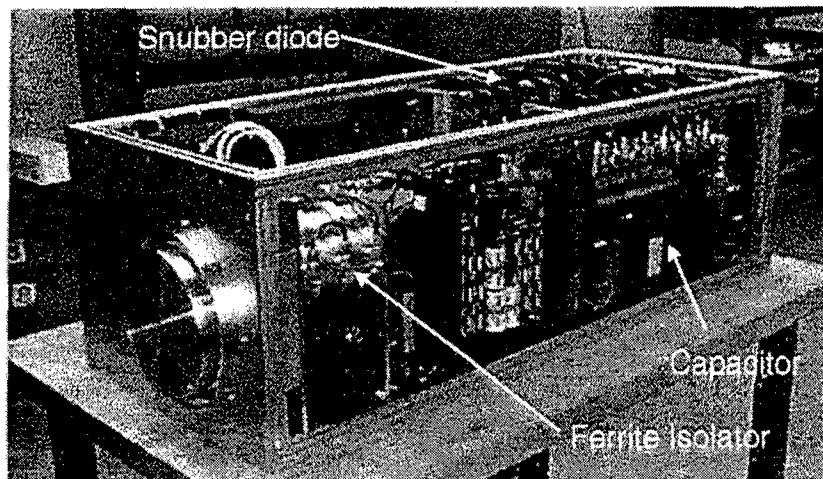


Figure 15: Photograph of the 12 Module Solid State Driver Test Bed

Solid State Driver Measurements:

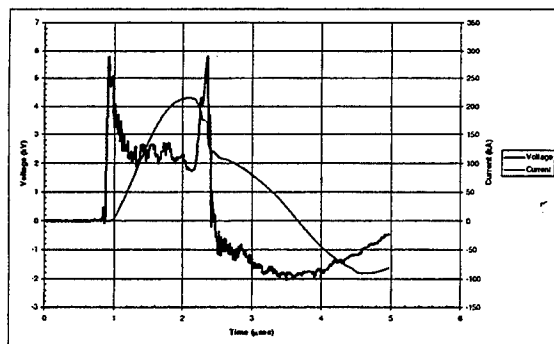
The performance specifications of the solid-state driver are based on the measured performance of the DPF X-Ray source driven by a conventional spark gap power supply. A DPF discharge waveform generated by the spark gap driver is shown in Figure 16. Computer modeling of solid-state driver performance, also shown in Figure 16, shows the solid-state driver will match closely the electrical performance of the spark gap test bed. Consequently, the solid-state power supply should produce X-Ray output comparable to that demonstrated by the spark gap driver. Note also that the solid-state driver waveform in Figure 16 shows no current reversal through the X-Ray head. This is key improvement that is critical for improving X-Ray electrode life.

Figure 17 shows a typical voltage and current waveform generated by the module into the resistive load. The nominal current rise time was 700 nsec, (10%-90%), to 13 kA peak current.

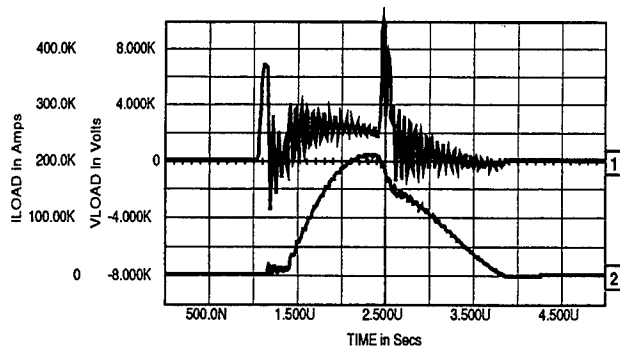
Studies on Phase II Deliverable Module Options:

Studies and experiments were conducted to narrow down choices for the design of the solid state driver for the deliverable machine. The principle goals of this work were to obtain a design which gave the same output in a more compact package using fewer modules. In particular, the overall height of the machine had to be below that of the overhead crane hook, which is 7.5 ft. The beam-line height was specified by SAL to be 1100 mm above floor level. The present all-solid-state machine has an overall height of 9 ft and a beam-line height of 1451 mm. Three potential architectures were identified. The first, would have used new high performance AZ thyristors developed by ABB. These thyristors should have readily supported a compact six module device.

Figure 16: Measured DPF Voltage and Current Waveforms Generated by a Spark Gap Power Supply, (left), and Simulated for the Solid State Supply, (right)



*Measured DPF Response
29 μ F charged to 7 kV*

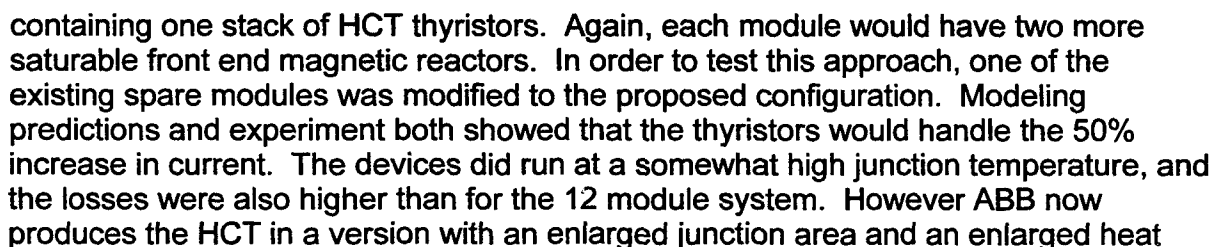


*SPICE Simulation of DPF Load Response
with solid-state driver charged to 7 kV
- Trace 1: V_{load} : 2 kV/div
- Trace 2: I_{load} : 50 kA/div
- Horizontal: 0.5 μ sec/div*

Unfortunately, early models tested at SRL did not meet promised specifications. Detailed tests were completed on a new AZ thyristor switch and its integral trigger

The second approach would again result in a six module device. The presently used HCT thyristors would be employed, but with two parallel stacks of thyristors in each module versus the present single stack. In order to maintain low inductance, two more saturable front end magnetic reactors would be added to the present two. The existing modules were designed so that the front end would accommodate two additional saturable reactors. Drawbacks to this approach include the cost of an additional thyristor stack with its set of trigger cards, and the fact the individual module would be quite heavy and bulky. Equal sharing of current between stacks without some kind of isolation was another concern.

Figure 17: Voltage and Current Waveforms Generated by the Solid State Module into a 0.25W Resistive Load



transfer area. It is expected that with this device, junction temperatures and system efficiencies will be in line with the present favorable value. Test are planned using these enhanced area thyristors.

The eight module architecture turns out to be quite favorable in terms of its spatial configuration. The modules would be arranged in two stacks of four. The individual modules would have the same height as the present modules. This turns out to place the beam height at the prescribed 1100 mm while allowing a 2.75" space beneath the support frame. This gives adequate space for passage of cooling, vacuum, gas, diagnostic, and control lines. The overall height of 6.38 ft falls below the 7.5 ft limit set by the overhead crane at the Sanders' facility. Each module would be somewhat wider than at present in order to accommodate the 50% increase in the number of capacitors which must be placed in each. The overall width of machine would increase from 91" to 114". The modules could have the same length in the beamline ("axial") dimension. However, in the interests of providing flexibility in design of the proposed lower inductance bus work, allowance is being made for a 4" increase in module length. The length of the machine in the axial direction would be increased by this distance plus an additional 9" to allow enclosure of the area where cooling, control, and power feeds enter the modules. This would put the overall length at 5 ft.

The favored approach has the final important advantage of being closest technically to the present configuration. Not only does that promise a reduced performance risk, but also the detailed design phase and the build phase should be able to proceed at an accelerated pace.

Dummy Load:

A dummy load was designed and built with the capability of testing the 12 module pulser at full power level before the DPF head is installed. This dummy load plugs into the same connections as will the DPF anode and cathode. Consequently, the power handling capacity of all of the current connections can be tested. The dummy load needs to have a 10 milliohm resistance and a 4 nanohenry inductance in order to match the characteristics of the baseline 5.5 cm anodes. In order to meet the high, 100 kW, power dissipation requirements while maintaining such low inductance, an unusual approach was called for. The load consists of a circular array of 57 thin wall, (4 mil), 1 ft long, stainless steel "hypodermic" tubes, (50 mil ID), set on a 14.2 inch diameter circle. Return current is provided through a surrounding 14.75" diameter copper cylinder which also serves as an electromagnetic shield. Cooling is provided by 100 psi, 16 gal per min water flowing through the "hypodermic" tubes. The flow enters and exists the dummy load through the same channels in the anode base that are used for anode cooling. The flow rate is also the same as is used for the anode.

A009: SOW Task 3.2.2.2: Source Lifetime Improvement

SRL will improve lifetime of the DPF head by conducting several lifetime enhancement studies, including anode material selection, cathode rod cooling, enhanced lifetime insulators, and enhanced lifetime chopper.

Anode Materials/Design Trade-Off:

A decision was made early in the program to concentrate first on anode output performance issues as opposed to material issues. If the output of the system could be improved without any decrease in lifetime of the anode, that would be equivalent to a lifetime increase. In fact, the measure of lifetime measured in shots is almost irrelevant. If one is concerned about downtime to change anodes, the important measure of lifetime is joules of X-Rays delivered per anode. Now that the time to replace an anode has been drastically reduced, even that measure is reduced in importance. The ultimate measure will be joules of X-Rays delivered per dollar cost. That cost should obviously include the cost of a new electrode or the cost of refurbishment, and the costs associated with changeover downtime. If, as in the case of the work reported below, selection of a new electrode design results in major machine designs change which carry a substantial cost reduction, then the true increase in joules delivered is not reflected in the measure as defined above.

Exploration of the phase space of anode geometry was expected to demand that a fair number of different anodes would have to be constructed. It was decided to make the anodes as inexpensively as possible. In order to accomplish this, they would be uncooled and they would be fashioned of the least expensive material that had demonstrated good performance in terms of output. The uncooled electrodes gave poor performance. Consequently a switch was made to cooled anode. In order to control costs, these anodes were built according to an older design which is suitable only for a relatively low repetition rate, (10 Hz, operation).

Degasser:

Evidence of melt was observed near the tip of the cooled anodes. Heat transfer calculations showed that the tips should never get close to the melting temperature. It was speculated that this could be the result of air trapped near the tip. A system for degassing water in the center electrode cooling circuit was designed, built, and placed in operation. If air is trapped near the tip of this electrode, then the amount of trapped air would increase during operation. Such an increase is expected because water flowing adjacent to the trapped air region becomes heated, releasing dissolved air. At 20 degrees C there are 18.7 standard ml of air per liter of water, and at 35 degrees C there are 15.6 ml per liter. Such air pockets would cause overheating, and consequently may be the root cause of some of the observed electrode melt and vaporization.

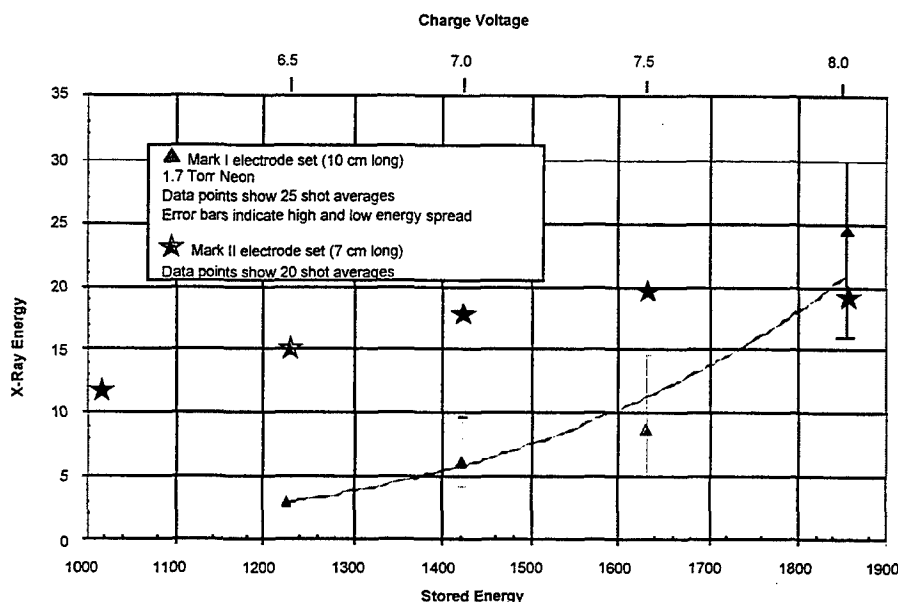
The degassing system employs a 20 ft high 6 in diameter PVC pipe which also serves as the cooling water reservoir. A diaphragm type vacuum pump evacuates a space at the top of the pipe. Water is extracted from the bottom of the pipe, and returned near the top. The height of the pipe allows pressures above atmospheric to be maintained throughout the cooling system, thereby avoiding problems with small air leaks, while the reservoir surface is held at sub-atmospheric pressure. Operation with the system showed that it effectively removed trapped air pockets. No further melting near the tips was observed on any of the anodes.

Short Anodes:

Efforts focused on evaluation of anodes which are shorter than the standard 9.5 cm length. Under the standard operating conditions for this electrode with the capacitor

bank charged to 8 kV and a chamber pressure of 1.7 torr, it was noted that the pinch generally occurs several hundred nanoseconds after the current maximum. It was believed that the pinch would be optimized if the current maximum occurred nearer to the time of peak current. Although lowered fill pressure does decrease the time to pinch, the scaling is weak. Consequently the option of using shorter electrodes was tried.

Figure 18: Comparison of Output versus Energy for Different Anode Lengths



A 7 cm anode was constructed and tested as a function of voltage and pressure. This electrode achieved 1.6% efficiency at the nominal 1800 joule input energy. This is better than the typical 1%, (rarely 1.5%), observed with the 9.5 cm anode. When the input energy was reduced to 57% of nominal by reducing the charge voltage, the efficiency dropped, but only to 1%. This behavior is illustrated in Figure 18.

Encouraged by these results, two of the six capacitor banks were disconnected. The efficiency was 2.4% at full charge of 1200 joules and 1.3% at a reduced voltage charge of 800 joules. This improvement of efficiency with some of the banks removed was quite unexpected, because the overall driver inductance is increased. Following this trend further, half of the banks were disconnected. With 700 joules in, the efficiency was 1.3 %. Finally, when four of the six banks were removed, the efficiency was poor for all conditions.

It was not clear that the optimum length had been reached, so an anode with a 5.5 cm length was built. Design changes in the anode had to be made in order to accommodate the cooling flow with the shorter length. The best performance was obtained when the tall cathode was in place. With half of the banks removed and an input energy of 700 joules, this electrode has shown efficiencies as high as 4%. The efficiency was typically 3% over series of runs, (mostly 50 pulses per burst, but some at 100 and some at 500 pulses per burst), totaling ~ 8000 shots. These results promised

a significance impact on the ultimate size and cost of DPF X-Ray sources. Because of nonlinear effects related to peak electrode heating, reduced input energy per pulse was also expected to have a favorable impact on electrode lifetime.

Evaluation of short anodes was continued. A 4 cm long anode was tested with half the capacitor bank connected. These results were not as good as those obtained with the 5.5 cm long anode which was typically 3% efficient. However, the 4 cm long anode gave the best performance seen so far with 1/3 of the bank connected. At a charge voltage of 7 kV, (457 joules input), the average output was 8 joules, which corresponds to 1.7% efficiency. Some individual pulses showed outputs as high as 20 joules, (4.3% efficient). It is believed that the variation of results is related to plasma ignition conditions. If this conjecture is true, the efficiencies seen on single shots point to the marked system improvements which would result from an optimized discharge triggering system.

The low cooling capacity short anodes had their differential pumping aperture severely eroded by the post pinch plasma. This is because the anode base designed to accommodate these anodes prevents the aperture from being moved far enough away from the tip. A tapered bore high cooling capacity 5.5 cm long anode which uses the high cooling capacity anode base was built. Because the high cooling capacity anode base has a relatively large bore to accommodate radial coolant feed to the anode, it was possible to accommodate propagation of the post pinch plasma as far as it can down the internal bore without striking an aperture. This distance is greater than the distance from the anode tip to the point where the anode enters the insulator. In order to make room for the cooling channels at the point where the anode enters the insulator, the bore had to be tapered from the 2.6 cm diameter value at the tip down to 1.4 cm at the insulator. The post pinch plasma did indeed propagate into the tapered region, and the erosion there was much less severe than was observed with the aperture. However, it was obvious that this was not a complete solution. A constant diameter bore, such as was used successfully with the long 9.5 cm long anodes, was required to avoid current concentrations on the internal walls and current contact with the differential pumping aperture during the zipper phase. This bore, hereafter referred to as a straight through bore, has to be reentrant in the sense that it must extend through the insulator into the anode base.

In order to accommodate the cooling channels in a straight through bore design, the external diameter of the anode must be increased in the region just above the point where it enters the insulator. The region of increased diameter is referred to as the skirt. Moreover, a new high cooling capacity anode base with a larger bore is required. Such a base was not available. Nonetheless, a 5.5 cm long, tapered bore anode with a "skirt" was built and tested in the existing high cooling capacity base with the smaller bore. The purpose of these experiments was to determine if this skirt would have a detrimental effect on the ignition phase of the discharge. Experiments with this anode showed the same 3% efficiency as an anode without the skirt. The percentage of shots with "dropouts" was markedly lower, (a few percent versus ~ ten percent), which implies that the field enhancement around the skirt encourages better ignition. Based on the success of these tests, it was decided that the new anode base for the all-solid-state driver would accommodate anodes with a skirt and a straight through bore.

A second electrode was built the same as the above electrode except that molybdenum replaces stainless steel. No performance output differences were observed between the stainless steel and the molybdenum model. The expected lifetime was also expected to be compromised by the tapered bore design. Because of this and schedule considerations, long term testing did not take place.

Finally, a series of test were conducted with anodes with an increased outer diameter. A potential advantage of larger diameter anodes is that the discharge energy is deposited over a larger area, which should result in enhanced lifetimes. A larger outside diameter 5.5 cm long anode was built and tested. The "fat" anode was tested over a pressure range of 1.0 to 1.9 torr and half bank charge voltages of 6 to 8 kV. The best performance was an average X-Ray output of 7 joules at 1.2 torr pressure and a 7.5 kV charge. Some individual shots were as high as 15 joules. It was expected that optimum performance would be at a lower pressure, (1.2 torr versus 1.3 to 1.5 torr), than was observed for the smaller diameter anode of the same length. This is because the driving magnetic field is reduced as the diameter is increased.

A shorter, 3.8 cm long stainless steel "fat" anode was then installed. The rundown velocity of the plasma in the 2" diameter device was expected to be slower than for the benchmark devices because the larger diameter reduces the driving magnetic pressure. The shorter length was chosen so that the slower plasma would reach the end of the electrode at the time of current peak. This timing is optimum for a good pinch. The device was fitted with a straight bore skirt to mimic the configuration in with a straight through bore. Tests were performed at 1.3 torr with half the capacitor banks disconnected and with both 7 kV and 8 kV charge voltage. The efficiency was about 1%, a factor of three below the benchmark results. The number of dropouts was larger than usual. This may be due to a change in ignition conditions resulting from the reduced anode cathode spacing. The test series had to be terminated because the aperture and base were bombarded by the plasma. This was to be expected because the low coolant base design does not allow the plasma to propagate freely in short anodes.

The above series of tests were quite successful. The overall efficiency of the machine was improved by a factor of three. Moreover, this improved efficiency was demonstrated with one half of the spark gap drivers removed. These results have had a major impact on the design of the all-solid-state laboratory prototype machine. The original plan to build a 24 modules device was thus modified. The new all-solid-state driven machine was built with only 12 modules.

Anode Gas Injection:

A new concept was developed for a mode of operation which will do away with differential pumping through the anode aperture and replace this with injection of neon through the anode aperture. Extraction of X-Rays through a differentially pumped aperture was conceived of as a means to minimize self absorption in the neon gas, and it works well. However, as the prospect for operation of this device with a collimator becomes more likely, the optimum configuration changes. The collimators require greater solid angles of X-Ray acceptance if they are to make up for their inherent losses. Moreover, the experience with synchrotrons indicates that reflecting surfaces must be in hard vacuum if they are to have long life. The hard vacuum requirement

can be met with a thin, very transmissive membrane which is located just beyond the chopper. This close spacing of the window, along with the reduced optimum neon pressure requirements with the short electrodes, implies neon transmission of approximately 88%, a very acceptable value. The enlarged aperture necessary to accommodate increased solid angle would impose a very expensive burden on the differential pumping. This is no longer the case if neon is injected through the anode aperture into the chamber as opposed to being extracted. In order to maintain pressure balance, this neon must be extracted from the chamber at the same rate as it is injected. This extraction is at a pressure at least 10 times higher than would be used for differential pumping, with the practical consequence that pump speed need only be 10% or less of that required for the differential pumping.

Reversing the gas flow will have other beneficial effects. If the flow is set at a value only four times the value presently used in differential pumping, the bore of the anode and the region around the anode tip will have a fresh charge of neon gas on every shot if the 133 Hz rate projected for the new machine is assumed. The fresh charge within the bore will insure that the X-Rays propagate through a medium which is uncontaminated with metal vapor, nanoparticles, or other contaminants. The pinch, which gathers gas from the region around the anode tip, will always be formed from uncontaminated gas. Finally, the fresh neon gas can be introduced into the chopper chamber in the neighborhood of the membrane in such a manner as to insure that no deposits are likely to ever form on the membrane.

In order to carry out tests of this new mode of operation, a new beam line was constructed. Previously, when the beam line was used with differential pumping, a small 2 mm gap at 0.2 torr pressure held off the voltage between the head and the beamline which is at ground potential. This small gap does not break down because the Paschen minimum for breakdown of neon at 4 torr is large compared to a gap pressure product of 0.04 torr cm. Without differential pumping, the beamline would be at the chamber pressure of 1.3 torr, and breakdown does occur at gap pressure product of 0.26 torr cm. Consequently a window, (25 micron of Al), was placed near the bottom of the anode base, followed by a several cm voltage holdoff gap, followed by the grounded beamline. The gap and the beam line were evacuated to 0.015 torr. As usual, the PIN diode detector was placed at the bottom of the beam line. However in this case, the PIN diode was not covered by a 25 micron of Al filter/attenuator because the window served this function.

The experiments were conducted using a 5.5 cm tapered bore stainless steel anode. X-Ray output and discharge traces were, as expected, the same as when the same anode was used with differential pumping. The benefits will be apparent with the new machine during long high repetition rate runs, and when a collimator is employed.

Water Cooled Cathode Rods:

Early in the program investigations were conducted to determine the cause of the missing pinches. One possibility was that various objects in the chamber, such water lines, could be disturbing the symmetry of the breakdown process. As a way of testing this, a grounded wire mesh cage was fitted over and outside of the cathode anode assembly. Test firing showed that this indeed made a marked improvement in the frequency of pinch occurrence.

The cage method was not survivable. After about five hundred shots a hole would be burned in the top of cage. It was reasoned that a cathode with rods several times longer than the anode length would have the same electrostatic shielding effect. Moreover, it would be survivable, because there is no top. An uncooled cathode with long stainless steel rods was built. The pinch reliability was again improved. Consequently the long rod cathode configuration was adopted for the rest of the program.

A design study of cooled cathodes was conducted. Cathodes having radiation cooled rods and a water cooled base were considered along with cathodes having water cooled rods and a water cooled base. The rods of a radiatively cooled cathode would rise to a temperature, which is repetition rate dependent, at which radiative transfer of heat from rods to the water cooled walls would be equal the heat input due to plasma bombardment and conduction. One candidate material for the radiating rods, tungsten, would survive the temperatures, but it would become extremely brittle. Detailed finite element calculations showed that considerable thermally generated mechanical stress would be developed in the water cooled base in which the rods would be mounted. There was also a possibility that thermionic emission from hot tungsten rods would initiate plasma discharge ahead of the pinch. Such discharges would interfere with the formation of strong pinches. Carbon rods appeared to be a better choice. Data shows it to have the lowest sputtering of any material, 8 x better than tungsten. Its low thermal conductivity would result in lower thermally generated stresses at the joint with the water cooled base. Calculations show that it will run cooler than tungsten. This is due to carbon's higher thermal emissivity. The lower temperature translates into lower vapor pressure. Much lower thermionic and secondary emission makes preignition less unlikely. Carbon residue does not stick like metal vapor. Finally carbon will not become brittle like tungsten will after operating hot. The fact that carbon is weak to start with was considered a drawback.

The overall concept of working with hot rods was abandoned. Computing the effects of heat transfer from hot rods on the gas flow was problematical. Moreover, no data would be available at high repetition rates until the all solid state machine was operational. Consequently, all further efforts were focused on water cooled cathodes. The first material chosen for the cooled rods was tungsten. An uncooled tall cathode version was built. It performed well in terms of X-Ray output. However, several of the rods spontaneously fractured near the base where there were discharge marks. The cause of this is unclear. Under the low repetition rate, short burst mode of operation that was employed, no part of the rod should have reached the embrittlement temperature. Whatever the cause, this behavior made tungsten unsuitable. Titanium was chosen next for the water cathode rod material because it has a low sputtering coefficient, four times less than that of tungsten, and second only to carbon. This should improve the life of the cathode beyond the current projected lifetime of 10^7 shots with tungsten. The low thermal conductivity was at first considered to be a drawback. However, calculations showed that average temperature drop across the wall would be only about 150 K.

An uncooled version of a long rod Ti cathode was built and tested. The objective of these tests was to determine if sputtered titanium vapor would have an effect on the X-

Ray output. (It was known from previous experiments that vapor from a copper anode decreases the X-Ray output by a factor of two from that observed with stainless steel, molybdenum, or tungsten.) No decrease in X-Ray output relative to the uncooled stainless steel and tungsten cathodes was observed. Consequently, a new Ti water cooled cathode was designed installed and tested. This device incorporated a tip flow header at the end of the rods which allows for flow return. In the interest of economy, the rods, actually hollow tubes, did not incorporate the flow control inserts that will be necessary at the high repetition rates which will only be accessible with the new all-solid-state machine. The addition of the tip flow header had no observable impact on the discharge characteristics. The measured X-Ray output was the same as with the uncooled cathodes, as expected. This cathode was examined after 10,000 shots. No wear, nor for that matter, discharge marks could be discerned.

Insulator Life Enhancement:

The average efficiency of the system would be improved if all X-Ray dropouts could be eliminated and the significant shot to shot variation reduced to a small variation about the best levels. The normal mode of initiating the DPF discharge is through a surface "sliding" discharge which takes place across the disk insulator separating the anode and cathode in response to application of voltage to the anode. It is believed that shot to shot variations in X-Ray output and occasional "drop outs" with no X-Ray output is due to the random statistics of initiation of the sliding discharge around the outer periphery of the insulator. In the normal mode of operation without spark plug ignition, a ring of plasma is generated at the 10 mil wide gap between the cathode edge and the insulator. This plasma propagates via a "sliding" discharge to the anode. This sliding discharge limits the lifetime of the insulator to an extrapolated value of 10^7 shots. During the roughly 100 ns time period during which the sliding discharge propagates across the insulator, the anode voltage is at the full capacitor charge voltage. Once the sliding discharge reaches the anode, the voltage collapses to roughly half this value for the duration of the "rundown" phase. This dwell at high voltage provides opportunity for discharge current to develop at other points between the anode and cathode. Occasional development of such unintended discharges was believed to be a possible cause of "drop outs", discharges which failed to produce X-Rays.

The goal of the "Improve Insulator Lifetime" task is to uniformly initiate a discharge above the insulator, thereby achieving more consistent DPF discharges, and eliminating any wear on the surface of the insulator. Three approaches for uniformly igniting discharges above the insulator were investigated. Two of these were hollow cathode methods. The third approach employed triggered spark gaps.

The first approach involved "passive" hollow cathodes. Before any actual attempt at triggering the main discharge was made, a number of benchtop experiments were performed to map out the characteristics of hollow cathode discharges in neon gas at the pressures of interest. Using cathodes fashioned from 1 cm diameter brass tubing, plasma ignition occurred when 256 V was applied between the cathode and the chamber wall, and the pressure was 1.7 torr. The running voltage was 234 V at 6 mA. Below 191 V, and 0.2 mA, the plasma extinguished. When operated at pressures below 2 torr, a glowing line was observed on axis, and no glow was observed in contact with the walls. The opposite configuration was observed from 2 to 6 torr. Operation below 0.5 torr was not possible.

A radially orientated set of three sided rectangular cavities were machined into the base of an old stainless steel cathode, just above the glass insulator that separates the cathode from the anode. The cathode was fired in DPF mode at 1.7 torr to determine if plasma would ignite in these cavities during the rise of the pulse thereby providing a beam of plasma and electrons to uniformly ignite the main discharge above the insulator. No differences in performance were observed from normal operation.

The second approach involves active hollow cathodes. These cathodes are already on when the DPF discharge is fired. A ring of 16 hollow cathodes was constructed, (see Figure 19 below).

The ring was mounted outside of and coaxial with the ring of 32 cathode rods. Axial placement of the ring was just above the cathode base to which the cathode rods are brazed. The hollow cathodes were orientated so that their discharge was in the radial direction in between every other cathode bar. The cathode bars served as the anode for this discharge. The cathodes were run DC with 1 ma going to each with an applied potential of 250 volts. They each were ballasted with a 20 kW resistor to insure current sharing from the common supply. Each hollow cathode was provided with a 0.5 μ F capacitor to ground so that a much larger current could be momentarily provided when the DPF anode goes to high positive potential. A preliminary survivability test showed no problems during single shot firing of the DPF at normal 8 kV voltage. Again, there was no marked difference in the DPF performance with and without the sustaining hollow cathode drive voltage applied.

At about the same time as the hollow cathode work was being carried out in Somerville MA, Dan Birx, working in SRL's California division, was developing coaxial plasma thrusters, and DPF EUV lithography sources based on very small DPF discharges. He had been obtaining good ignition results by mounting a circular array of surface discharge spark plugs around the base of his cathode at a short distance above his insulator. The plasma is initiated symmetrically in the gas, probably due to either UV preionization or to injection of plasma into the gap between the electrodes. In order to emulate his results, an uncooled cathode containing an array of 20 spark plugs was designed. The plugs are orientated with their axes in the radial direction such that tip of their center electrodes are even with the inner diameter of the ring. The tips are set 1.5 cm above the surface of the insulator. The plugs themselves are miniature commercial plugs which have been specially modified to insure a surface breakdown across the insulator separating the center electrode and the ground electrode.

An existing magnetic compression pulser, the Slam 8 power supply, was modified to power the spark plugs. A vacuum feedthrough for the ten spark plug leads was constructed in house. The Slam 8 power supply provided 4 kV pulse to the plugs. Each plug was isolated from the common feed by a 500 pf capacitor. This arrangement insured that the first plug to fire would not take up all the energy. The system was first tested in air, and then in the vacuum chamber at 1.5 torr Ne pressure. Test firing was conducted at repetition rates up to 50 Hz without any difficulty. Jitter between the firing of plugs was typically less than 0.5 μ s. Because it was expected that the suitable operation will be achieved with the plugs firing up to 10 μ s before the main DPF discharge, this value of jitter was acceptable. The discharge from each plug lasted

about 200 ns at a peak current of 9 A. The discharge produced by the plugs could be observed through a window in the vacuum chamber. The visual impression is that a cylinder of plasma ~ 2 cm in diameter is projected across the space between the plug tip and the anode surface.

Assuming that the ignition will be centered at the plane intersection all of the spark plug tips, it would be expected that an anode of a given length would behave like an anode that was 1.5 cm shorter. Hence, tests were conducted using a 7 cm long anode in the expectation that performance would be similar to a 5.5 cm long anode. The tests were conducted under the same conditions which gave superior performance with the 5.5 cm anode.

A time delay unit was employed to delay firing of the main discharge with respect to the firing of the sparks. Delays of from 0.5 μ s to 18 μ s were employed. Over this entire range of delays, performance was similar to the 5.5 cm long anodes with X-Ray production efficiency > 3%. When the trigger system was not fired, X-Ray production efficiency decreased to the ~ 2.5 % values previously observed for the 7 cm long anode under the same conditions. If the trigger system is fired, the leading edge voltage spike characteristic of the sliding discharge disappears, as expected.

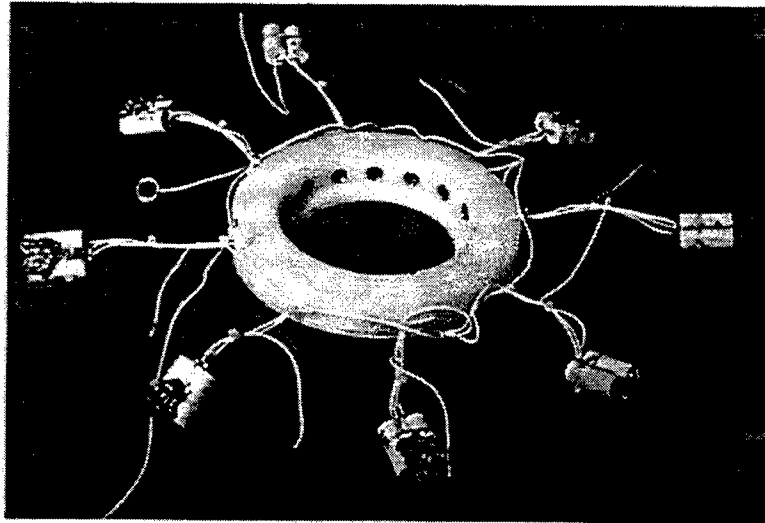
Contrary to expectations, the fraction of dropouts was independent of whether or not the trigger system was fired. A possible explanation for this would be arcing of one or more of the spark plug lines, possible at the vacuum feedthrough. Given the excellent low drop out performance obtained if the anode is equipped with a skirt, it was decided not to further pursue the active ignition option during the Phase 1 program.

Chopper Life Enhancement:

Design changes were identified which would greatly improve the accuracy and stability of alignment between the drive motor shafts and the shafts of the Ferrofluidic vacuum feedthroughs to the chopper wheels. In the previous program, lack of precise alignment led to premature failure of the bearings. One of several critical components to the new concept is an innovative insulating coupling with improved torsional stiffness.

The chopper motor housings are now mounted to the Rigaku vacuum feed-through housings in contrast to the previous configuration in which the motor housings were mounted to the vacuum casing surrounding the chopper. With this change, alignment between the vacuum feedthroughs and the motors will not be changed by the small deflections of the chopper housing when a vacuum is applied. The chopper housing has been stiffened so as to reduce deflections. A new design has been implemented for the insulating coupling between the vacuum feed-through shaft and the motor shaft. It is much shorter, and it is much more torsionally rigid. A DVT was carried out to demonstrate that this coupling would withstand the pinch voltages developed by the DPF discharge. This DVT was performed by subjecting the coupling to the actual pinch voltage, because the narrowness of the voltage spike precludes measurement of its actual magnitude given the bandwidth of commercial probes. Adjustment means have been implemented so as to allow alignment of the shafts to sub-mil accuracy. The whole system was assembled and adjusted to give shaft alignment better than a mil in order to obtain long bearing life. Previously, the air cooling which was used for the

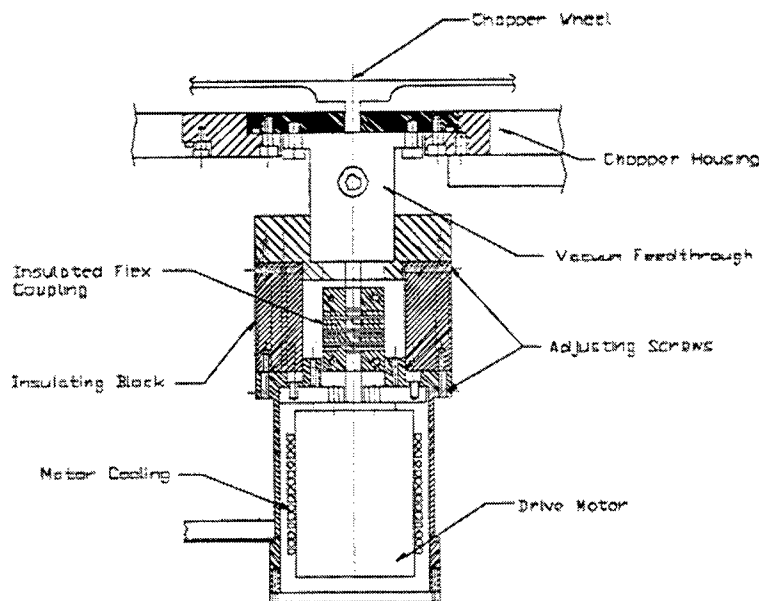
Figure 19: Hollow Cathode Array with Pulse Discharge Capacitors



motor housings was found to be marginal. Water cooling lines have now been applied to the motor housings. These features are illustrated in Figure 20.

The chopper was brought on line for bench testing. Full synchronization of the two

Figure 20: Chopper Coupling



wheels at the design speed of 9000 rpm was achieved. The Rigaku ferrofluidic vacuum feedthroughs exhibited high drag, and they were noisy. After several days operation the drag increased to the point where synchronization could no longer be maintained.

The feedthroughs were sent back to the manufacturer. They determined that the bearing were defective and admitted that a number of customers have been having similar problems. Apparently "feed" of lubricant to the bearing on the vacuum side is inadequate. A second issue is that the drag of the feedthroughs was three times higher than specifications, even before bearing failure. (This had, during the previous program, necessitated replacement of the original motors and significant upgrades to the motor drivers).

The manufacturer promised to supply new units with improved bearings at no cost and to pay for the remounting of the wheels. The new units would also have design changes which would reduce the drag by a factor of three from the original specification. New feedthroughs were delivered just at the end of the first phase of the current program, so no further tests could be performed.

A010: SOW Task 3.2.2.3: Source Testing to Verify X-Ray Output

This task includes fabrication of EMI enclosures, power supplies, power feeds, and supporting systems for operation of the solid state driver. The testing of the driver both into a dummy load and into the DPF head are included. Characterization of X-Ray output will be carried out by MIT under subcontract from SRL.

EMI enclosures, Power Supplies, Power Feeds, and Supporting Systems:

DPF Base and Power Feed:

Basic Architecture:

A system power feed architecture was developed to allow simple integration of the outputs of the twelve pulse power modules. The modules are mounted in two vertical racks with six modules stacked one above the other in each rack. The dense plasma focus head and surrounding vacuum chamber are placed midway between the two racks, at a position equal to half the height of the module stack. A rectangular three component parallel plate transmission line, the triplate, covers the output ends of each rack and the space between the racks. The center plate and the one of the exterior plates, the one facing the modules, carry the pulse current. The outer plate acts as an electrostatic shield. The output end of each module is equipped with a specially designed high voltage, high current capable coaxial connector which mates with a corresponding connector on the triplate. The coaxial connection between the modules and the pulse power distribution plate is "blind". No bolts or fasteners are necessary to make the high current connection when a module is placed on its frame and slid into its position.

Module Frame:

The frame was constructed using a commercial system of aluminum extrusions. Components are held together with a system of fittings and screw fasteners. This design allows for accurate construction and ease adjustment and transport. Structural calculations were performed for the system during the design phase. Each of the frames sit on a welded aluminum "I" beam structure which is raised two and a half inches above the floor on adjustable wedges. The space below this structure provides

a pathway for introduction of the various power, cooling, vacuum, and control lines to the machine.

The coaxial connectors on modules slide into contact with the triplate under the guidance of rails on which the modules are mounted. The critical tolerance for the coaxial connectors to mate up is that lateral offset had to be less than 20 mils. In order to insure that such accuracy can be met, the guide rails on which the modules slide were made to mate with holes machined into the triplate which were accurately placed with respect to holes for the coaxial connectors.

Feed Plates:

The triplate design was completed following detailed modeling of possible field enhancements using finite element calculations. High fields, through coronal erosion, could compromise the long term life of the insulation. Polypropylene was selected for the intra-plate insulating material because of its low dielectric heating loss and because of its low coefficient of thermal expansion. This later parameter is important because critical, 1/16" features machined into these sheets must match up with corresponding features on the aluminum feed plates over scale lengths of 10 ft. The dielectric sheets will be 3/16" thick. All joints with adjacent sheets take place via three corresponding steps machined in the sheets. The steps are 1/16" high. Consequently, wherever there is a step, there is a 2/16" of insulation and 1/16" of air in a narrow, less than 1/16" gap. Unfortunately this scheme does not work with crossing overlaps. Such overlaps, which would result in 1/16" of insulation and 2/16" of air at an overlap, are not allowed. Because the height of the laboratory prototype is greater than the standard 8' sheet length, a special mill run of longer sheets was ordered so that crossing overlaps could be avoided.

The insulation of the triplate must join with the insulation of the coaxial connectors and with the insulation of various bolts that pierce the triplate and hold the system together. Insulation overlap, similar to that described above was used for these joints also. A mock up of a portion of the feed plate was built. The mockup was tested for voltage holdoff and for fit with the connectors on the module before building of the full size plate commenced.

Vacuum System:

The vacuum system was designed to meet a number of constraints. The chamber needed to be cooled so as to handle a large heat load. The cooling had to be equipped with diagnostics so that the cooling provided with the deliverable machine could be optimized. The shape of the chamber had to be such as to provide for proper recirculation of the working gas at high repetitive pulse rates. The chamber had to allow rapid, no tools needed, access to the electrodes so that replacement could be effected with a minimum in down time. The pumping system had to allow for the high, through the anode, gas feeds which could possibly obviate any need for a chopper. The system needed to be equipped with instruments and controls so that all functions and states of readiness could be under computer control, while all self protective features were hard wired.

The vacuum chamber is a stainless steel cylinder which sits on top of the cathode base. Vacuum seal to the top of the cathode base is effected with a concentric pair of O-rings.

A differential pumping channel is provided between this O-ring pair. This feature allows good vacuum to be reached and it greatly simplifies leak detection. A set of four pneumatic toggling clamps press the chamber base against the cylindrical cathode base. A second set of pneumatic clamps press the cathode base against the transmission line insulation, where a second pair of O-rings also effect a vacuum seal. The cathode base makes current connection to the ground transmission line by means of "Multilam" finger stock on its edge. The toggling feature of the clamps insure that lockdown is maintained even if pneumatic pressure should be lost. This clamping system allows for almost instant removal or installation of the chamber, and if desired, the cathode. This new system replaces the arrangement of more that 40 bolts on the spark gap driven source. These bolts had to be carefully torqued down in a sequence of small increments in order to effect a vacuum seal and current connection using copper gaskets.

The vacuum system is designed to handle much higher gas flows, up to 80 scc/s versus 5 scc/s, that were used heretofore. This increased flow is achieved using a much smaller forepump, (21 cfm versus 145 cfm), than before. There are two reasons for this improvement. Firstly, gas is evacuated at higher pressure than before. It is now extracted directly from the chamber, which is held at an operating pressure of 1.3 torr, after it is introduced through the anode. Previously, gas was extracted from a beamline at low, 0.2 torr pressure, after it flowed through the anode from the chamber. Secondly, a two stage pumping system is employed with precompression provided by a 108 cfm Roots blower.

The fraction of discharge energy which reaches the chamber wall has been measured at approximately 40%. The distribution of energy on the chamber walls is not known in detail. However, intelligent guesses could be made based on the physics of the DPF process. Previous measurements made at SRL have shown that most of the gas accelerated in the rundown phase continues along the axis until it hits and the wall. This gas, with kinetic energy of order 200 eV per particle, shocks against the end wall. The dominant mechanism for heat loss by this shocked gas is through radiation. The end wall can be expected to intercept up to 50% of this radiation. The pinch likewise radiates strongly. From straightforward geometric considerations, a certain fraction of this radiation is intercepted by the electrodes, and the remainder transferred to the walls.

The chamber is not cooled directly. Rather, it has a water cooled liner. The liner is made to be readily removable so that it may be serviced, and so that diagnostic ports in the chamber wall may have direct view of the plasma during low repetition rate experiments. At the end of the chamber opposite from the DPF electrodes, a cooled molybdenum beam stop is provided for the plasma which is axially accelerated to approximately 200 eV during the pre-pinch phase of the discharge. This beam stop is conical in shape, with the apex pointing back towards the pinch. Consequently, the shocked, stagnated plasma will experience a radially outward component of velocity, as well as a reversed axial component, as it begins to expand. A water cooled copper dome extends from the edge of the conical beam stop to the water cooled cylindrical wall liner. A photograph of this arrangement is presented in Figure 21. These two elements, along with the beam stop, must dissipate much of the radiative energy given off by the axially directed plasma shocking against the beam stop, and by the radially

directed pinch plasma. The beam stop, the dome, and the side wall liner all have separated water feeds. By monitoring the water temperature jumps in these feeds, the spatial distribution of the heat loads will be determined. This will allow for optimization of cooling in the deliverable device.

The shapes of the beam stop, the adjacent domes and the wall liner are such as to encourage a toroidal flow of gas within the chamber during repetitive operation. That is, the gas that is accelerated along the axis will hit the beam stop and reverse its flow so as to return along the cylindrical walls.

Upon nearing the plane of the cathode base, the flow will turn radially inward, pass between the cathode bars, and fill the vacuum left by the snowplow phase of the previous pulse. Before passing through the cathode bars, the gas must pass between a set of cooled, radially orientated fins which are attached to the cathode base. Their primary function is to conductively cool the gas. However, when a second set of uncooled fins is interdigitated with the cooled fins. The combination forms a thermophoretic nanoparticle precipitator. Nano-particles will be driven to and adhere in the form of a film to the cooled fins.

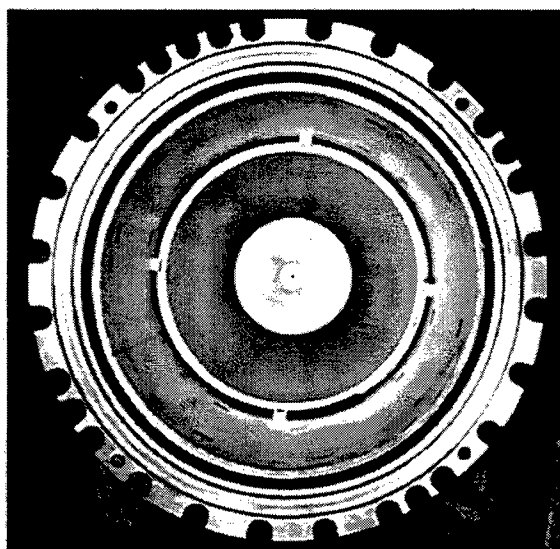


Figure 21: View of Interior of Vacuum Chamber, as Seen From the Pinch, Showing Cooled Cylindrical Liner, Dome, and Conical Beamstop

Thermophoretic Particle Precipitator:

It is well known that discharges produce nano-particles. Concern has been expressed that, during long runs, the density of these particles could build up to the point where they interfere with the propagation of the X-Rays, or that they would settle on the X-Ray window or the insulator between the electrodes. The newly introduced procedure of reverse flow of neon through the anode should greatly ameliorate these issues. However, the ideal situation would be a continuous cleansing of the gas within the chamber. Ordinary filters are out of the question for such small particles, and electrostatic precipitators could not be expected to function in the pulsed plasma

environment. A thermophoretic precipitator, on the other hand, appears to be ideally suited. In fact such devices are employed in the manufacture of nano-particles. If a thermal gradient exists in a gas containing particles, the particles are exposed to more gas molecule impacts from the hot side than from the cold side. Consequently, they acquire a drift velocity in a direction opposite to the temperature gradient. This is the physical basis of the so called thermophoretic force. If the particle diameter is small compared to the mean free path for collisions, the drift velocity is independent of particle diameter. This is case within the chamber where, at 1.3 torr working pressure, the mean free path in Ne is of order 60 microns. The drift velocities are substantial. A temperature gradient of 100 K/cm results in a drift velocity of 50 cm/s, which is approximately 1/5 of the characteristic circulation velocity. Experiments have shown that that the nano-particles will, when driven by a temperature gradient, plate out in the form of a loosely adhered film on the first surface it encounters while drifting.

As mentioned above, a gradient will be established between a set of cooled fins and an interdigitated set of hot fins. The hot fins are attached to a common thermally conductive ring which is designed to intercept thermal radiation from the shocked plasma and, coincidentally, shield the cooled fins from this radiation. No additional power is necessary to maintain the thermal gradient. The characteristic circulation velocity increases in proportion to the pulse repetition rate as does the intercepted radiation power. Consequently the ratio of drift velocity to circulation velocity and collection efficiency should be independent of repetition rate.

DPF Source Computer Controls and Hardware Interrupts:

The computer control system is PC based, currently running under Windows 95. LabView, from National instruments is used for the control software. This is a graphical programming system which has the advantage of being almost as fast as C, yet development time is a small fraction of that with C. An entirely new program, with state machine architecture, was developed during this contract.

Almost all systems, excluding the hardware interrupts to be discussed below, can be controlled through computer. The only major exception, at this point in time, is the vacuum system. During Phase 2 of this program, control of the vacuum system will be added, and the software will be modified so that all source functions, with the exception of maintenance, may be controlled through a remote TCP/IP interface.

The computer system monitors and stores measurements of the system performance, including X-Ray output, plasma rundown voltage, chamber pressure, pressure, temperature, and flow rates for all key components, including the electrodes, insulator, beam stop and vacuum chamber. Virtually all of the system measurements can be displayed in strip chart format. With only two 20 inch monitors, they cannot all be displayed simultaneously. However, a mouse click will switch from one set to another. The new all-solid-state source has been fitted with a comprehensive hardware interrupt system. There are over two dozen different flow, pressure, temperature sensed conditions which will result in a system interrupt. All of these, with the exception of out of limits temperature readings, are handled completely in hardware, independent of the computer. The status of the interrupts is displayed on an annunciator panel. The status is also forwarded to the computer where a virtual annunciator panel can be displayed. The control software is programmed to send the interrupt hardware a

"heartbeat" signal at a higher rate than the fastest pulse repetition rate, (100 Hz now and 130 Hz in the deliverable machine). Should this signal fail to arrive, the hardware will assume the program has hung or the computer has crashed, and all firing will be terminated. A number of the interrupt sensors are out of limits during system start up. Time delay relays insure that interrupt condition are not signaled during the appropriate startup time for each such sensor. For a development platform, it is sometimes necessary to bypass an interrupt for diagnostic purposes. Rather than "hot wiring" such bypasses, the system provides bypass switches. Annunciator lights warn that a given interrupt is bypassed, and the computer is "informed" that at least one bypass is in place.

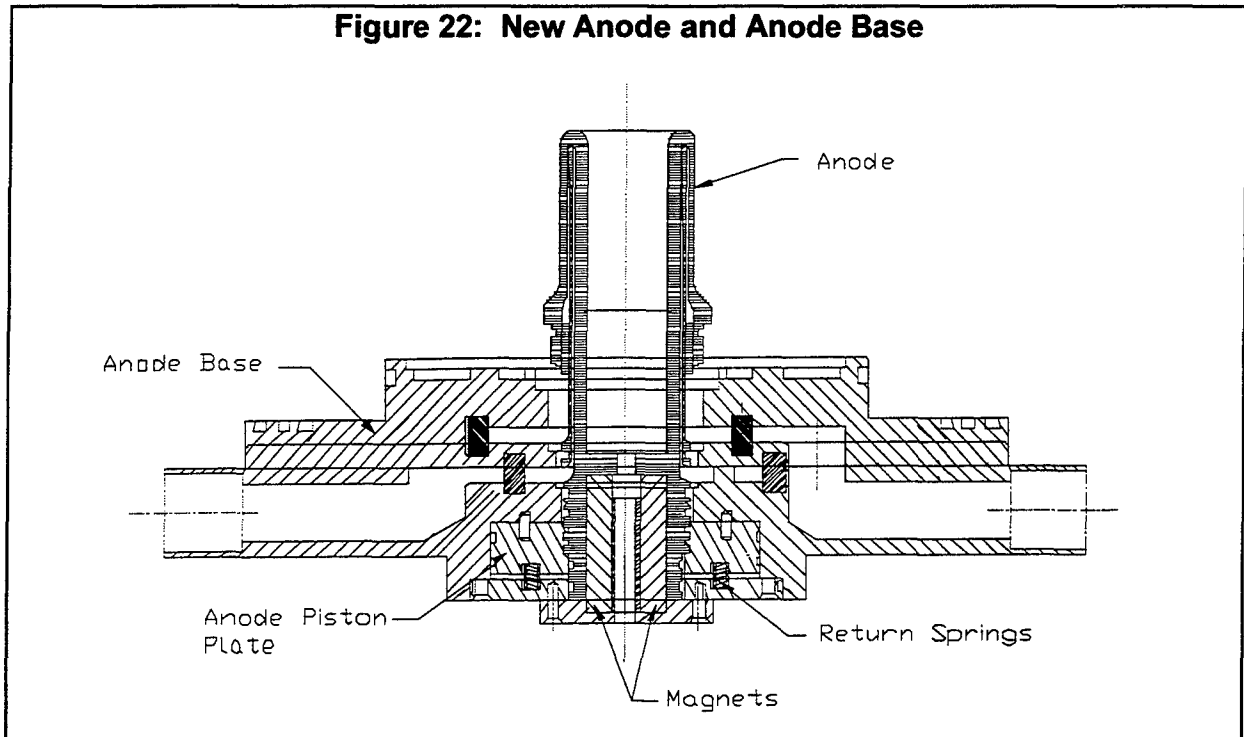
New Anode Base:

The anode base for the new all-solid-state driven machine incorporates an number of changes from the spark gap driven machine. One obvious change was the necessity of a larger bore in order to accept a straight through anode. Other changes were dictated by the high average power of the new system and by experience with the old system. The new anode base was built of copper versus stainless steel in order to limit skin effect heating as the current converges on the center electrode. The knife edge is stainless steel so as to allow penetration of the softer metal gasket between the anode base and the anode. This knife edge is brazed so as to be in good thermal contact with the cooled copper base, and it is bathed on both side by coolant water. The system was built so that the knife edge could be replaced should it be damaged. The new anode base makes a current connection with its feed plate over a significantly larger diameter, thereby limiting peak currents to 10 kA/in, and avoiding EDM action, (Electrode Discharge Machining), at the contact line.

A technical issue was raised as to whether the current connection between the center electrode and its base could sustain continuous operation. At the time of this test, the baseline architecture for the new machine included 24 modules firing at a 50 Hz rate. A DVT was initiated in which a knife edge connections were made to a fraction of the circumference of a circular copper gasket. That fraction was chosen such that the RMS line current density resulting from application of current pulses from a single module would be the same as the 130 rms amp/cm current which the normal connection would receive from the full compliment of 24 modules. The test connection was placed in series with the dummy load being used with the 10^8 shot module tests. The connection survived 12 million shots with no sign of deterioration. Since about half of the shots were at a 100 pps rate as opposed to the 50 pps rate, the connection was actual subjected to extended testing at a level 50% greater than nominal. (Note that rms current scales as the peak current times the square root of the product of the frequency times the pulse width).

The previous anode base used a system of four cams to engage holes in the base of the anode in order to pull its knife edge into electrical contact with the copper gasket.

Figure 22: New Anode and Anode Base



This system suffered from high friction and material distortion at the cam interface. Moreover, it was non compliant. If the gasket material underwent creep, good current contact would be lost. This in turn would lead to EDM of the knife edges, which would result in damage to both the anode base and to anode. A compliant friction free long term solution was conceived, and it has been incorporated in the new machine. The anode will, with a 1/8 turn motion, lock into a piston which is buried in the anode base. Application of air pressure to one side of this piston pulls the knife edge on the anode and the knife edge on the anode base into the metal gasket current connection separating the two. The new system allows for rapid change of the anode, is simpler to build than the previous system, and it should be more reliable. The new anode and base are illustrated in Figure 22. Also illustrated in this picture are the magnets whose function is to deflect the induced electron beam so that it does not strike the X-Ray output window.

The pneumatic lockdown system for the anode was first exercised using a annealed copper gasket. A pressure of 290 psi N_2 on the piston, (1630 lb. force), resulted in a very uniform signature of the knife edges in the gasket. However, the total penetration, both sides, was only six mils. Substitution of an annealed gasket of 1100 aluminum resulted in the objective penetration of 13.6 mil. Observation of this gasket after 20,000 shots shows absolutely no sign of deterioration.

Electrodes:

New anodes of stainless steel and of molybdenum were built for the new anode base. They are of the straight through type with skirt. A magnet holder is provided in the base of the anodes near the beam aperture. As described above, the base of the anode has a bayonet type configuration which locks it to the pull down piston plate. A new long rod water cooled cathode was built for this machine. The cathode makes electrical contact with the feed plate over a large diameter so that a finger stock type of contact can be employed. The cathode base is a water cooled disk of copper. Copper gas cooling fins extend from this disk. External water plenums connect to the cathode through an array of hoses terminated with quick disconnect fittings. An array of pneumatic clamps hold the cathode in place against the feedplate insulation. A vacuum seal at that interface is effected with O-rings. The combination of the method of electrical contact, the quick disconnect water feeds, and the pneumatic clamping system allow for tool free replacement of a cathode in a matter of minutes. A

photograph of the new electrode set is provided in Figure 23.

Chiller:

The chiller system employs city water for primary cooling at 30 gal/min. The primary system is provided with an inlet filter, a boost pump at the inlet, an accumulation tank, and a boost pump on the outlet to city drains. At Sanders a similar system will be employed, but the city water will be replaced by "in house" chilled water.

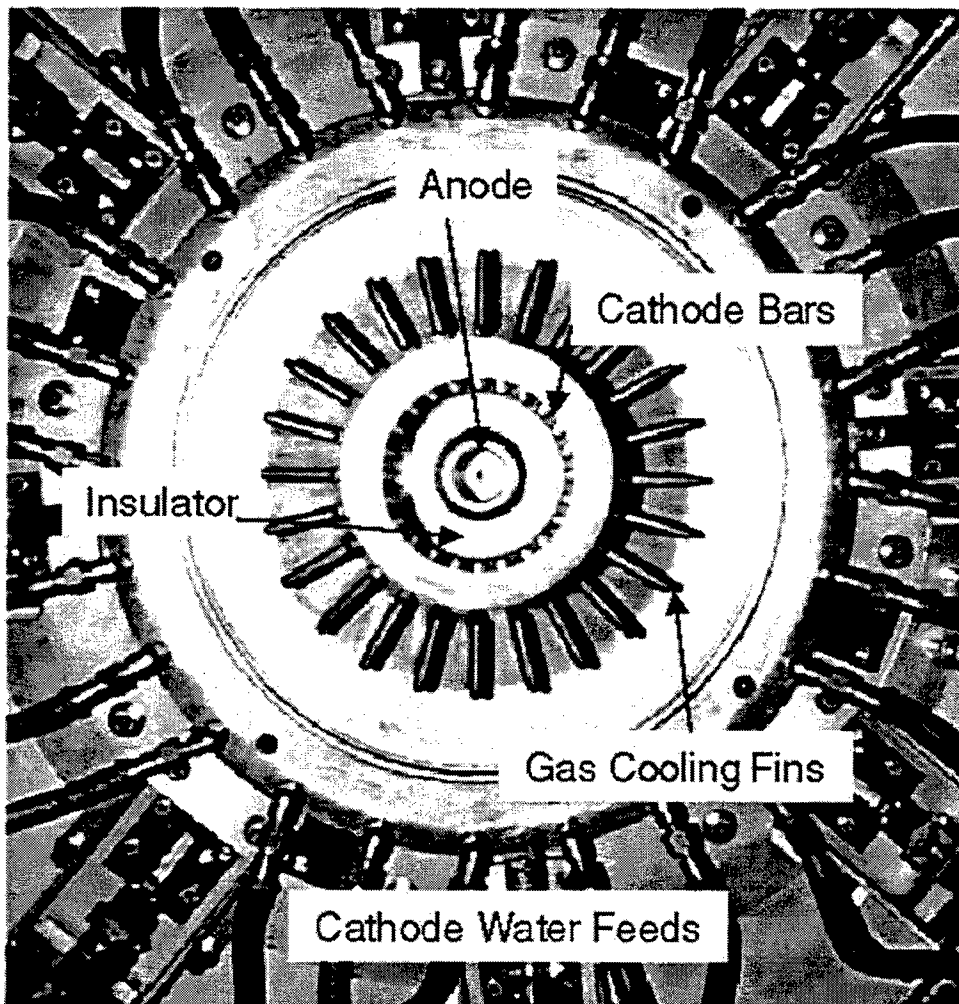


Figure 23: New Electrode Set

There are separate heat exchangers for the chill water, the normal water circuit and for the deionized circuit. Each of these circuits has its own 1 hp pump circulating water

through its respective heat exchangers to its respective degassing tower and back. The 16 ft degassing towers each have a 100 gal capacity, allowing them to also serve as reservoirs for the water circulated to the various parts of the X-Ray source. The height is short enough to fit within the chase area at Sanders without having to penetrate the roof. A portion of the circulating deionized water passes through a deionizer.

A 16 gal/min, 300 psi, constant volume pump with a 5 hp motor supplies deionized water to the anode. A 40 gal/min, 100 psi, constant volume pump, also with a 5 hp motor, supplies water to the cathode and the beam stop. Solid state controllers allow the pumping speeds of these motors to be controlled. Deionized water is supplied to the insulator, the high voltage plate, and to the modules through via a 1 hp pump. A second 1 hp pump provides coolant to the radiation shields inside the vacuum chamber, and to the two ground plates of the triplate. All pump functions can be manually controlled, or controlled from the computer via solid state relays.

The pumps, heat exchangers, and control panels are fitted within a wheeled "cooling cart". It is anticipated that a similar arrangement will be employed at Sanders, thereby allowing rapid setup and efficient use of space. The cooling cart could be located near the degassing towers in the chase so as to avoid having rotating machinery in the clean room.

DPF Source Serviceability:

The ease of servicing of this machine is a major advancement over previous models. The discussions above described the simple processes of replacing a module, an anode, or a cathode. All of those processes can be completed in minutes without the use of tools. The photographs, Figure 24, Figure 25, and Figure 26 give a graphic illustration of the simplicity of the process of accessing the head for servicing. Figure 24 shows the operator's view of the head which covers the chamber. Removal of the chamber involves opening a valve to bring it up to atmospheric pressure, turning a valve that releases the pneumatic clamps that maintain pressure on the chamber O-ring seal, and pulling back the cart on which the chamber is mounted.

Figure 25 illustrates the process of pulling back the vacuum cart. Note that the Roots blower mounted and vibrationally isolated on the lower cart shelf moves back at the same time, so mid and high vacuum connections do not have to be broken. The forevac connection simply slides out as the cart is withdrawn. Note also the large hoses at the side of the cart. These provide cooling to the vacuum chamber. They do not have to be disconnected to allow withdrawal of the cart.

Figure 26 shows the operators view of the head with the chamber withdrawn. If the anode is to be replaced, the operator simply throws a valve to release pressure on the anode piston, reaches in, twists the anode by 1/8 turn, and pulls it out along with the current connection gasket. A new or refurbished anode is put in place by reversing these operations. In order to remove the cathode, the quick disconnect fittings at the cathode cooling plenums are pulled off, and a valve is turned to release the cathode clamps that are shown in Figure 26.

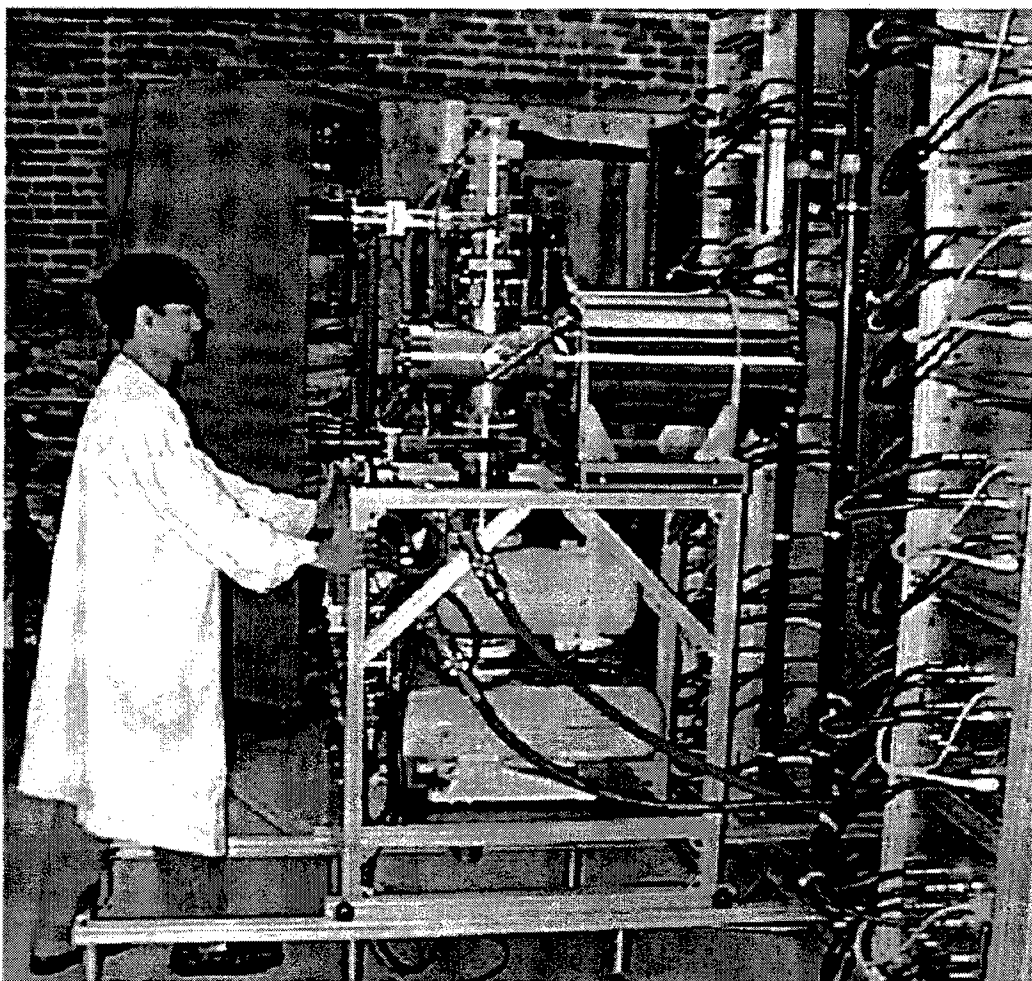


Figure 24: Withdrawal of the Vacuum Chamber

The cathode simply pulls out. If the insulator is to be removed, both the cathode and anode must be removed. Bringing the system back on line involves a reversal of the processes outlined above, with the exception that pulling a vacuum replaces the operation of letting the system up to air. The pumpdown to base pressures a factor of a thousand below operating pressure takes only minutes.

The ease of access built into the device extends beyond items requiring regular service. All of the device, with the exception of the cooling cart, has been built with serviceability in mind. The one omission will be corrected in the deliverable model. The payoff in this approach has been immediate, with a marked improvement in productivity in experiments to characterize the device. In summary, this laboratory prototype has been built to serviceability standards which will carry over directly to an industrial setting in the semiconductor industry.

Install and Test DPF Driver:

Early System Demonstration:

Near the beginning of this program, at the request of DARPA and Sanders, SRL hosted a series of measurements intended to benchmark the upgraded spark gap driven DPF

X-Ray source in Somerville, MA against performance previously documented in Alameda, CA. Juan Maldonado, DARPA's representative, made measurements of the X-Ray output and effective wavelength of the DPF device.

For these tests, a cooled stainless steel anode with a clear bore, (no aperture to impede the plasma zipper phase), and a newly developed tall cathode were installed. Strong, reliable pinching was observed, with a pinch drop out rate of only about 2%. Pinches occurred after the normal delay of about 1.6 msec after the start of the discharge. The average X-Ray output was 19 joules as measured by the PIN diode

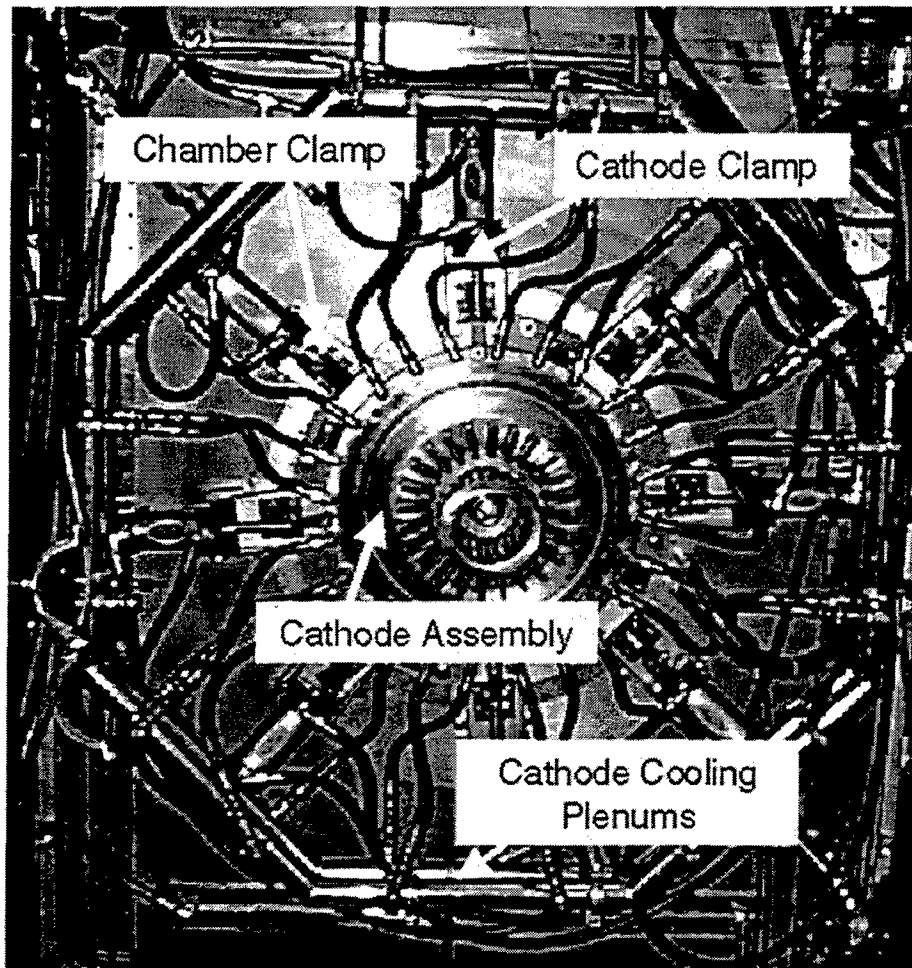


Figure 25: View With Head Exposed Showing Pneumatic Clamping System

monitor mounted in the differentially pumped beam line. In order to accommodate these tests, a differentially pumped beam line, which differed from the beam line built for the chopper, was constructed. Differential pumping yielded pressures in the beam line below 0.2 torr, and a computed average transmission through neon of 80% (versus 40% without differential pumping). The tests were operated in the same configuration as tests previously performed at Alameda. That is, Maldonado's apparatus was mounted at the end of an arm on top of

the vacuum chamber at an angle of 14 degrees off the machine axis. However, in contrast to the Alameda test series, the chamber pressure was 1.7 torr versus 1.0 torr. Maldonado reported an output, (into 4π sr), of 15.8 joules per shot and an effective wavelength of 11.4 Ang.

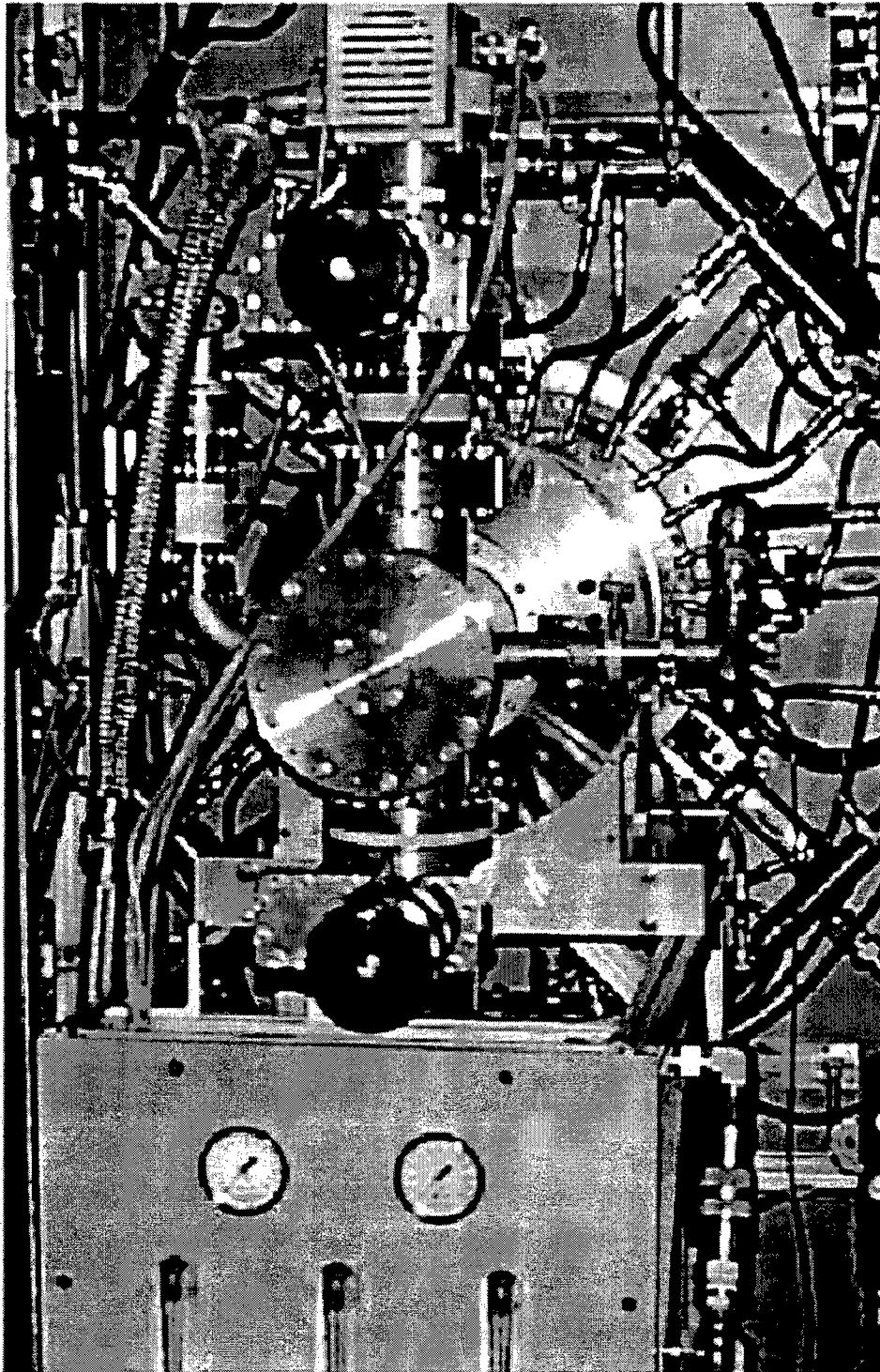


Figure 26: View of Vacuum Chamber Covering DPF Head

One Hundred Million Shot Module Test:
As part of the solid-state development effort, a 100 million shot lifetime test was performed on the DPF solid-state drive module. The purpose of the test was twofold. The module was operated at rated power for a sufficiently long time to 1) identify and correct any weaknesses in design and component selection, and 2) to acquire data which would permit a prediction of ultimate lifetime. Highlights of the test series are presented below in Table 8.

The module was operated to 100 millions shots over a 3 month test period from April to June 1997. Most of the problems

encountered during the life test were of the nagging type prevalent in prototype laboratory devices. For example, problems with computer controls indicating a bias power supply fault were eventually traced to a faulty 5 V supply in the controls assembly. During the life test there were two incidents that led to power semiconductor

failure. The first occurred at 39 million shots, and was caused by operator error. In order to isolate the control bias fault signal, the optical fibers that conveyed trigger power fault to the control network were disconnected. The power connection to the trigger card for thyristor #2 was inadvertently broken, causing this card not to trigger. As a result, 10 kV was impressed across thyristor #2, (see Fig. 13), causing it to breakdown and short. This then put 5 kV across the remaining thyristors. Thyristor #3 failed in a similar manner as thyristor #2. The remaining thyristor #1 was saved because its RC snubber network arced over and shorted.

Table 8: Summary of 100,000,000 Shot Tests

- The module was effectively operated for more than 140 million shots:
 - * 10 million shots were conducted in 1996 test sequence.
 - * 100 million shots were added from March to June 1997.
 - * An additional 30 million shots were added in September 1997.
- The module demonstrated an average power capability that is two times greater than the baseline X-Ray system design.
 - * 100 Hz operation was demonstrated compared to the baseline 50 Hz design point.
 - * The module was tested at charge voltages up to 10 kV, which was 25% over its 8 kV design rating.
- Life testing identified some module component and design deficiencies and their resolution:
 - * Sub-standard components and electrical insulation assemblies were identified and replaced.
 - * Voltage surge protectors and fast over voltage sensors were implemented.
- The initial 100 million shot module testing identified power semiconductor life issues:
 - * Asymmetric current distribution due to non-uniform clamping pressure caused cathode contact degradation.
- A follow-on 30 million shot test sequence showed improvements in power thyristor clamping techniques eliminated contact electro-migration, so that device lifetime is ultimately limited by thermal cycling issues.
 - * Temperature excursions in the thyristor wafer are low enough to project to greater than 10 billion shot lifetime.

The second power semiconductor failure occurred at 81 million shots. An external arc and breakdown in the high voltage insulation caused an over voltage condition across SCR #1 and diodes #1 in the diode snubber stacks. It should be noted that the external arc occurred at 10 kV operation, which is 25% over the 8 kV design rating for the prototype module. The insulation design has been improved in the upgrade module in order to eliminate this failure mechanism.

We have subsequently implemented silicon surge protectors to guard against over voltage conditions across the thyristors. These surge protectors act as fast voltage break-over devices similar to zener diodes, and fail closed if they dissipate too much

energy. (This is opposed to varistors that typically fail open). We have also incorporated a fast over voltage sensor across each SCR that will shut the system down automatically. Thus, if an over voltage fault occurs, or a surge suppresser is lost, the over voltage sensor will stop the system and alert the operator of the SCR stack status. The module design improvements that resulted from the 100 million shot life test included:

- Increasing electrical insulation by 4X to eliminate external arcs.
- Implementing improved over voltage sensors that shut down operation if an over voltage situation occurs
- Implementing fast silicon surge protectors to protect thyristors from over voltage.

Power Semiconductor Life Analysis:

The thyristors that were destroyed were sent back to ABB for analysis. Some electro-migration in the cathode metalization contact was found, which was caused by inadequate pressure contacts in the hockey puck devices. Analysis showed that electro-migration correlated to regions of the SCR pole face that were not directly underneath a clamping bar. Pressure paper measurements showed that these areas were under significantly less compressive force, i.e. the area directly underneath the clamp showed much higher force than at the edges beyond the bar. A new clamping bar that covered the entire SCR pole face was tested with pressure paper, and showed that compressive force was now uniform across the SCR.

In order to verify that inadequate clamping was the cause of the electro-migration, the module was operated for an additional 30 million shots in September, 1997. Thyristors used in this test were then returned to ABB for analysis. ABB found the thyristors to be in pristine condition with no evidence of contact electro-migration. This confirmed the that earlier issue of contact electro-migration was caused by inadequate clamping procedures. Consequently, the long-term life limiting mechanism in the module thyristor is failure due to thermal cycling. ABB has a wealth of engineering data on semiconductor lifetime as a function of silicon wafer temperature rise over a discharge cycle. SRL provided ABB with detailed commutation voltage and current traces in order for ABB to calculate the thermal temperature cycling in the wafer. The semiconductor reliability group at ABB has estimated that the wafer temperature cycle excursion is less than 2 degrees C, which interpolates to greater than 10 billion shot life expectancy for the thyristor.

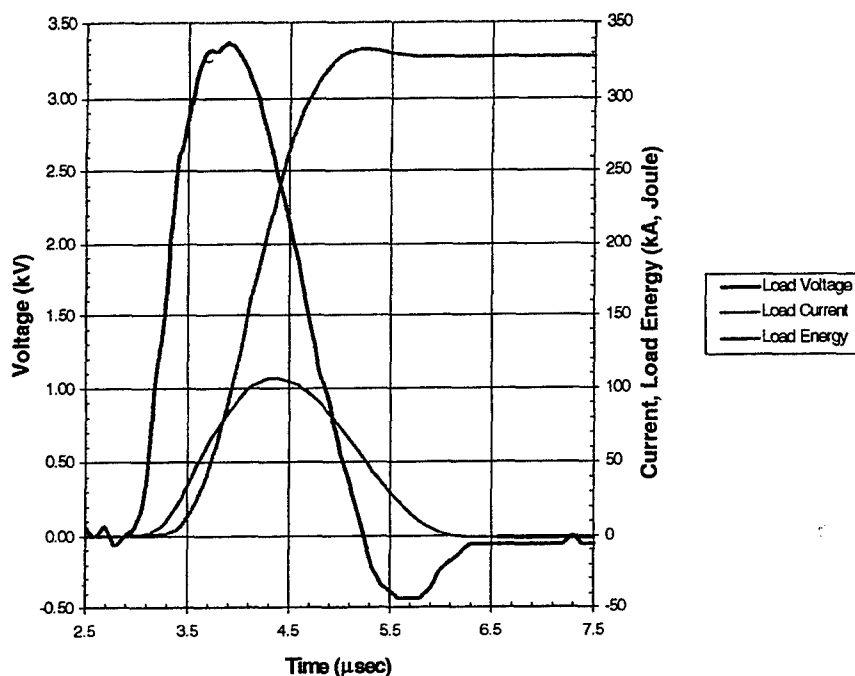
Module Life Test Summary:

A prototype solid-state module was operated for 100 million shots in order to identify component and design deficiencies. During operation, the module was operated at voltage levels 25% greater than its baseline rating, and at average power levels that were twice its design point. The life test identified component and electrical insulation inadequacies, as well as issues on how to proper clamp the power thyristors to avoid high current densities and cathode contact degradation. Engineering modifications were implemented that eliminated these problems. Life analysis indicates that with improved clamping techniques power semiconductor lifetime will scale to greater than 10 billion shots.

Bringing System on Line into Dummy Load:

The solid-state modules were tested into resistive loads in order to verify switching performance. Initially, 6 parallel modules were operated into a 0.025W load. Figure 27 shows the discharge waveform into the resistive load at 7 kV charge voltage. The measured output current for 6 parallel modules was 106 kA at a current rise time of 700 nsec, (10% to 90%). The overall energy transfer efficiency from modules to the load was 88%. The 6 module array was also operated at 100 Hz pulse recurrent frequency for short bursts into the resistive load. Figure 27 shows there is no current reversal in the load, which verifies the snubber circuit operation. The measured electrical performance of the modules operating into the 0.025W resistive load met all design goals.

Figure 27: Voltage and Current Waveform for 6 Parallel Modules Driving a 0.025W Resistive Load at an Initial Charge Voltage of 7 kV.



The full complement of 12 parallel modules was then operated into a 0.0075W load. Figure 28 shows the output voltage and current traces for the 12 modules charged to 7 kV. The measured peak current was 210 kA with a current rise time of 850 nsec (10% to 90%). Note that the current waveform is smooth, indicating that all 12 modules are triggering simultaneously. The measured energy transfer efficiency to the load was 70%. The longer current rise and lower energy transfer efficiency for the 12 module test is due to the lower resistance and impedance mismatch of the load. Again note that there is no current reversal in the under-damped load.

The thermal and power interfaces were completed. This allowed for integration of the head and driver, the first steps of which included installation of the anode base along with its cooling, vacuum, and pneumatic lines. The electrodes, including a cathode, a

stainless steel anode, and a molybdenum anode, were completed. Both the cathode and an anode were fitted up into the head.

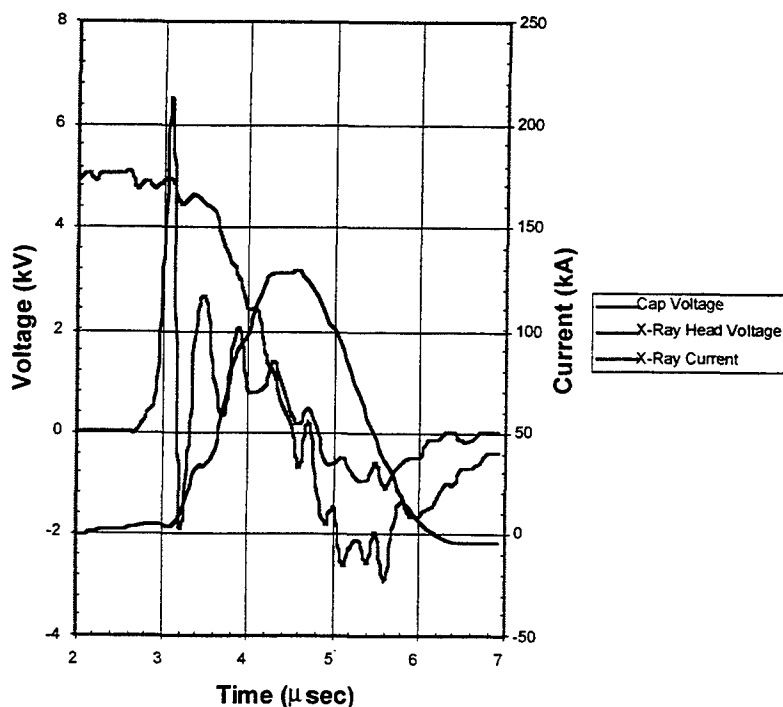
The pneumatic lockdown system for the anode was exercised using a annealed copper gasket. A pressure of 290 psi N₂ on the piston, (1630 lb. force), resulted in a very uniform signature of the knife edges in the gasket. However, the total penetration, both sides, was only six mils. Substitution of an annealed gasket of 1100 aluminum resulted the desired penetration of 13.6 mil.

The cathode was fitted into place. The dimensions were in accord with specifications. A softer rubber O-ring (25 lb. compression force per inch of O-ring length versus 70 lb. per inch for the usual Viton rings) was installed so that the cathode can be held in place with less pressure from its pneumatic holddown clamps. The pneumatic drive system for these clamps was installed and checked out.

Bring System on Line into DPF Load:

The 12 module system was briefly operated into a DPF X-Ray head. The solid-state driver was able to generate discharges across the DPF electrodes at charge voltages as low as 5 kV at 1.3 torr neon fill pressure. Figure 28 shows the discharge waveforms at 5 kV charge and 1.3 torr neon pressure. Peak currents are on the order 130kA with

Figure 28: X-Ray Source Waveforms Generated by the 12 Module Solid State Driver. The pulser was charged to 5 kV, and the X-Ray head was pressurized to 1.3 torr neon.

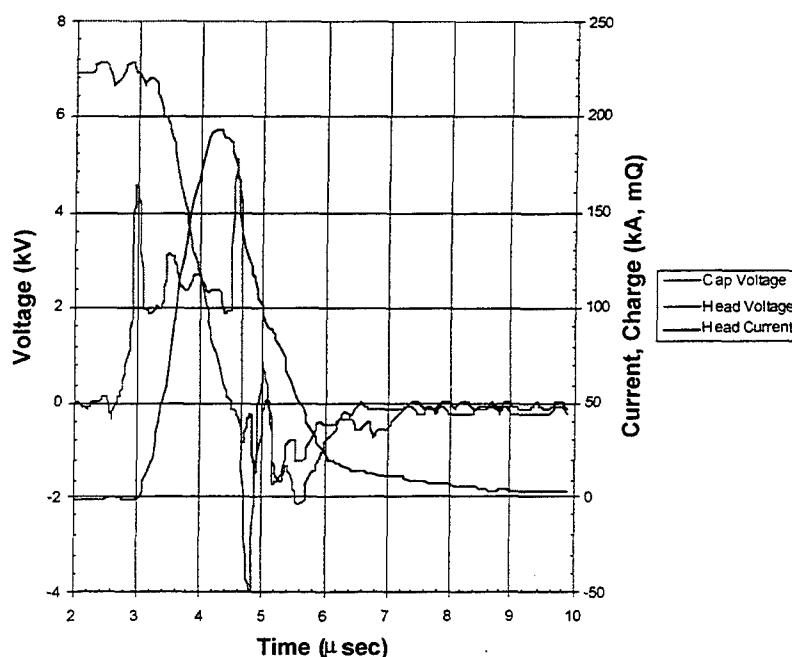


no current reversal in the head. Initial tests at 7 kV show discharge currents of 220 kA, which is the design point for the solid-state driver system.

Once the insulator is conditioned, after firing a few thousand shots, plasma pinches developed. The presence of a pinch is immediately evident from the appearance of a second spike in the voltage trace and a sharp drop in the current. These features are visible in Figure 29, which was taken under conditions of 1.0 Torr fill of neon gas and a charge voltage of 7 kV.

Following the achievement of pinches, a beamline was installed on the machine. This is illustrated Figure 30. An aluminum foil separates the vacuum of the beamline from the chamber pressure. A PIN diode senses the X-Ray fluence. The current signal from the PIN diode is now monitored on a high speed oscilloscope. In the near future, a system of analog integration followed by digitization of the net charge, the same as was employed on the spark gap driven system, will be implemented. This will permit characterization of every pulse and accurate dose control. The amount of X-Rays produced appears to be comparable to those produced on the spark gap driven system under the same conditions. Detailed cross checking of X-Ray diagnostics is underway. The system has now been operated at 20 Hz in bursts of 200 pulses per burst with neon flow introduced through the anode. X-Rays have been achieved over twenty

Figure 29: Waveforms with Pinch. 7 kV charge, 1.0 Torr Ne



bursts with *no dropouts*.

To date, the electrodes have been subjected to 40,000 shots. Examination of the anode shows an amount of erosion that is too small to measure with any accuracy. This was expected. A major function of the all-solid-state driver was to eliminate the current reversal that was implicated in anode erosion. The waveforms show that current reversal is indeed eliminated. The inspection shows that material removal from

the anode is at least tens of times smaller than observed with the spark gap driver. This is highly encouraging. Detailed measurement will have to await the buildup of at

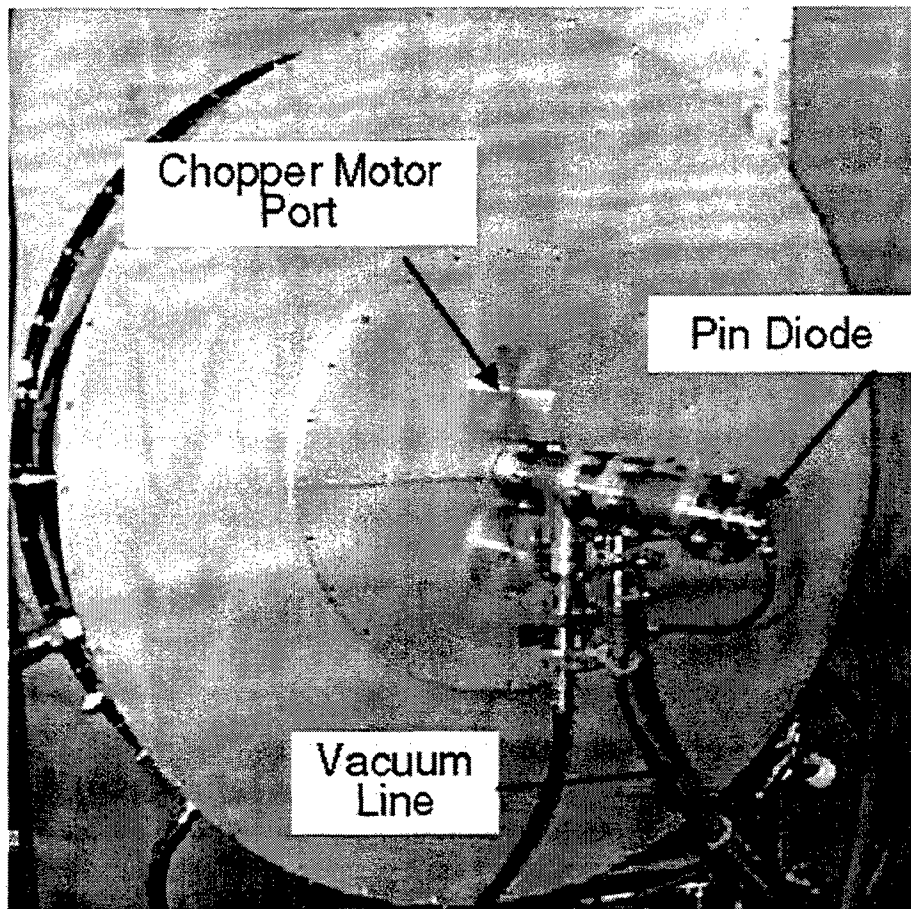


Figure 30: View of Beamline

least several hundred thousand shots on the machine.

DPF Source Characterization by CXrL:

SRL hosted a test series using the original spark gap switched DPF source designed to measure the intensity distribution versus angle of the X-Ray beam. These measurements were critical for CXrL's beamline collimator design.

Previous measurements made by NRL while the spark gap system was at SRL's Alemida, CA plant revealed the following:

Transition	Energy, keV	Emitted Wavelength, Å	Relative Power
H α	1.0215	12.10964	
	1.022	12.10372	
He α	0.9149	13.5206	
	0.9221	13.41503	
Total of characteristic spectrum			60%
Continuum	1.1 - 1.4	8.5-10.7	40%

CXrL used the following information measured by SRL in May, 1997 as a starting point in experiment design:

Average Pulse Energy	$P \sim 19\text{J}$
Conversion Efficiency	$\eta \sim 1.2\%$
Repetition Rate	$\nu = 10\text{Hz}$

By exposing Polaroid film through a stencil mask at two locations, the projection cosines across the exposure was determined. The diagnostic chamber that was used was the housing from an existing gate valve. The overall height of the diagnostics chamber assembly was 10½". The chamber was shipped to SRL and used in experiments on Monday, May 12, 1997. A Polaroid film pack, (600 series), in a 405-type camera back was placed inside of the chamber. Two positions were provided for the stencil mask, "high" and "low".

Calibration of the Polaroid film was performed before and after experiments on the SRL DPF source. The calibration exposures were performed on the ES-1, (hard X-Ray), and ES-5, (soft X-Ray), beamlines at CXrL. For both beamlines, a high degree of reproducibility and accuracy of the film response to the exposure dose for different levels of filtration has been shown. Aluminum filters of 18 μm and 25 μm thickness in different combinations were used. To calibrate the filters, the flux and spectral filtration of the synchrotron radiation, (Aladdin Synchrotron), in the region of 3 to 20 Å was used. The calculated values for Al filters were obtained using PC-Transmit software, (developed by CXrL). Photocells, (2 x 4 cm), and Polaroid instant film were used as the detector.

The experiments with the photocell and with Polaroid film were conducted on the ES1 beamline which provides X-Rays in the spectral region of 3 to 15 Å. With the photocell detector, a set of 25, 50, 75 and 100 μm thick Al filters were used covering 10^{+4} times flux attenuation. With the Polaroid instant film 200, 225, and 250 μm thick aluminum filters were used. In the measurements, the experimental results agree with the calculations within 5% for the photocell detector, (see Table 9). The conversion efficiency of the photocell was found to be equivalent to ~ 4.5 eV/electron.

Table 9: Photocell Response and Al Film Transmission (Measured and calculated values of attenuation are within ~3%).

Thickness		No filter	25 μ m	26 μ m	52 μ m	78 μ m	104 μ m
Power @ 100 mA / 4 mrad	Calculated	115 mW	1.85mW	1.66 mW	147 μ W	30.4 μ W	11 μ W
Photocell Response	Measured	24.6 mA	390 μ A	320 μ A	32.7 μ A	7.1 μ A	2.34 μ A
Transmission	Calculated	1.56E-2	1.4E-2	1.24E-3	2.56E-4	9.1E-05	
	Measured	1.6E-2	1.35E-2	1.3E-3	2.9E-4	9.5E-05	

Table 10: Summary of Exposures Conducted at SRL by CXrL for Source Characterization

Exposure	Film Type	Filter	Mask Position	# Shots	Comments
1	664, 100 ISO	18 μ m Al	none	75	Overexposed, 5 underlying films also exposed
2	664, 100 ISO	50 μ m Al	low	12	Overexposed, no underlying film exposed
3	664, 100 ISO	68 μ m Al	low	20	Exposure in range
4	664, 100 ISO	68 μ m Al	low	40	Exposure in range
5	665, 80 ISO	68 μ m Al	low	20	Under exposed
6	665, 80 ISO	68 μ m Al	low	45	Exposure in range
7	665, 80 ISO	68 μ m Al	high	48	Exposure in range
8	664, 100 ISO	68 μ m Al	high	25	Exposure in range
9	665, 80 ISO	68 μ m Al	high	60	Exposure in range
10	664, 100 ISO	68 μ m Al	high	40	Exposure in range
11	664, 100 ISO	68 μ m Al	high	30	Exposure in range
Total Shots				315	

Photographs were obtained during Exposure #4 at the DPF source, (see Table 10), with the stencil mask in a "low" position and exposure #10 with the mask in a "high" position. The number of shots was the same for both pictures. The pattern on the second photograph is ~1.2 times magnified compared with that in the first. From the magnification value of 1.2, the distance between source and film was estimated at ~720mm and ~600 mm between source and the stencil mask in the "high" position. The visual analysis of the patterns suggests reasonable (qualitative) uniformity of the angular distribution.

CXrL's ES5 beamline is equipped with two gold-coated mirrors and provides soft X-Rays in the 9 to 15Å region, comparable with the DPF Source spectrum. The experimental results obtained with the Polaroid instant film, when compared with the calculations, indicate the sensitivity in the soft X-Ray, (9 to 15Å), region to be proportional to the nominal ISO speed of the film. For an 3000 ISO film, the sensitivity is ~6-8 nJ/cm² and the dynamic range is from 6 nJ/cm² to 100 nJ/cm².

A calibration was performed using Polaroid film on the ES-5 beamline providing a spectrum with average energy in the region of 1400 to 1600 eV. These exposures were performed on film from the same packs and the same thickness, (68 μ m), Al filter as were used at SRL. However, an additional 25 μ m or 50 μ m Al filter was added to provide similar exposure of the Polaroid film. Six exposures correspond to 100, 250, 125, 62, 40, and 30 mJ/cm² were made.

The photographs of the Polaroid exposures were digitized with an optical scanner. TIF files were generated and the files were analyzed by IDL software. The TIF images were converted to a pseudo-color representation for statistical analysis. The value of the intensity was averaged over the central part of the spots. Statistical analysis of recorded images confirms uniformity of the angular distribution within $\pm 1.5\%$, ($\pm 3\sigma$).

Conclusion of CXrL's Evaluation of DPF Source:

For the purposes of collimator design, CXrL can assume a uniform angular distribution within approximately 50 mrad x 50 mrad.

Beamline and Collimator Development:

CXrL has completed the design for a no-collimator beamline that is shown in Fig.32. CXrL has finalized the collimator and intensity correction mask design. The following is

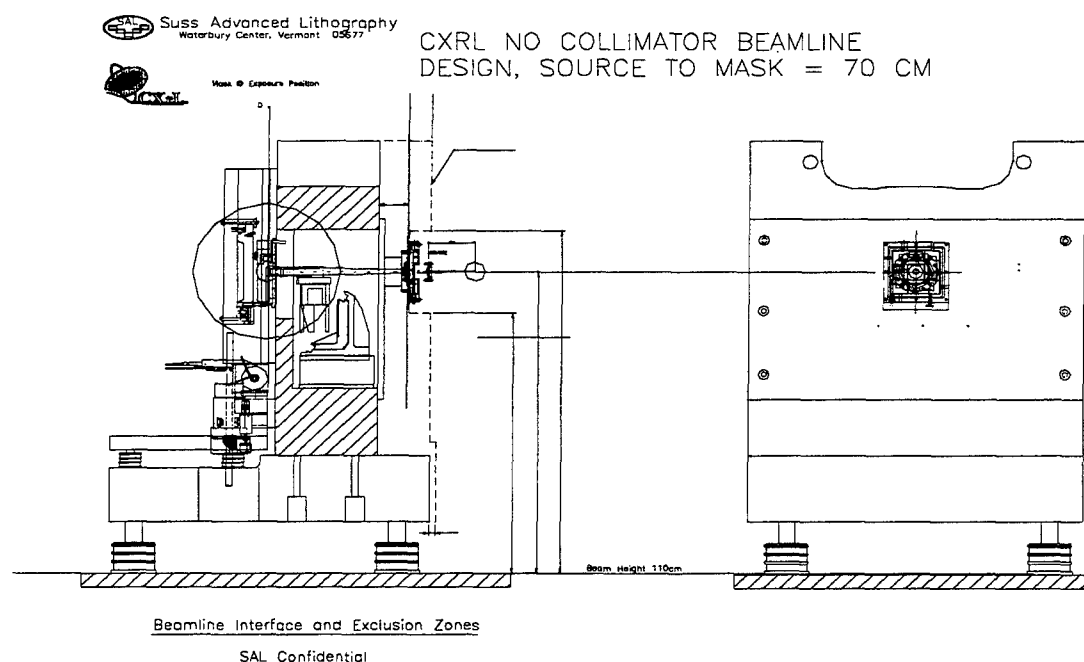


Figure 31: X-Ray Transport Line, (No Collimator)

the status of the point source collimator design.

- The design includes an aspherical collimating mirror that is 3.5 cm wide and 31cm long with a source-pole distance of 50 cm and a pole-image distance of 250 cm. The mirror has an angular acceptance of 70 mrad in vertical and 20 mrad in

horizontal, (scanning,) directions. The angular 'swinging' of the mirror is performed using the position of the point source as a pivoting point.

- The linear shape of the beam footprint formed and the delivered power at the exposure plane are not changing during the scan in the horizontal direction, since the incident angle remains constant.
- Computer modeling was performed for an ideal point source and for the dense plasma focused, (extended: a 10 mm long double cone with 0.5 mm diameter in the center), source with radiation emitted within a 50 mrad cone from each point.
- The collimator provides the following parameters for a 30 mm wide field:
 - ♦ ± 6 mrad angular scanning range and ± 6 mrad global horizontal divergence, (in direction of scan), and ± 0.6 mrad global vertical divergence
 - ♦ Approximately 4 mrad local horizontal divergence, (blur), for the DPF point source and 0.0125 mrad for an ideal point source
 - ♦ 0.9% intensity uniformity range for 10 mm field size and 9% for 24 mm field size were obtained for the DPF source and $\sim 0.15\%$ for an ideal point source

A shorter beamline, (~ 2 m long: 0.5 m from the source to the mirror and 1.5 m from the mirror to the exposure plane), was analyzed in more detail. The shorter beamline does not produce significant collimation gain, but increases the global divergence in the direction of scan from ± 6 to ± 9 mrad due to the larger mirror rocking angle and additional 2 mrad due to lesser vertical focusing.

The design and integration of the beamline with the collimator based on the above-described mirror was finished. The top and side views of this X-Ray beamline hardware are presented in Fig. 33. The X-Ray source is shown on the left of the drawing. The mirror reflects the X-Ray beam and performs the scanning in the horizontal plane. The beamline control software will be based on that designed for the CXrL ES-6 beamline that supports the SAL Model 4 X-Ray stepper.

A preliminary testing of an aluminum prototype mirror, (funded by CXrL internal funds), was performed using visible light. Simulation results confirm the predicted linear shape of the beam footprint.

CXrL has also completed a conceptual design for an intensity correction mask. The intensity correction mask blades, profiled according to the actual intensity distribution of the beam, determined experimentally, are inserted into the beam providing attenuation mostly in the intensity distribution tail region. This way, it offers the possibility of fine-tuning; the level of attenuation will be $\sim 5\%$ of the overall intensity and provide $\pm 0.5\%$ uniformity. The aperture blades of the intensity correction mask can be attached to the scanning window frame or scanned synchronously with the window.

CXrL presently has all of the LabView software building blocks, (vi's), required for controlling their design for the beamline for the no-collimator case. They have software

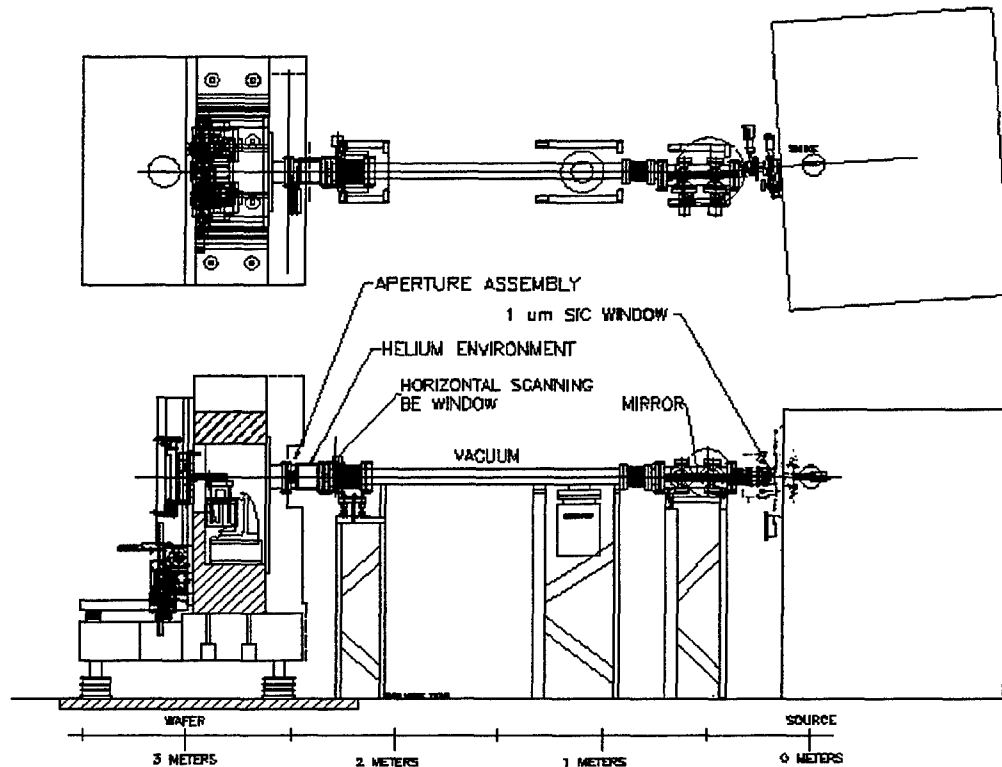


Figure 32: X-Ray Transport Line with the CXrL Collimator

control of the encoder micrometer stages that drive the aperture blades, giving both positioning and position feedback. They also have an A/D card controller that will monitor the 4 solar cells, oxygen sensor, and pressure. This A/D card has output control capability, which will be used to actuate the shutter, and possibly to control helium flow. There is also a software control module that can communicate with the stepper via RS-232.

A012; SOW Task 3.2.4: System Integration

This task includes two parts; first, the system specifications will be reviewed for applicability in MMIC and QWIP device fabrication for military application, (Sanders led task). Second, the system integration specification will be developed, (CXrL led task).

System Specifications Review:

The system specifications review for applicability in MMIC and QWIP device fabrication for military application has been completed. The findings are described in the following.

Lithography is a key technology driver for the silicon semiconductor industry, and the GaAs industry is no exception. While optical lithography is the mainstream technology for production silicon ICs at 250 nm, and even at 180 nm for product development, the

GaAs industry has focused almost exclusively on direct write e-beam for sub 0.5 μm linewidths.

Direct write e-beam is used routinely for production of 0.25 and 0.15 μm GaAs MMICs, and also for development and prototyping of 0.1 μm geometry devices. Such linewidths are used primarily for Field Effect Transistors, (MESFETs, PHEMTs, and InP HEMTs), operating at frequencies from the mid-microwave to high mm-wave spectrum. At the lower microwave frequencies, 1 to 10 GHz, for example, 0.5 and 1.0 μm optically defined linewidths are adequate; in fact, this is the realm in which GaAs is currently produced in high volumes for such applications as PCS and direct broadcast TV. However, as bandwidth needs increase and spectrum becomes available for mm-wave applications such as wireless, LMDS, and auto radar, the need for production quantities of sub-0.5 μm GaAs MMICs will far outstrip the throughput capacity of most foundries using e-Beam tools.

While linewidth and throughput are key, shared issues for both GaAs and Si industries, specifications on other lithography metrics may not be equally important. For example, while GaAs FETs have one critical dimension, (the gate), and one critical registration, (gate to channel), a typical Si CMOS process may have 5 to 6 critical dimensions and registrations, leading to more stringent overlay requirements. Also, since silicon processing usually relies on etching to define critical dimensions while FETs rely on photoresist lifting, the silicon processes require steep resist sidewalls while GaAs device technology relies on sloped walls which are created by manipulating resist chemistry and processing. Thus, divergence is not as restrictive for GaAs FETs as for Si CMOS.

Another issue to consider is chip size and field size. As Si chip size will continue to grow as lithographic dimensions shrink, this will not occur as fast with GaAs. This is because the finer linewidths in GaAs FET devices are usually associated with mm-wave applications, and since circuit size scales inversely with wavelength, the chip size will not grow nearly as fast with shrinking lithography as is predicted for silicon. While one might argue that increased functionality will drive GaAs MMICs larger, it is generally more advantageous to minimize functional integration at the extreme high frequencies and mix down to lower frequencies using less expensive Si or 1.0 μm GaAs technology for signal processing. In fact, according to the SIA Roadmap, chip sizes for the 180 nm silicon generation will be 400 mm^2 , (for DRAMs), to 800 mm^2 (for ASICs), which is a factor of 10 to 20 times the largest GaAs MMIC produced today. Thus, field size requirements should be at least a factor of 2 lower for GaAs than for silicon, notwithstanding throughput issues.

While the above discussion centered on GaAs FET technology for microwave and mm-wave applications, two other GaAs device technologies should be considered: HBT and QWIP. Heterojunction Bipolar Transistors, (HBT), are currently employing 0.5 to 1.0 micron rules, and are thus several generations behind silicon technologies. Current Quantum Well Infrared Photodetector, (QWIP), needs are being met by direct e-beam write, albeit at low throughput (22 hours write time for a 3 inch QWIP wafer using a Leica model EBMF 10.5 e-beam). The throughput goals of the Point Source X-Ray System will have a 300x throughput improvement over current e-Beam lithography. Future QWIP chip size requirements, however, will be pushing beyond even the most

aggressive silicon predictions. Current QWIP chips are about 200 mm² and use sub-half micron lines and spaces. Future projections call for 100 nm lines and spaces, on chips of 1250 to 2500 mm² area, chip sizes which do not appear on the SIA Roadmap until 2012! Clearly, alternative approaches to lithography and processing of such large chips need be considered for QWIP technology, and is beyond the scope of this program.

In view of the somewhat dissimilar requirements between the GaAs and Silicon technologies, a Technical Interchange Meeting was planned to discuss the unique needs of the GaAs industry and solicit inputs for the X-Ray Point Source System Specification. Invitations were mailed to US GaAs Foundries and to over 75 individuals in Government and the GaAs industry.

In conjunction with the TIM planning, a brief survey on Next Generation Lithography Needs for the GaAs Industry was mailed. Questions were asked regarding current and future linewidth requirements, throughput, field size, overlay, divergence, source wavelength, uniformity and intensity, resist chemistry, bake and chill requirements, and preferred wafer handlers. Eleven responses were received: 5 from GaAs foundries with significant, (>10,000 starts per year), volume, 4 from GaAs foundries with moderate volume, 1 from an R&D facility and 1 from a Government laboratory.

Current linewidth requirements, (see Figure 34), varied widely from 150 to 700 nm, probably reflecting a large mix of applications among the respondents. Near term, (through 2003), future needs ranged from 100 to 250 nm, while one foundry predicted 50 nm linewidths in 2005, four years ahead of the SIA Roadmap.

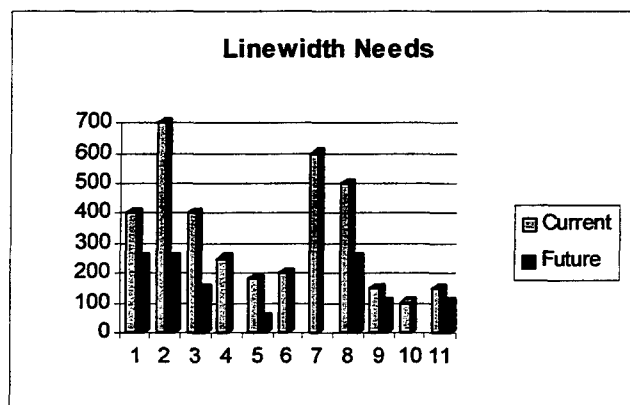


Figure 33: GaAs Industry Linewidth Needs Determined from a Survey

Throughput, (see Figure 35), also varied widely, from 10 to 100 wafers per hour. On the high end, assuming only one level is printed with an X-Ray tool, 100 wafers per hour translates into approximately 200,000 wafer starts per year on a single shift; this is considerably beyond what most foundries are projecting, so it is unclear how this question was interpreted. Perhaps the requested throughput was equated with current optical steppers.

Responses on field size requirements, (see Figure 36), were more consistent, ranging from 15 to 22 mm square. As predicted above, this is well below the requirements of silicon. The smaller field size, coupled with the less stringent requirements for vertical resist sidewalls, will relax the divergence requirement and/or specifications on collimation. In fact, it was notable that only two of the eleven respondents answered the question on global and local divergence limits, and the responses were quite different, 3.5 and 30 mr for global, and 1.5 and 10 mr for local divergence.

Similarly, there were only 4 responses on overlay requirements. Aligner to aligner overlay ranged from 60 to 200 nm, and aligner to self ranged from 40 to 150 nm. The two responses on aligner to absolute grid were 50 and 60 nm. The variations in responses may be due to the differing approaches used to form a "T" gate in FETs, or the variations in linewidth. More study is needed.

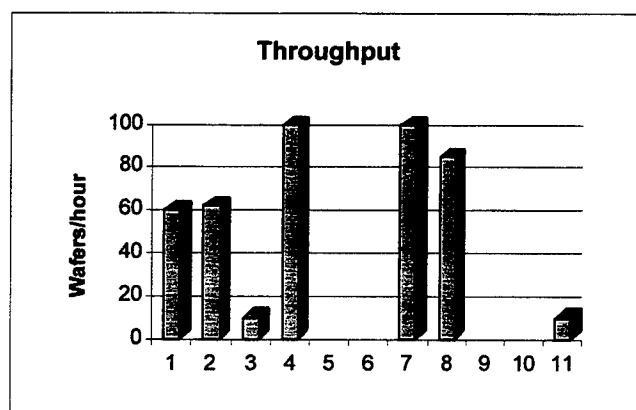


Figure 34: GaAs Industry Throughput Needs Determined from a Survey

Not surprisingly, six responses on wafer size were evenly divided between 100 mm and 150 mm wafers. Eight inch GaAs wafers are clearly not within anyone's horizon yet. Regarding wafer transport, cassette outnumbered SMIF by 6 to 1, with 1 stating no preference. While SMIF may be preferred due to lower potential particulate contamination, which might destroy an X-Ray mask, the industry is tooled for cassette operations and prefers to stay with this technology.

With respect to source wavelength, it is clear that the industry is still thinking "optical." Two respondents mentioned DUV (wavelength unspecified), 1, 365 nm, 2, 248 nm, and 1, X-Ray. Foundries are being very cautious about X-Ray, and will remain so until an affordable point source system has been demonstrated with GaAs technology. Synchrotron rings, while affordable for a \$1B silicon factory, are not practical for a typical \$50M GaAs factory. Resist chemistry and bake/chill requirements were typical of the resists required for the cited wavelengths.

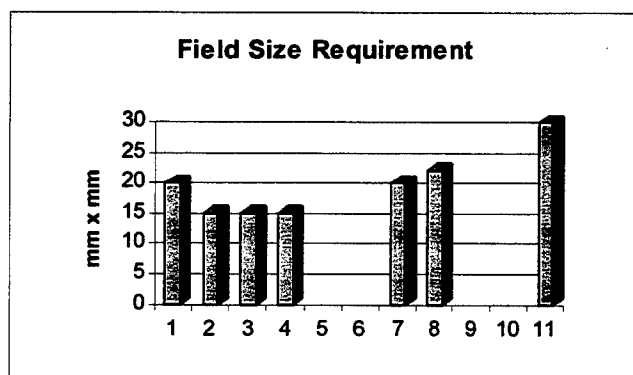


Figure 35: GaAs Industry Field Size Needs Determined from a Survey

In summary, from the survey it is clear that linewidth needs of the GaAs industry will lead projections of the silicon industry for isolated lines by at least several years (when considering year of "first product shipment"). Also, while the throughput requirements are significantly lower than for silicon, (annual wafer starts of a large GaAs factory are about equal to the monthly starts of a typically sized silicon factory), they will be well beyond the capability of conventional e-beam tools. Thus, to meet both linewidth and throughput

requirements, a new lithography tool is needed.

A draft Specification for the Point Source Lithography System for Sub-0.15 μm Design Rules was written based on Table 1 of the SOW and circulated to team sub-contractors for comment. The final version dated May 15 is attached in Appendix A, and

incorporates feedback from team sub-contractors and the Industry survey. The system specifications, as written, are fully compliant with needs for processing GaAs devices in production to current 0.15 μm design rules.

DPF Point Source System Control Interface:

A document was prepared which describes the communication hardware, software, and protocols which will allow the X-Ray source to be controlled by SAL's stepper. The final form of this document was forwarded to SAL for their approval, which was given. What follows is a copy of that document, with the exception of attachments dealing with LabView's TCP/IP capabilities.

At the June 2, 1997 interface meeting between SAL and SRL engineering staffs, mutual agreements were reached which allowed the communications and control interface to be defined broadly. Further issues regarding details of the communication protocols were clarified at a subsequent meeting.

Firstly, it was agreed that SRL's X-Ray point source control computer would act as a server to SAL's stepper control computer. In short, SAL's computer will issue commands for action or requests for information, and SRL's computer will respond appropriately. Secondly, a provisional list was drawn up of commands and informational requests. An expanded version of this list is presented in Table 11. Thirdly, it was agreed that all communications between the machines would employ TCP/IP protocol. In particular, the communications structure would follow the conventions set up by SAL for use on their present steppers. These protocols are presented in Table 11.

Fourthly, it was agreed that SRL's system would keep track of the X-Ray dose as it accumulates, and that SRL's system would terminate the accumulation when the dose fell within certain limits of the requested dose. Finally, it was assumed that each system, the X-Ray point source and the stepper, would control their own internal functions as they see fit. This means that the choice of computer, operating system, and software is immaterial as long as the mutual functionality and reliability are not impaired.

Internally, the two systems employ significantly different control architectures. SAL's tool is controlled by a PC running RMX operating system. Programming is performed in C. Communications with external hardware is through a TCP/IP protocol. SRL's laboratory prototype is controlled through National Instrument's LabView V software running under Windows 95 on a power PC. Communications with external hardware is primarily carried out through a National Instruments SCXI bus. The X-Ray point source scheduled for delivery to Sanders will likewise be controlled by LabView with a possible upgrade of the operating system to Windows NT.

LabView is a graphical programming language offering rapid program development and program modification while retaining the speed of compiled C. Most plug in boards, signal conditioners, and instruments capable of computer control are available with LabView drivers. A significant architectural difference between LabView and C is that LabView is data driven rather than command driven. This means that any "virtual

instrument", (the equivalent of a function in C), will run whenever all of its data inputs are available. If a particular sequence of certain functions is important, the exact order in which the functions execute can be controlled. It is SRL's judgment that these differences in internal architecture will not place any impediments to the successful linking of the two systems. LabView fully supports TCP/IP communications in a straight forward manner. The "LabView TCP/IP Appendix" to this document reproduces the portions of the LabView manual which describes this capability.

Table 11: X-Ray Source Control Message List

SAL STEPPER Command	SRL SOURCE Response
Any Command	Acknowledge Receipt
Report Status	State # Initialization Parameters ID and timing of Required Service
Go to State 0 (only manual return)	Service Mode
Go to State 1	Computer On
Go to State 2	Pressure diagnostics on Chamber vacuum pump on Chamber gate valve open Discharge chamber pumped to base pressure
Go to State 3	Chamber gate valve closed Beamline vacuum pump on Beamline gate valve open Gas flows on Chamber at operating pressure All diagnostics on Chopper cooling on Chopper on and synchronized
Go to State 4	Driver and head cooling flows on Line power connected to DC Supplies
Go to State 5	Charge interlocks off X-Ray shutter open
Start	Reset accumulated dose to zero Begin accumulating requested dose (State 6) Go to State 5 & report dose when finished
Pause	Cease accumulating requested dose Go to State 5 & report dose
Resume	Continue accumulating requested dose (State 6) Go to State 5 & report dose when finished
Abort	same as Go to State 1
Calibrate Output	Go to State 5 Fire for preset number of pulses Save average energy per pulse & report Go to State 4
Initialize Parameters -pulse frequency -mask dimensions -source to mask distance -mask material and thickness -total dose	-set interpulse timer -set mask blades -adjust dose scale factor -adjust dose scale factor -set dose limit

The physical data link between the two systems will employ a standard 10 Mb/s Ethernet hookup. SAL uses Intel User Express Ethernet cards. Connectors are either coax or RJ45. Although SRL has experienced no noise problems related to operation of the X-Ray source, as a general principle it would be advisable to use an optical isolator in the Ethernet connection.

The dose delivered by each pulse of the X-Ray point source will be detected at some point in the beamline downstream of the X-Ray window. CXrL has the responsibility of providing the X-Ray detector. They have proposed the use of solar cells. Solar cells could be located on the upstream side, (the side facing the source,) of one or more of the movable field defining shutters so that the active region of cells are immediately adjacent to the X-Rays exposing the print field. Measurements are taken downstream of the window in order to include the X-Ray window transmission. Hence, if there is a gradual change in transmission with time due to a build up of deposits on the X-Ray window, this change will be detected, and the number of pulses may be increased to achieve the desired total dose.

SRL has the responsibilities of recording the electric charge generated on each pulse striking the detector, of processing that data to determine the accumulated dose, and of terminating the pulsing of the point source when the dose falls within certain limits of the requested dose. As presently implemented at SRL, charge generated by each X-Ray pulse in a PIN diode detector is deposited on a small capacitor. The resulting voltage on the capacitor is amplified by a fast high impedance unity gain amplifier and is then fed to a 10 bit digitizer. The digitized signal is appropriately scaled by the SRL computer to give the pulse energy per unit area at the resist. During the exposure of a single field, SRL's software keeps a running total of energy per unit area, ("dose"), delivered to the resist as well as the current running average, (over the partial exposure), of dose per pulse. Following each pulse, SRL's software determines whether or not the accumulated dose is less than the requested dose minus one half of the measured average dose per pulse. If it is not, and neither a pause or abort command has been received from the stepper, another pulse is delivered. If it is, or if a pause or abort command is received from the stepper, pulsing ceases. The measured value of the actual dose delivered is then transmitted to the stepper.

The provisional list of commands worked out jointly between SRL and SAL has been expanded by SRL. The expanded list is presented in Table 12. The syntax employed in this table and in the accompanying discussion is intended to be descriptive. The actual syntax of commands used by SAL is in the form of a "Job ID" number, a "Command" number, and block of data, if any. Once the descriptive list of commands is finalized, a "Job ID", and "Command" number will be assigned to each item in the list.

The source status has been broken down into six principle states. Operational readiness increases with state number from State 1, in which the control computer is capable of accepting commands, through to State 6 in which the X-Ray exposures are being made. The normal "resting" state of the X-Ray point source will be in State 2, with the source chamber under vacuum. At least 5 minutes before exposures are first required, the system gas flows and chopper operation needs to be established by transitioning to State 3. Line power connections to the drivers and cooling flows to the electrodes are established in the transition to State 4. This transition from State 3 to

State 4 will take only a few seconds. The system would be commanded to reside in State 4 during automated wafer changes. The highest state of readiness is State 5, in which the X-Ray shutter is opened, and the X-Ray source drivers are enabled. The time for transition from State 4 to State 5 will be dominated by the X-Ray shutter opening time. CXrL has the responsibility of supplying this shutter. If the shutter cycle time is not much shorter than the estimated 1/2 sec stepper inter field positioning time, it would not make sense to close it during stepping. Likewise, if cycling the shutter for every field would impose excess wear on the shutter or vibration on the stepper, it would not make sense to close it during stepping. Instead, the system would automatically return to state 5 after exposing each field.

When the source is producing X-Rays, it is in State 6. This state is reached by either the Start or the Resume command. The Resume command will be obeyed only if 1.) a Pause command was issued before the requested dose was reached, or 2.) internal X-Ray Source fault detection directed the interruption of X-Ray production and the return of the system to an appropriate state.

With two exceptions the Stepper can command the transition from any state to any other state, without specifying the intermediate states. The X-Ray Source will automatically carry out the necessary intermediate transitions. For safety reasons, the Stepper cannot command a transition out of State 0, the service state. This must be done manually by an operator on the X-Ray source computer. Again for safety reasons, the Start and Resume commands can only be obeyed if the system is already in State 5.

The Start, Pause, and Resume commands are sufficient to control the exposure process. If a pause is called for during an exposure, a Resume command will complete the exposure from the level where it left off. If the exposure is to be abandoned for whatever reason and a new field is to be expose, the Start command should be used. The Initialize Parameters commands are largely self explanatory with the exception of "mask material and thickness". The dose delivered to the resist will depend on the transmission of the mask as will the spectrum of the X-Ray source. Because the spectrum is a characteristic of the source, it is appropriate that the source computer perform the scaling to convert the X-Ray readings into dose.

In summary, a simple TCP/IP Ethernet based control interface between the stepper and the X-Ray source has been identified. The outlines of the communication protocol and the content of the control messages have likewise been identified. The differing software and operating systems currently used by the stepper and the X-Ray source will fully support the planned interface.

Table 12: X-Ray Source Command/Response Format

Definition of Terminology	
Client (SAL's Stepper)	The system requesting functions or information.
Server (SRL's X-Ray Source)	The system providing services over the TCP interface.
Command	A request from the Client for the Server to perform a function.
Response	Results of a previously initiated command returned by the Server to the Client.
Job	A single server process that can be accessed externally.
Transaction	A complete Command/Response sequence

Command Block Format		
Name	Size (in bytes)	Description
Job ID	2	An identifier for the Server process. This allows the Server to modularize the external command set into functional blocks.
Length	2	Size of the following data (including length)
Command	2	Command number
Transaction ID	2	An identifier set by the Client. The Server returns this identifier with the associated Response. This allows the Client to send multiple overlapping commands.
Status	2	Error Code, (zero for no errors)
Data	Length - 8	Data defined by the Command being sent.

Response Block Format		
Name	Size (in bytes)	Description
Job ID	2	An identifier for the Server process. This allows the Server to modularize the external command set into functional blocks.
Length	2	Size of the following data, (including Length)
Response	2	Response number, typically the same as the Command number.
Transaction ID	2	The identifier sent by the Client in the Command Block. The Server returns this identifier to allow for multiple overlapping commands.
Status	2	Error Code, (Zero for no errors)
Data	Length - 8	Data defined by the Response being returned.

Point Source Design Configuration Considerations:

The system interface design requirements study for the point source has been completed. A description of this activity and conclusions follows.

The original configuration goal was to have the source of X-Rays, the DPF pinch, placed at a horizontal distance of 70 cm from the X-Ray mask. A closer spacing was not to be entertained because the global divergence was considered unacceptable. A larger spacing was undesirable, because of the $1/r^2$ fall decline in dose with distance. However, it was realized that mutual interference between the source and the stepper could dictate a spacing somewhat larger than 70 cm. Potential areas of interference included the region between the DPF feed plates and the stepper base, and between the DPF chopper and equipment mounted on the granite stepper upright.

A further constraint was placed on the configuration by the necessity to match a beam line height set by stepper constraints. Moreover, the overall height and width had to be compatible with the clean room being prepared at Sanders. Whether or not the source is to be in the clean room, or separated from it by a wall or other barrier is an issue that has just been resolved. Depending on design, a wall or barrier could force a spacing greater than 70 cm.

A collimator that exhibits output gain relative to that obtained with no collimator at nominal 70 cm spacing must collect radiation from a larger solid angle than that collected with no collimator. Accommodation of a larger solid angle has significant implications on the DPF design. Affected components include the central electrode, the chopper, and the beamline.

Finally, the tradeoffs must eventually deal with X-Ray window and beamline issues. Full size, 3 cm x 3 cm, atmospheric pressure window transmission exceeding 50% should be possible, as opposed to the 10% values typical for thick beryllium windows of the required size that could support atmospheric pressure. In addition, it is frequently assumed that transmission losses through a beamline filled with atmospheric helium are minor. In fact, at the DPF source's effective wavelength, (as measured by Juan Maldonado), of 1.14 nm the transmission through a meter of helium is only 44%. The beam path within the stepper involves transmission through 47.5 cm of He. This transmission is 68%. It should be noted that if the final window can eventually be moved closer to the mask, there is room for significant throughput improvement. Consequently, absolute throughput issues will not be discussed.

Interface with Stepper:

The stepper includes an exclusion zone for general compatibility considerations in multiple applications. In general, no part of the source should intrude into this zone. The principle boundary of this zone is a plane which is normal to the X-Ray axis, and which is located 55.0 cm from the mask along the direction of the X-Ray axis. In the region of the horizontal granite slab that forms the stepper base, the zone becomes more restrictive. There, the zone boundary is 57 cm from the mask. Consequently, the pulsed power feed plate of the DPF, which is normal to the X-Ray axis and which extends up from near floor level, can be placed no nearer than 57.0 cm from the mask. The X-Ray pinch forms approximately at an axial position that is coincident with the end

of the central discharge electrode. Assuming use of the nominal 5.5 cm long central discharge electrode, the axial distance from the pinch to furthest surface of the pulse power feed plate is 10.4 cm. Thus, if the pulse power feed plate is placed 59.6 cm from the mask, the source will be at the desired 70.0 cm from the mask.

If a chopper is not employed, the desired 70 cm spacing can be readily achieved. Two new design elements could allow operation without a chopper. Neon gas is now introduced through the anode into the chamber. The gas flow is in a direction opposite to that of the extracted X-Rays. It is expected that this flow will reduce or eliminate any flow of particulate or vapor towards the X-Ray window. The deliverable machine will employ a thermophoretic particle precipitator. It is expected that this device will greatly reduce the population of particulate that are suspended in the gas. Even if these innovations are as successful as hoped, a chopper could still be required to block a pinch generated shock wave from damaging the X-Ray window. Measurements will have to be conducted to determine if the window is at hazard from these shock waves. The primary housing of the present chopper extends 16.9 cm in the axial direction from the source. If this housing were to be placed adjacent to the principle boundary of the exclusion zone, the source would be 71.9 cm from the mask, approximately two cm larger than the goal. This would result in a 5% loss in fluence at the mask as compared with the 70 cm distance. The motors of the present chopper extend out an additional 20 cm from the chopper housing. If the motors were to be placed adjacent to the principle boundary of the exclusion zone, the source would be 92 cm from the mask. This would result in a 42% loss in fluence at the mask as compared with the 70 cm distance. This is unacceptable. Clearly, the motor problem must be addressed. SAL has offered relief by making a region in the exclusion zone available for motor placement. This region is in the cutout area near the top of the vertical granite piece. The distance from the motor axis to the optical axis is approximately 46 cm. This would allow the use of a directly driven drive wheel approximately a meter in diameter, or a smaller wheel with a belt drive. Two wheel designs would be difficult. An alternate approach would be to use a disk that is sufficiently large so that the drive motor could be placed to one side of the vertical granite piece of the stepper, thereby avoiding the exclusion zone. The distance from the optical axis to the side of the granite block is approximately 56 cm. Such flexibility can be achieved by bringing the chopper axle or axles through the triplate transmission line. High voltage insulation would be achieved by a variation of the proven methods now employed for through bolts.

Beam Height and Overall Height:

In order to deal with the beam height specification and overall height limits on the DPF source, a new architecture for the modules was identified, modeled extensively, and tested using a modified module of the current architecture. Basically, the new machine will have a suite of eight modules instead of the current count of twelve modules. The eight module architecture turns out to be quite favorable in terms of its spatial configuration. The modules will be arranged in two stacks of four. The individual module will have the same height as the present modules. This turns out to place the beam height at the prescribed 1100 mm while allowing a 2.75" space beneath the support frame. This gives adequate space for passage of cooling, vacuum, gas, diagnostic, and control lines. The overall height of 6.38 ft falls below the 7.5 ft limit set by the overhead crane at the Sanders' facility. These design changes have been made with no compromise in output capability.

Collimator Accommodation:

A collimator with gain requires that more solid angle be collected from the point source. The X-Rays are extracted through an aperture in the hollow anode. The increased solid angle means that this aperture must increase. The 150 mr full angle accepted by the Focused X-Rays LLC collimator design is approximately 2.5 times that with no collimator at a 70 cm standoff. Differential pumping from an aperture with six times the area is impractical. However, this has already been addressed with the scheme of reversed gas flow. Here, fresh gas enters the anode at subsonic velocity through the aperture, thereby assuring that the X-Rays form in and propagate through clean gas.

The skirt of the present anode is large enough to pass the full solid angle. However, there is an issue with the e-beam deflecting magnets that are placed in the skirt. Either they could be moved out radially to the anode base, or left in place to obscure part of the collimator acceptance aperture. The magnetic field would be decreased in the first case. Experiments will have to be conducted to determine if, with a weakened magnetic field, the inductive e-beam could still be deflected before it hits the vacuum window, which is just beyond the shutter. The second solution would result in a small loss of output. It is anticipated that this would be less than 10%.

The chopper must be changed to accommodate the acceptance angle required by the collimator. Increase in acceptance angle means that the chopper window size must increase proportionately. If an enlarged window is to be closed by the chopper in the same time as a smaller window, the rim speed of the chopper wheels must increase in proportion to the ratio of the window dimensions. Increase in rim speed can be achieved either through increase in rotational speed, increase in wheel diameter, or a change in both design parameters. At this point in time, an increase in wheel diameter and a decrease in rotational speed appear attractive. A decrease in rotation speed would be favorable for bearing lifetime. An increased diameter would allow for more flexibility in the location of the drive, for the bearing lifetime enhancing decrease in rotational speed, and for a single, versus a double wheel system.

If experiments show that a chopper is required, SRL proposes a simple straightforward design. In the absence of a collimator, this design would allow the pinch to be located within 72 cm of the mask. A single disk with a diameter slightly greater than a meter would be employed. It would be driven by a shaft that extends through the high voltage triplate. A magnetic coupling would connect this shaft to a variable speed synchronous motor mounted on the head side of the DPF. The disk would have two cutouts to insure balance even if there are deposits. The cutouts, which are approximately 2 cm in diameter, would accommodate the full solid angle of the collimator proposed by Focused X-Rays LLC. A rotational speed of approximately 4000 rpm would allow pulse repetition rates of 130 Hz. Rim speed would be approximately half the speed of sound in Ne. This yields a closing time of less than 100 ms. The disk would intercept shock waves or debris material moving a speed up to order Mach 2. No elaborate synchronization of the disk to the DPF source would be required, as is the case with the present two disk system, because the firing of the source would be synchronized to the disk angular orientation. The disk would be dynamically balanced to eliminate objectionable vibration levels. It would be suitably encased so that any catastrophic failure would be contained.

Beamline Interface:

SRL will design the DPF source so that it will function either with or without a collimator. SRL's proposed approach is to insure that the anode and chopper accommodate the larger solid angle of a collimator.

The collimator needs to be positioned downstream from and immediately adjacent to the first vacuum window that, in turn, is just downstream from the chopper. Because of their proximity to the high voltage anode, all of these components must pulse to high voltage. This means that the high voltage break in the evacuated beam line must be downstream from the collimator. A coaxial ground shield would extend from the chopper ground shield to the grounded side of the high voltage break in order to effect complete EMI shielding. If the machine were to be operated without the collimator, the only difference would be to mount the high voltage break immediately downstream from the first vacuum window, and to employ a shorter coaxial ground shield. The inner interface must provide 1) registration and mechanical support for one end of the beamline tube, 2) electrical contact with the beamline tube, and 3) a vacuum seal between the moderate vacuum, (torr level), of the chopper housing and the external atmosphere. The outer interface need only provide electrical contact between the chopper housing and the beamline electrostatic shield.

The window near the X-Ray source must be capable of supporting an atmospheric pressure difference, or the beamline must be capable of adjusting its pressure in synchrony with the pressure in the chopper housing during servicing of the source. In terms of throughput, the second choice is preferable because a more highly transmitting window could be employed. As the source is brought up to atmosphere, a clean inert gas would be introduced into the beamline at a rate to maintain zero pressure difference across the window. (Filling with clean gas, as opposed to simply opening a high conductance port between the chopper housing and the beamline, insures that the X-Ray mirror remains free of contamination). SRL employs a diaphragm type gauge to monitor chamber pressure in the region between 1 atm and 1 torr. The difference between the electrical output of this gauge and the output of an identical gauge mounted on the beamline could provide a signal to electrically operated valves controlling the fill and evacuation of the beamline in a manner that maintains at most a small pressure differential across the window.

Point Source Interface Conclusions:

The point source, including a chopper, can be configured to give 95% of the output that would be obtained with the baseline 70 cm pinch to mask spacing if no collimator is employed. If a collimator is employed, the point source, again including a chopper, will be able to take full advantage of the proposed output enhancements due to increased solid angle collection. No interface impact on alignment precision, wafer overhead, or step and repeat times has been identified. By far and away the most important leverage on throughput can be obtained through improvement in atmospheric window design.

A013: SOW Task 3.2.5: Compatibility with Laser Based Point Source

As a possible alternate to the SRL source, in this task, the laser based X-Ray source being developed by JMAR will be evaluated. Measurement of source output is included.

CXrL conducted measurements and analysis of the laser based point source system being developed by JMAR Industries. This study was motivated by the desire that the Point Source Lithography System being developed would be compatible with an alternate source, if possible.

Background Information on JMAR source:

This information was obtained during a visit to JMAR on July 15, 1997 and on 10 September, 1997.

Laser power -	125 -160 mJ/pulse for 1064 nm wavelength
Laser power -	80-100 mJ/pulse for 532 nm wavelength
Repetition rate -	10 Hz
Conversion Efficiency	
to 532 nm light -	50% from 1064 nm wavelength
to X-Rays, (2π sr) -	4% for 1064 nm wavelength
	5 to 6 % for 532 nm wavelength

Expectations for the Future:

Sixteen modules with 250 W power each are planned, and will allow operation with 1000 Hz repetition rate and 1064 nm wavelength. Multiple 10 to 15 μ m diameter spots can be projected with the same lens, (100 mm focal length), on a copper tape simultaneously within an area of \sim 200 μ m. This corresponds to 2000 W of 532 nm wavelength laser energy. With an efficiency of 5.5%, we obtain 110 W/ 2π sr of X-Rays. At a distance of 66cm, (J. Maldonado's approach), it will produce \sim 4 mW/cm². This number will be reduced due to absorption in atmospheric Helium.

JMAR X-Ray Source Spectrum:

A spectrum analogous to that of the JMAR source was obtained from Lawrence Livermore National Laboratory, (courtesy of Steve Lane).

JMAR Source Evaluation:

During the visit to JMAR on September 10, 11, and 12, a series of experiments were performed. The source is contained in a chamber. A "beamline" connected to the chamber and terminated with a valve provided convenient connections with the end-of-the-line attachments. An enclosure able to contain a Polaroid cassette with film was attached to the "beamline" providing a distance of \sim 62 cm from the source to the film plane. The beamline together with the enclosure was filled with He and He flow was maintained during exposures. To ensure sufficient helium flow, a detector was used to monitor residues of oxygen in the beamline and enclosure. The exposures were performed when the detector indicated the partial relative pressure of oxygen to be $<1\%$. All the experiments were performed using green light, $\lambda=532$ nm, and a repetition rate of 10 Hz in a single channel regime. The laser light was focused into a few micrometer spot on the copper foil tape, (\sim 25 μ m thick), producing effectively an X-Ray

source of a few μm in size. The final hole punched in the tape is typically 20-30 μm in diameter, reflecting an area with a temperature higher than that of Cu sublimation.

On September 10th and 11th, the single channel 640 mW laser regime, (10 Hz), was employed, corresponding to 64 mJ of green light per pulse and providing more than 1.7 mJ of X-Rays per 2π sr per pulse. In this regime, 24 exposures were made and initial conditions for the following experiments were established.

For quantitative experiments performed on September 12th, the laser system was re-tuned to a high efficiency, (>5%), and harder X-Ray conversion mode: with the same 10 Hz repetition rate the laser power was raised to 83-87 mJ per pulse yielding ~ 4 mJ of X-Rays per 2π sr per pulse. In this regime, 46 exposures were recorded.

Seventy exposures on a Polaroid film have been recorded using different combinations of Al filters. The thickness combinations of Al filter are listed in the Table 13.

Combination #	1	2	3	4	5	6	7	8	9	10	11	12	13	14	15	16	17
Al thickness, μm	2.5	4	6.5	8	10.5	12	14.5	15	17.5	19	22.5	23	27	31	34	38	42

Table 13: Al Filters Combinations Used in JMAR Laser Plasma Source Spectrum Evaluation

The number of shots for exposures was maintained to provide the film exposure response within approximately the same range: ~ 50 to 80% of the maximum value. The Polaroid pictures were scanned and the luminosity values were measured on an 8 bit, (256 level), gray scale. Obtained data were normalized to a single shot and compared with attenuation of Al filters calculated using PCTransmit software. A single fitting parameter, F , its standard deviation, s , and their ratio s/F , (relative standard deviation RSD), were calculated for 24 spectra including one obtained from Lawrence Livermore National Laboratory. The spectra were synthesized using results of aluminum filter attenuation experiments. The RSD value was used as a criterion to optimize a simplified spectrum and ranged from $s/F = 10.97\%$ to 21.02% . The experimental spectrum from Lawrence Livermore National Laboratory revealed a reasonably small value $s/F = 12.82\%$. The smallest obtained RSD = 10.97% is less than, but close to that for the "real" spectrum, (RSD=12.82%). The analysis indicate little dependence of that criterion on details of the spectra, and that, indeed, the spectrum for the JMAR source can be effectively presented in a range of photon energies from 1030 to 1300 eV.

JMAR Laser Plasma X-Ray Point Source Power Estimation:

The fitting parameter, F , was used to estimate the X-Ray power output from the source. The values were corrected according to the effective photon energy of the filtered spectra, (~ 1150 eV). The calibration exposures were performed on the ES-5 beamline at CXrL, equipped with two grazing incident 2° mirrors designed for X-Ray lithography. The grazing incident optics eliminates high-energy photons and thus provides the

closest spectra to that of X-Ray point sources. To achieve proper exposures for Polaroid film, (100 - 600 nJ/cm²), a 100- μ m thick Al filter was used. The attenuation factor of 4.03×10^{-6} at the effective photon energy of 1500 eV was calculated using PCTransmit for a realistic combination of the filter and 270 mm of atmospheric He. The fitting parameter for the estimated spectra, (see above), with the RSD not exceeding S/F = 13%, (value close to that of the "real" spectra), was ranging from F=100 to F=150 equivalent with the most probable value of F = 125 corresponding to

$$W = 5.6 \text{ mJ/pulse into } 2\pi\text{sr}$$

This value is larger than that measured using a PIN diode: $W \approx 4 \text{ mJ/pulse} \cdot 2\pi\text{sr}$.

JMAR Laser Plasma X-Ray Point Source Uniformity Estimation:

The uniformity of the source was estimated using the statistical feature "Histogram" of the Adobe Photoshop image processor. This feature returns average value and standard deviation of luminosity presented in 256 gray levels. These parameters are estimated for the background, ($I_B = 5.6$, $s_B = 3.48$), and in the exposed areas, ($I_E = 209.8$, $s_E = 3.5$). The normalized standard deviation of the exposure field, U_F , is used to estimate the uniformity of the exposure field:

$$U_F \equiv \frac{\sigma_F}{I_F} = \sqrt{\sigma_E^2 - \sigma_B^2} / (I_E - I_B),$$

where I_F and σ_E are the luminosity and standard deviation of the exposure field. Substituting values for symbols, we obtain:

$$U_F = \sqrt{3.5^2 - 3.48^2} / (209.8 - 5.6) = \frac{0.38}{204} = 0.0018 = 0.18\%,$$

which is very uniform. The result

$$U_F = 0.18\%$$

means, that the possible non-uniformity is quite small and its actual value is substantially smaller than the noise of the measurements.

JMAR Laser Plasma X-Ray Point Source Size Estimation:

To estimate the source size, a penumbra blurring effect was used. Two razor blades were positioned, (one horizontally and one vertically), at 5.7 cm from the source to cast a shadow on the film 56.7 cm behind it with a magnification ratio of $M = 56.7/5.7 = 9.95$. Images of razor blades and the closest aperture edge, and the stencil mask holes, were recorded with a high-resolution negative Polaroid film type 665. The resolution of this film is 160-180 line pairs per mm, which is equivalent to a $\sim 3 \mu\text{m}$ pixel. The images were scanned in using a HP scanner with optical resolution of 600 dpi, (an optical dot of $w = 42.3 \mu\text{m}$).

Another limiting factor in determining the source size is diffraction. For long distances, the 10-15 Å wavelengths produces a significant diffraction effect. This effect can be calculated using equations based on Fresnel diffraction of light on a straight edge. The

distance between points where the intensity changes from dark, (25%), to the bright, (75%), in the plane of recording is given by a formula

$$\Delta = \sqrt{\frac{b \lambda (a + b)}{2 a}},$$

where a is the distance between source and the edge, b is the distance between edge and the observation plane, (film), and λ is the effective wavelength. The diffraction effect on the blade edge, $\Delta \approx 45 \mu\text{m}$, is very strong in comparison with that of the aperture edge, $\Delta \approx 2.3 \mu\text{m}$.

The scan-in resolution can be controlled providing interpolation within the optical dot. We used 6 pixels per optical dot, or $7 \mu\text{m}$ per pixel. The half-width, W , of the edge definition consists of 6 pixels and is limited by the HP scanner optical resolution W : $W \approx 42 \mu\text{m}$.

The aperture edge consists of 6 pixels or $42 \mu\text{m}$ and the blade edge has 11 pixels or $77 \mu\text{m}$. Based on these data we can estimate the source size. Using the formula

$$PB = \sqrt{W^2 - \Omega^2 - \Delta^2},$$

the broadening of the blade edge image due to the penumbra blur associated with the source size can be found. Dividing that value by a magnification factor, $M = b/a$, the source size L can be estimated as

$$L = PB/M.$$

Calculating penumbra blur:

$$PB = \sqrt{77^2 - 42^2 - 44.8^2} = 44.8 \mu\text{m},$$

and dividing this value by the magnification factor $M=10$, an estimation of the source size gives a value of

$$\Lambda \sim 4.5 \mu\text{m}.$$

JMAR Source Evaluation Conclusions:

- The experiments allowed establishing the spectral range of the JMAR laser plasma X-Ray source: the spectrum of the JMAR source can be presented in a range of photon energies from 1030 to 1300 eV with the effective energy of 1150 eV. The spectrum is well suitable for the sub- $0.15 \mu\text{m}$ lithography.
- The JMAR source is substantially smaller than the SRL: 100 times in end on configuration for the SRL source, and 1000 times in the other direction.
- The spatial uniformity of illumination of the JMAR source is better compared with the SRL source.

- The JMAR source offers more convenient access and can easily support more than one exposure station.

Appendix A: Revised System Specifications

1.0 Introduction

This document is a revision to the system goal specification for the Point Source X-Ray Lithography System contained in Tables 1 and 2 of the Statement of Work for Contract N00019-97-C-2001. This revision reflects additions and changes that resulted from 1.) inputs solicited from gallium arsenide IC manufacturers; 2.) inputs for Sanders wafer fabrication personnel resulting from experience using the Model 4 stepper at CXrL; 3.) revisions arising from improvements in source and stepper as a result of work accomplished in Phase 1 of this program. This revision does not modify any contractual requirements as specified in the contract Statement of Work.

This document describes a specifications for a Point Source X-Ray Lithography System intended for use in fabrication of GaAs MMIC and QWIP devices having critical dimensions of 0.15 μm or less. The System is being developed under Contract N00019-97-C-2001; Sanders, a Lockheed Martin Company, is the prime contractor. The major sub-contractors, and their areas of responsibility, are:

Suss Advanced Lithography, (SAL) - Wafer Stepper, System Integration
Science Research Laboratories, (SRL) - X-Ray Point Source, Bichromatic
Interferometer. (under subcontract from SAL)
Center for X-Ray Lithography, Univ. of Wisconsin, (CXrL) - Beamline

This development program is divided into two phases. In Phase 1, critical stepper components will be demonstrated using an existing SAL Model 4 stepper test bed installed at the synchrotron ring at CXrL; the facility will also be used by Sanders in developing MMIC processes with 0.25 and 0.15 μm features. SAL will also commence fabrication of the Model 5 stepper, SRL will build and demonstrate a prototype X-Ray point source, and CXrL will design a beamline. In phase 2, SRL will build the production point source unit and deliver it to Sanders where the point source, CXrL fabricated beamline, and Model 5 stepper will be integrated into a complete Point Source X-Ray Lithography System.

This specification addresses goals for both the pre-production, (Phase 1), and production, (Phase 2), stepper, as well as the production goals for the point source and beamline. While specifications for the stepper, point source, and beam line are listed separately in Sections 2.0, 3.0, and 4.0, respectively, it is understood that all specifications must be met simultaneously in the integrated system. Section 5.0 lists specifications common to all sub-systems.

2.0 Stepper Specifications

The stepper is an automated wafer handler, mask handler, and alignment tool which performs precise wafer-mask alignment over a given field size, which is stepped and repeated over a given size wafer during X-Ray exposure. In addition, the stepper will

provide hot and cold plates to pre and post condition wafers as required by the photolithographic process. Finally, all wafer and mask transports will occur in a particulate, temperature, and humidity controlled environment.

2.1 Resolution and Linewidth Control

While the resolution of patterns exposed on the wafer is impacted by the quality of the X-Ray mask, the aligner/beamline/source system must be capable of replicating features on the mask down to the following limits:

	Pre-Production	Production	Units
Resolution	≤ 250	≤ 150	nm
Line Width Control	< 25	< 15	nm, 3σ

2.2 Overlay

The aligner to absolute grid is the variation over a wafer of the distances between the commanded and actual field centers and their associated field corners of a grid of fields printed by the aligner.

	Pre-Production	Production	Units
Aligner to Aligner	70	50	nm, $(x + 3\sigma)$
Aligner to Self	50	33	nm, $(x + 3\sigma)$
Aligner to Absolute Grid	25	20	nm, $(x + 3\sigma)$

2.3 Mask to Wafer Gap

The mask to wafer gap shall be continuously variable between the limits given in the table. The distance between any point on the wafer and any point on the mask shall never fall below 10 μm at any time during normal operation. Provision shall be made for preventing mask and wafer damage due to loss of power or vacuum.

	Pre-Production	Production	Units
Gap - Manual Mode	10 to 20	n.a.	μm
Gap - Automatic Mode	20 to 50	10 to 50	μm
Accuracy/Precision	$\pm 1.0/\pm 0.5$	$\pm 1.0/\pm 0.2$	μm
Uniformity			

2.4 Alignment

	Pre-Production	Production	Units
Technique	ALX-2	ALX-4	n.a.
Modes	N-Site Global Field by Field Mix and Match	N-Site Global Field by Field Mix and Match	n.a.
Operator Assisted/ Automatic	both required	both required	Graphical User Interface

2.5 Throughput (excluding exposure)

The specification below address wafer handling and alignment throughput of the stepper, excluding exposure time and process time such as baking or chilling. Exposure time is a function of X-Ray intensity, beamline design, (e.g. collimation), and resist sensitivity. The intensity and beamline parameters are discussed in Sections 3.0 and 4.0, respectively.

Throughput assumes 20 overlaid fields in the N-Site Global Alignment Mode, where N is the minimum number such that the overlay and line width specifications are satisfied simultaneously.

The Field by Field Alignment Mode throughput assumes each field is aligned and exposed before the next field is measured.

	Pre-Production	Production	Units
N-Site Global Alignment Mode	≥40	≥60	wafers per hour
Field by Field Alignment Mode	≥20	≥25	wafers per hour

2.6 Wafer Types and Sizes

The production stepper is designed for use with a single wafer size only, nominally 150 mm. However, the design shall not preclude handling of different wafer sizes as indicated below. Maximum wafer size change time, defined as beginning with the end of aligner operation in preparation for wafer chuck exchange and ending with the start of cycling of new size wafers, shall be ≤90 minutes.

	Pre-Production	Production	Units
Wafer Type	GaAs and/or Si	GaAs and/or Si	n.a.
Orientation Features	major and/or minor flats	major and/or minor flats, and/or notches	n.a.
Wafer Diameter	75, 150, 200	75, 100, 125, 150, 200	mm
Input/Output	Cassette	Cassette	n.a.
Batch Size	25	25	n.a.

SMIF - Standard Material interface

2.7 Masks

	Pre-Production	Production	Units
Storage/Load	Manual	SMIF	n.a.
Mask Format Envelope	NIST	NIST	n.a.
Mask Exchange Time	45	25	sec.
Field Size, max.	50x50	50x50	mm

2.8 Robotic Handlers and Bake/Chill Stations

Robotic handlers shall be employed on the production stepper for all wafer and mask handling and transfers. There shall be no undue stress placed on the mask or wafers during handling or in place which would hamper the ability of the tool to meet overlay specifications.

Proximity and contact style bake stations with two hot plates, one chill plate, and provision for a second chill plate shall be provided. All handlers and bake/chill stations shall be under software control.

	Pre-Production	Production	Units
Bake Station - over 6 inch central diameter			
Temperature Range	n.a.	50 to 200	°C
Uniformity (max-min)	n.a.	0.6 from 50 to 80 0.2 from 80 to 140 0.6 from 140 to 200	°C
Accuracy (mean-nominal value)	n.a.	± 0.5 from 50 to 80 ± 0.2 from 80 to 140 ± 0.5 from 140 to 200	°C
Chill Station - over 6 inch central diameter		80 to 140 ± 0.1 140 to 200 ± 0.3	°C
Temperature Range	n.a.	15 to 35	°C
Uniformity (max-min)	n.a.	1.0	°C
Accuracy (mean-nominal value)	n.a.	±0.5	°C

2.9 Environment

The system is intended to operate in a Class 100 facility, and all components installed in the facility must be compatible with such environmental protocols.

An environmental chamber shall be provided such that the temperature, humidity and contamination requirements set forth below are satisfied, when operated in a Class 100 facility having a nominal temperature of 68 to 72 °F, a rate of change of not more than 0.5 °F per hour, and a relative humidity in the range of 30 to 50%.

A mask pass is defined as the lesser of one hour residence time in the aligner or the time required to pass 60 wafers, including exposure time.

	Pre-Production	Production	Units
Temperature	n/a	20 to 24 ± 0.2	°F
Humidity	n/a	40 ± 5.0	%
Particulate Environment	n/a	Class 1	n.a.
Particles >200 nm per pass for 200 mm wafers or masks	n/a	1	n.a.
Beamline to Mask Environment	n/a	pure He	n.a.

2.10 Maintainability and Reliability

	Pre-Production	Production	Units
He consumption, max.	n/a	5	SCFH
MTBF	>50	>100	hr.
MTTR	<4	<4	hr.
MTBA	>20	>20	hr.

3.0 Point Source Performance Design Goals

The X-Ray energy for this system is derived from a Dense Plasma Focus source driven by a solid state pulsed power supply. The point source system includes the DPF source, shutters, power supplies, water cooling and circulation, control software and hardware. Following are the Point Source Design Goals as they relate to the performance of the production Point Source X-Ray Lithography System.

3.1 X-Ray Output

	Specification	Units
X-Ray Energy per pulse	20	joule
Pulse Repetition Rate	130	Hz
X-Ray Intensity @ 70 cm from source, (in vacuum)	42	mW/cm ²
Spectral Distribution, (in vacuum)	60% He-a and H-a lines centered @ 12.9 Å 40% He-like and H like continuum centered @ 9.8 Å	
Effective Source Size	<0.5	mm
Field Size @ 70 cm source to mask separation	30x30	mm

Note: provision shall be made to automatically sense the dose at the wafer plane and adjust exposure times accordingly; provision shall be made to minimize or eliminate debris from the plasma discharge from contaminating the beamline and/or mask.

3.2 Maintainability and Reliability

	Specification	Units
Head Life (refurbishable)	10 ⁷	pulses
Power Supply Life	3x10 ⁹	pulses
Anode Change Time	1/2	hr
Ne consumption, max.	72	l/hr

3.3 Environmental/Operational Considerations

The Point Source is intended to operate in a Class 100 facility in proximity to the Stepper, and all Point Source components installed in the facility must be compatible with appropriate environmental protocols during normal operation. Equipment not compatible with a clean room environment shall be installed in an adjacent equipment chase. All equipment must have vibration damping so as to be compatible with device overlay requirements. The Point Source components shall not introduce EMI which would upset the function of other electrical subsystems.

4.0 Beam Line Specifications

The beamline transfers the X-Ray energy from the Point Source to the mask plane at the stepper such that the alignment and system specifications herein will be met with or without a collimator. Design of the beam line shall be such that no mask bias is required to meet lithographic specifications. Provision shall be made to align the Point Source to the appropriate reference point at the stepper, with the beam at normal incidence to the center of the wafer plane. The beamline shall utilize vacuum, or He at near atmospheric pressure.

	Parameter	Condition	Units
Global Divergence	± 30	at corner of 30 x 30 cm field	mr
Local Divergence	± 10	at corner of 30 x 30 cm field	mr
Local Divergence Uniformity	± 0.4		mr
Intensity Uniformity	± 2.0	over 30 x 30 cm field	%
Field Defining Blades ¹	10 x 10 to 50 x 50		mm
Intensity at wafer plane ²	5		mW/ cm ² min
Length	70		cm
He consumption, max.	TBD		SCFH

Note:

1. Field Defining Blades must be capable of dissipating excess X-Ray energy
2. Intensity at the wafer plane must be sufficient to meet wafer throughput system with a resist of 50 millijoules/cm² sensitivity.

5.0 General System Specifications

The following specifications pertain to all components of the Point Source X-Ray Lithography System.

5.1 Facilities Constraints

The system shall be designed to operate in a Class 100 environmental cleanroom. The nominal temperature range of the room shall be 68°F to 72°F, with a temperature variation of not more than 3°F, and a rate of change of not more than 0.5°F per hour. The relative humidity of the room shall be 30 to 50%. Components not compatible with a Class 100 environment may be located in an adjacent equipment chase.

The system shall be designed to fit within a TBD ft. by TBD ft. clean room bay with an adjacent TBD ft. wide chase for support equipment.

The system shall be adequately isolated to operate in a vibration environment which is acceptable to comparable lithography tools.

The power, chilled water and exhaust requirements shall not exceed the following:

	Stepper ¹	Source	Beamline	Units
60 Hz Power				
120 VAC		15		kVa
208 VAC	30	20		kVa
480 VAC		125		kVa
Chilled Water - city, @ 40°F		100		gpm
Chilled Water - de-ionized, @ TBD °F				gpm
Nitrogen @ 75 psi	3.9			cfm
Compressed Air @ 90 psi	0.5			cfm
Vacuum @ <110 mm Hg	0.8			slpm
Exhaust	165 acid 2.1 solvent	150		cfm

Note:

1. Includes Bake Station and Environmental Chamber

5.2 User Interface and Software

The operator shall be provided with an interface to the system via Graphical User Interface software which shall have the capability of linking to the factory's host computer via a LAN. The operator shall be able to control, remotely if necessary, all system operations.

The user interface shall include a diagnostic mode which shall permit access to and control of all normal hardware operations.

Provision for storing and/or transfer of data accumulated in all operating modes, including key alignment and exposure parameters for each exposure field, shall be provided by means of a TCP/IP interface or equivalent.

Any direct interlocks to and from the system which may be required for safety or prevention of damage to the aligner or point source shall be specified. The control interface shall be able to handle unexpected system failures by providing a signal to the point source subsystem in event of failure of the aligner. The aligner shall have a mode that protects the mask and wafer from damage with a minimum loss of exposures in the event of unexpected failures in the point source subsystem.

5.3 Documentation

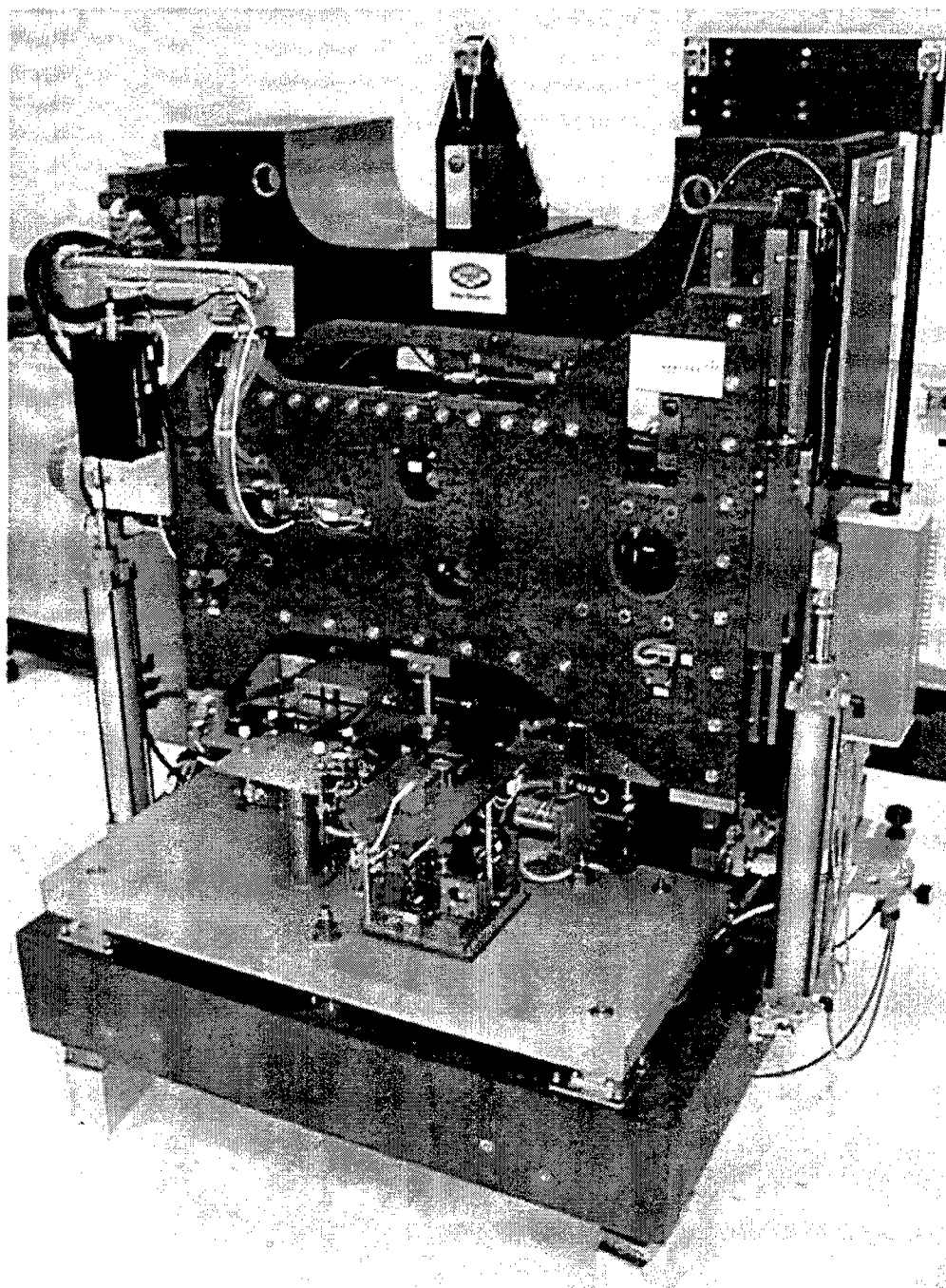
System level operation, training, maintenance and software manuals shall be provided in both hard copy and electronic format.

5.4 Safety

The system shall incorporate shielding, as appropriate, to preclude operators from exposure to X-Ray radiating emanating from any component of the system. The system shall be designed to meet Lockheed-Martin Corp. defined and Government approved safety standards to protect personnel who operate and service the system.

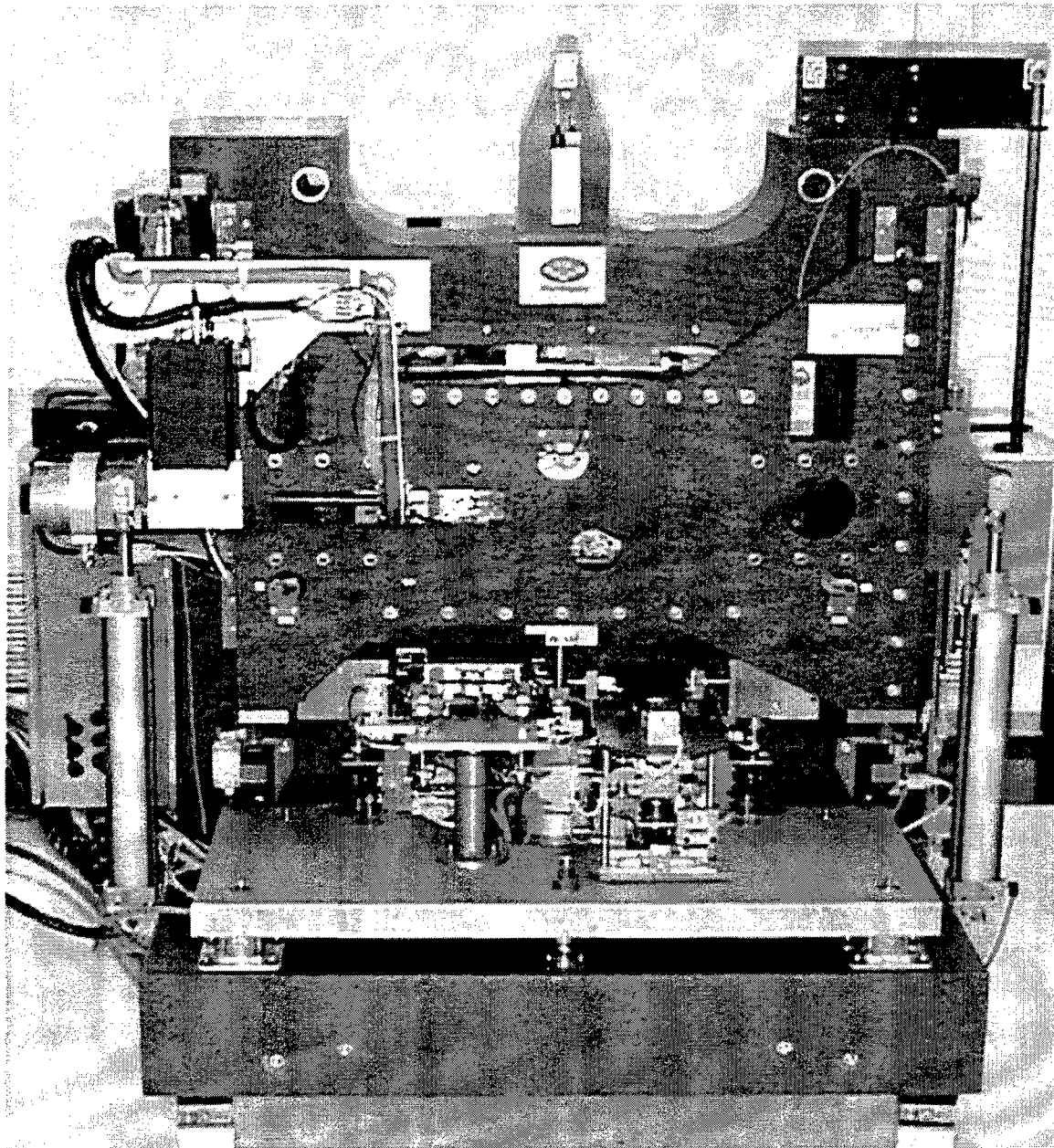
Appendix B: Photographs of SAL Produced Equipment

Model 5 Test Bed



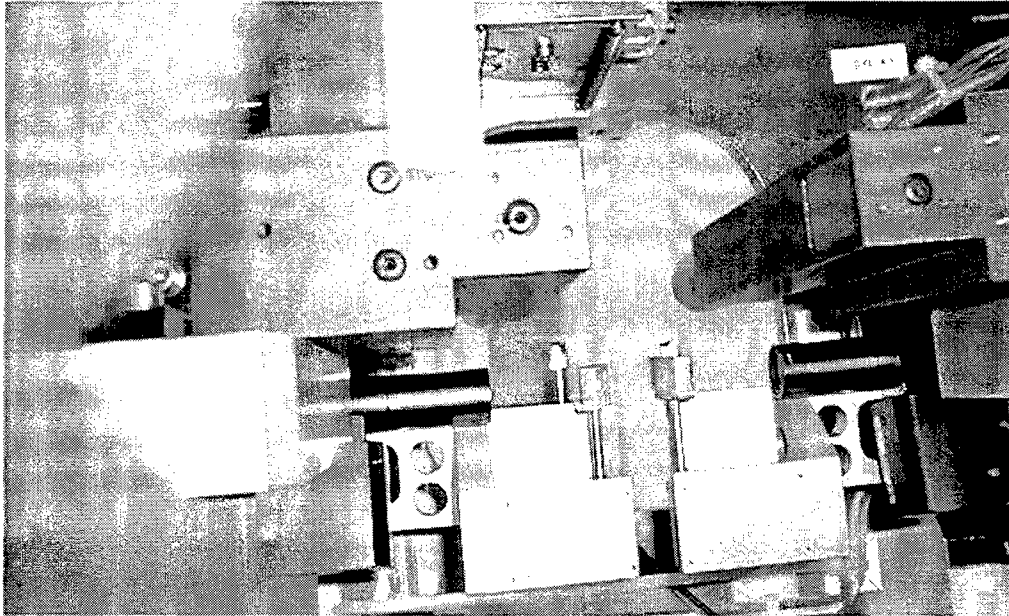
X-Ray Lithography

Model 5 Test Bed

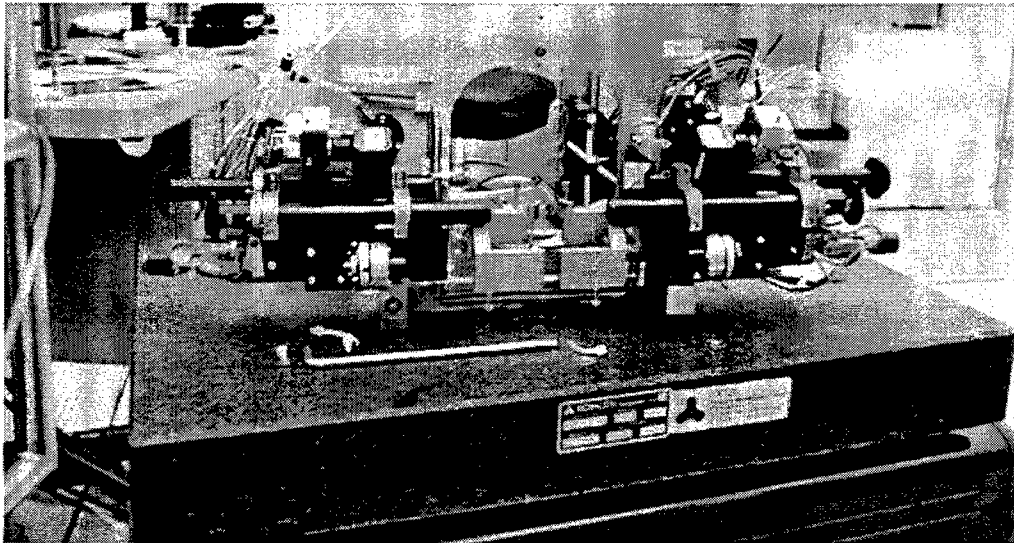


X-Ray Lithography

ALX & IBBI on XRS 2000/1

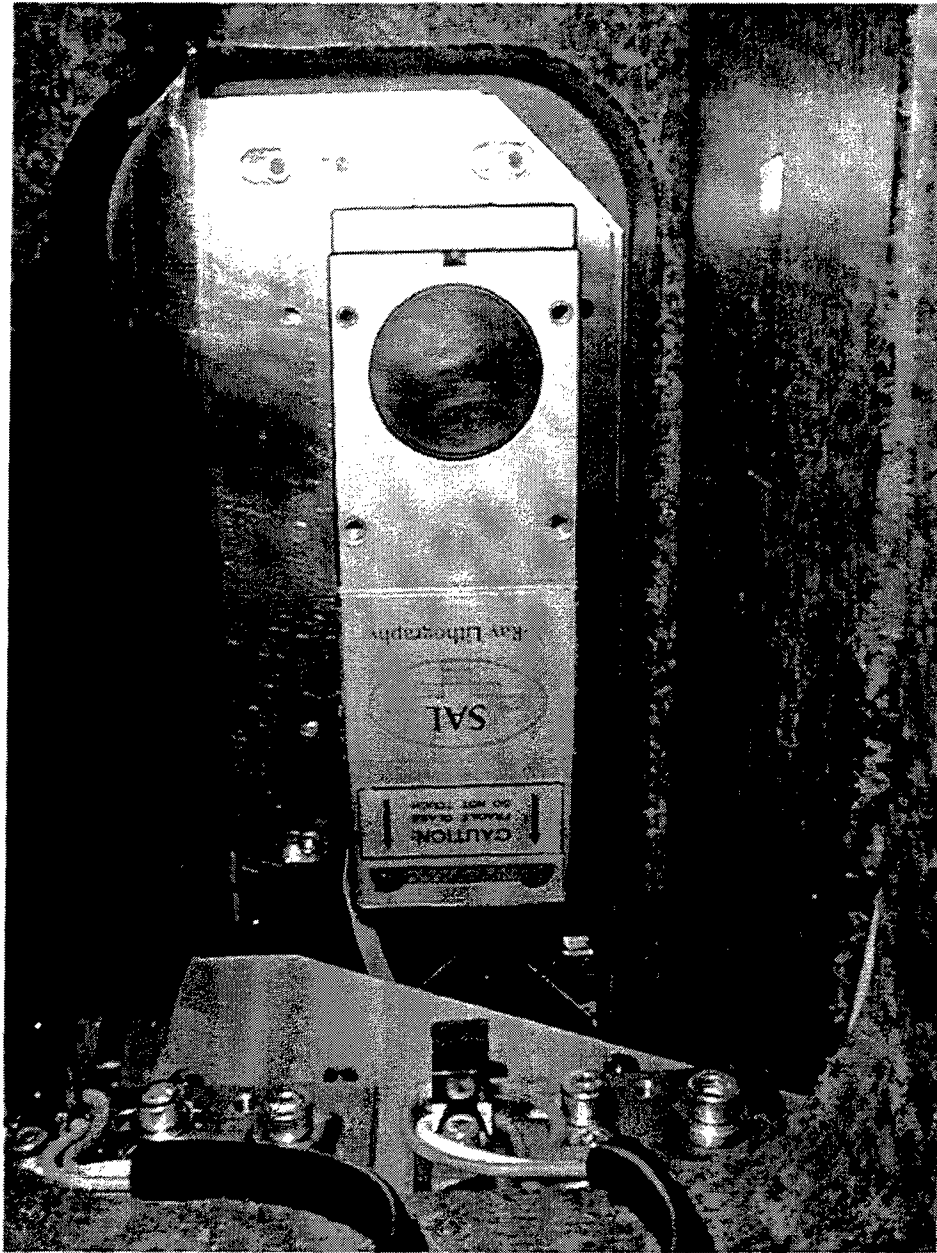


IBBI/4 Alignment System



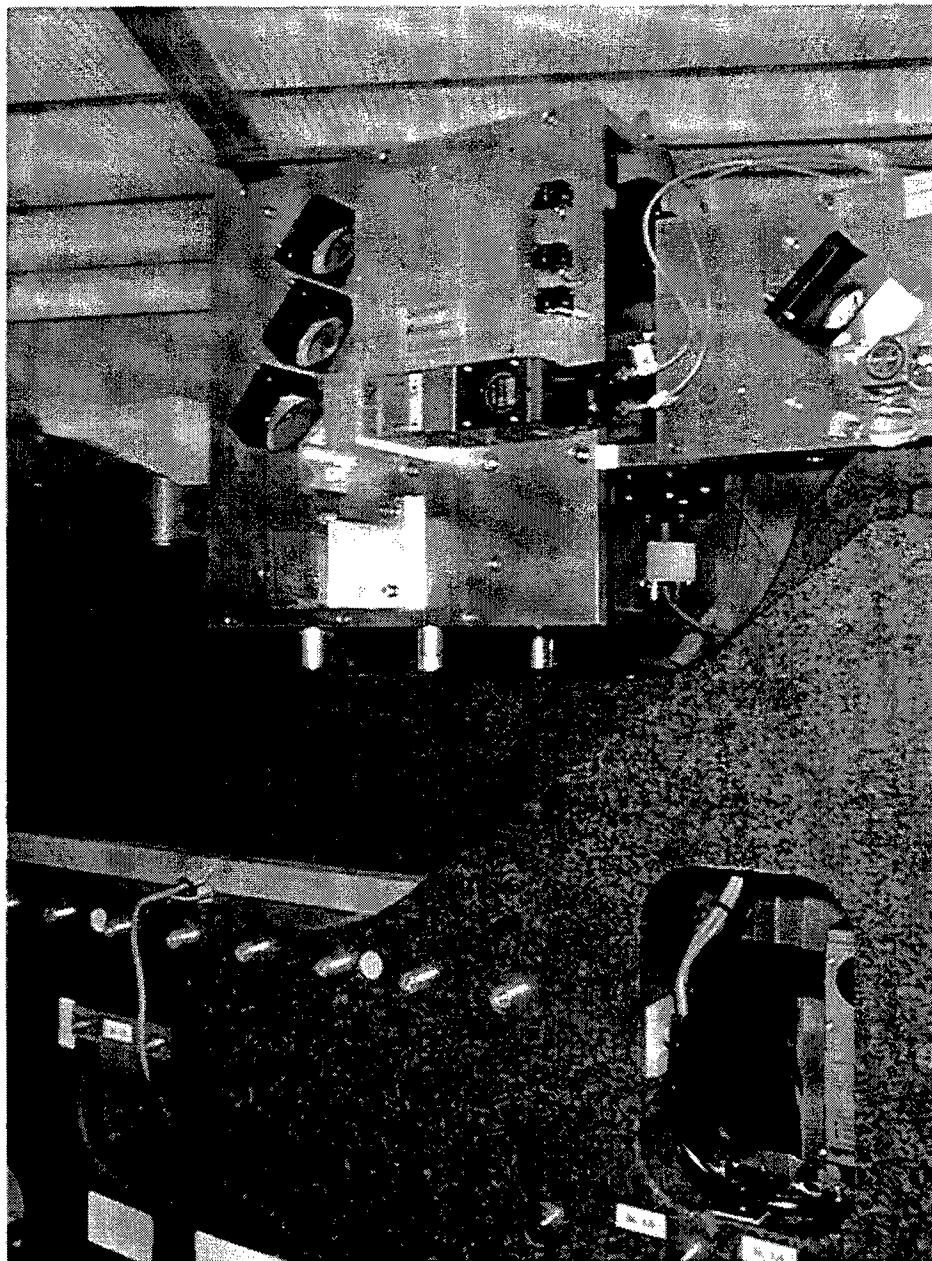
X-Ray Lithography

BCI X-Axis



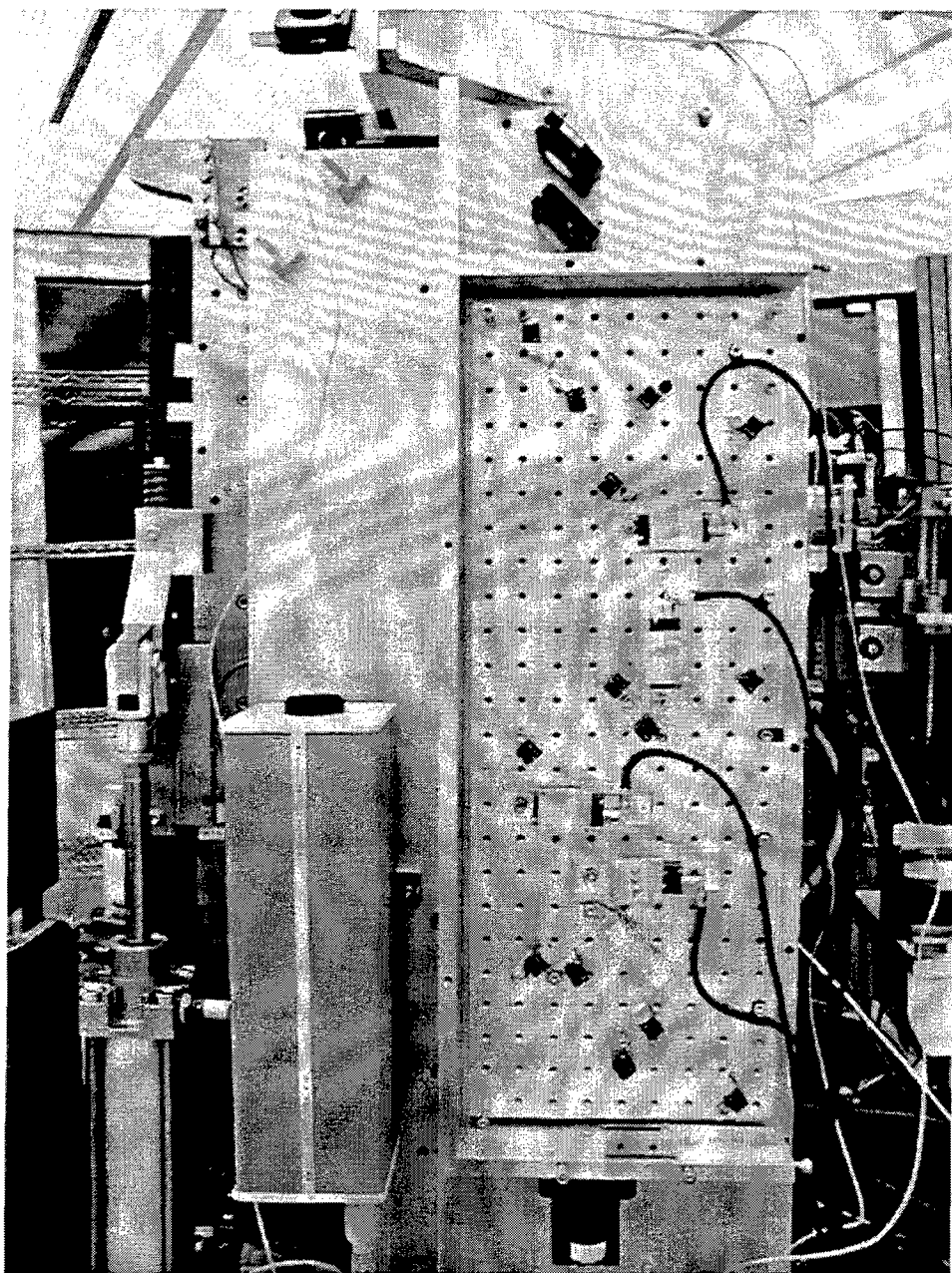
X-Ray Lithography

BCI Y-Axis



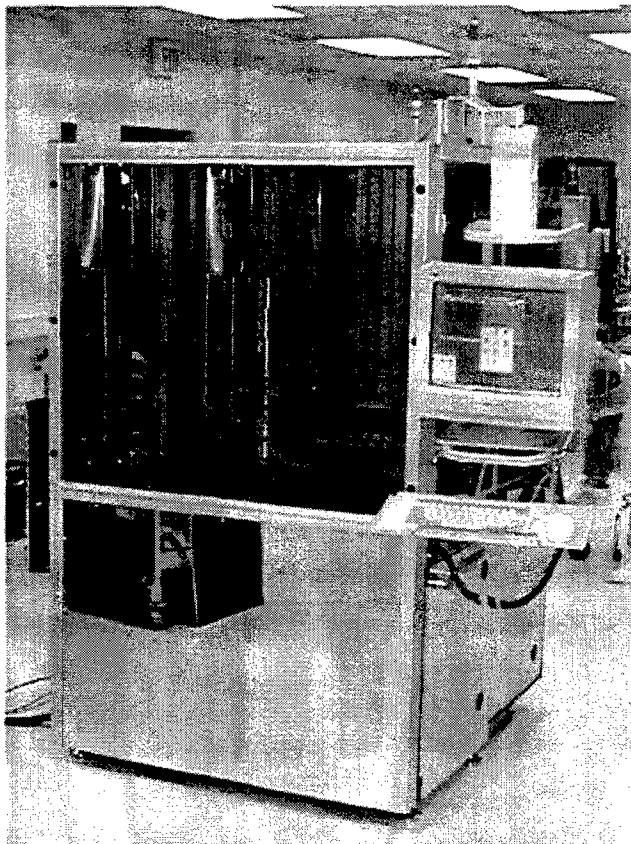
X-Ray Lithography

BCI Electronics



X-Ray Lithography

MHS Bake Station



Exterior View



**Interior View
Transfer Port
at Rear**



X-Ray Lithography

Microwave, Space & Mission Electronics
65 Spit Brook Road, P.O. Box 868, Nashua, NH 03061-0868
Telephone (603) 885-4321



29 June 1998
MED/pjj_a020/98-115

Commander
NAVAIRSYSCOM
ADPO-48, (301)342-2638
Bldg 2185, Suite 1140, Unit 6
27347 Cedar Point Road
Patuxent River, MD 20670-1161

Attention: Mr. Charles D. Caposell, ADPO-48

Subject: Point Source X-Ray Lithography Systems for Sub-0.15 Micron Design
Rules, Interim Report 22 January 1997 through 22 April 1998,
CDRL A020

Reference: Contract No. N00019-97-C-2001

Dear Mr. Caposell:

Enclosed please find a of the subject report dated 22 May 1998 for your review and approval.

Should you have any questions regarding this subject, please feel free to contact Henry Dunne at (603)885-6803, or FAX at (603)885-6045.

Very truly yours,

Sanders, A Lockheed Martin Company

Christine A. Gillis
Contract Coordinator
Microwave, Space & Mission Electronics

cc: DARPA/ETO	USAF
AIR-2.5.3.3.5	DTIC
NRL-6800	NIST
NRL-6860	ARMY II
D805	ARMY I